Electron Transport in GaAs Heterostructures at Various Magnetic Field Strengths

a dissertation presented by

Jeffrey Burnham Miller

to the Division of Engineering and Applied Science
in partial fulfillment of the requirements for the degree of

Doctor of Philosophy
in the subject of
Applied Physics

Harvard University
Cambridge, Massachusetts
January, 2007

©2007 Jeffrey Burnham Miller
All rights reserved.

Dissertation Advisor: Professor Charles M. Marcus Author: Jeffrey B. Miller

Electron Transport in GaAs Heterostructures at Various Magnetic Field Strengths

Abstract

This thesis describes two sets of experiments which explore transport in a two-dimensional electron gas in the presence of a magnetic field. We used nanofabrication techniques to make samples on GaAs/AlGaAs heterostructures, and measured the samples at cryogenic temperatures using ac-lock-in techniques.

In the first set of experiments—the low-field experiments—we studied the effect of spin-orbit coupling. We tuned the strength of spin-orbit coupling from the weak localization regime to the antilocalization regime using *in situ* gate control. Using a new theory, we separately extracted the values for the three material-dependent spin-orbit constants. We also measured the average and variance of conductance in assorted quantum dots, with and without strong spin-orbit coupling, and found quantitative agreement with recent random matrix theory predictions, as long as we also properly included the effects of parallel magnetic field.

In the second set of experiments—the high-field experiments—we studied the transport properties of quantum point contacts (QPC) fabricated on a GaAs/AlGaAs two dimensional electron gas that exhibits excellent bulk fractional quantum Hall effect, including a strong plateau in the Hall resistance at Landau level filling fraction $\nu = 5/2$. We demonstrate that the $\nu = 5/2$ state can survive in QPCs with 1.2 µm and 0.8 µm spacings between the gates. However, in our sample, all signatures of the $5/2$ state are completely gone in a 0.5 µm QPC. We study the temperature dependence at $\nu = 5/2$ in the QPC and find two distinct regimes: at temperatures below 19 mK a we find a plateau-like feature with resistance near (but above) the bulk quantized value of $0.4\,h/e^2$, while at higher temperatures this plateau does not form. We study the dc-current-bias (I_{dc}) dependence of the plateau-like feature, and find a peak in the differential resistance at $I_{dc} = 0$ and a dip around $I_{dc} \sim 1.2$ nA, consistent with quasiparticle tunneling between fractional edge states. In a QPC with 0.5 µm spacing between the gates, we do not observe a plateau-like feature at any temperature, and the I_{dc} characteristic is flat for the entire range between $\nu = 3$ and $\nu = 2$.

Contents

Abstract iii

Acknowledgements ix

1 Introduction 1

2 Introduction to the $^5/_2$ experiment 3
- 2.1 Overview . . . 3
- 2.2 Theoretical Background . . . 4
  - 2.2.1 General introduction to quantum computers . . . 4
  - 2.2.2 Introduction to anyons . . . 5
  - 2.2.3 Integer and fractional quantum Hall effects . . . 7
  - 2.2.4 Topological Quantum Computation . . . 11
- 2.3 Prior experimental work . . . 13
- 2.4 Impact of this work and future directions . . . 15
- 2.5 Techniques . . . 17
  - 2.5.1 Refrigerator and wiring . . . 17
  - 2.5.2 LED . . . 17
  - 2.5.3 Electron Temperature . . . 18

3 Introduction to the spin-orbit coupling experiments 21
- 3.1 Theoretical background . . . 21
  - 3.1.1 Spin-orbit coupling . . . 21
  - 3.1.2 Weak localization and antilocalization . . . 22
  - 3.1.3 Conductance fluctuations . . . 23
  - 3.1.4 Physics in the dot and random matrix theory . . . 23
- 3.2 Perspectives on the 2D spin-orbit experiment . . . 24
- 3.3 Perspectives on the quantum-dot experiments . . . 25
- 3.4 Techniques . . . 27
  - 3.4.1 Data Acquisition . . . 27
  - 3.4.2 Data Analysis . . . 27

4 Spin-Orbit in Two Dimensions 29
- 4.1 Introduction . . . 30
- 4.2 Previous Theory and Experiments . . . 30
- 4.3 Theory of Two-Dimensional Magnetotransport with Spin-Orbit Coupling beyond the Diffusive Approximation . . . 31
- 4.4 Experimental Details . . . 32
- 4.5 Crossover from WL to AL and Separation of Spin-Orbit Parameters . . . 33
- 4.6 Angular Dependence of Spin Precession Rates . . . 34
- 4.7 Comparison with previous Theory . . . 34
- 4.8 Conclusion . . . 35
- 4.9 Acknowledgements . . . 36

5 Antilocalization in Quantum Dots **37**
5.1 Introduction . . . 38
5.2 Previous Experiments . . . 38
5.3 Random Matrix Theory . . . 38
5.4 Antilocalization and Confinement Suppression of Spin-Orbit Effects . . . 39
5.5 Suppression of Antilocalization by an In-Plane Magnetic Field . . . 40
5.6 Breaking of Time-Reversal Symmetry due to an In-Plane Magnetic Field . . . 42
5.7 Effects of Temperature on Antilocalization . . . 42
5.8 *In Situ* Control of Spin-Orbit Coupling with a Center Gate . . . 42
5.9 Acknowledgements . . . 44

6 Conductance Fluctuations in Quantum Dots **45**
6.1 Introduction . . . 46
6.2 Previous Work . . . 46
6.3 Spin-Rotation Symmetry Classes . . . 46
6.4 Experimental Techniques . . . 47
6.5 Characterization of Spin-Orbit Strength at Zero In-Plane Field . . . 47
6.6 Variance at Zero In-Plane Field . . . 48
6.7 Effects of Spin-Rotation Symmetry on the Variance . . . 49
6.8 Orbital effects of $B_{\|}$ on the Variance . . . 50
6.9 Conclusion . . . 51
6.10 Acknowledgements . . . 52

7 Experimental observation of the $\nu = 5/2$ state in a quantum point contact **53**
7.1 Introduction . . . 54
7.2 Measurement Techniques . . . 55
7.3 Previous Experiments . . . 55
7.4 Experimental Details . . . 55
7.5 Bulk Measurements . . . 56
7.6 Demonstration of the QPC in IQHE and FQHE regimes . . . 57
7.7 Observation of plateaus at $\nu = 5/2$ . . . 58
7.8 Temperature data in the QPC . . . 58
7.9 I_{dc} data . . . 59
7.10 Conclusion . . . 61
7.11 Acknowledgements . . . 61

A Raith Users Guide **63**

B Detailed Fabrication Procedures **77**
B.1 Getting Started . . . 77
B.2 Cleave . . . 77
B.3 Mesa Photo . . . 78
B.4 Etch Procedure . . . 81
B.4.1 Summary . . . 81
B.4.2 Details . . . 81
B.4.3 Profilometer Operation . . . 82
B.5 The rest . . . 83

C Complete Nanofabrication Recipe for 5/2 Devices **85**
C.1 5/2-ready fab recipe . . . 86
C.1.1 Mesas . . . 86
C.1.2 Ohmics . . . 86
C.1.3 Small gates . . . 87
C.1.4 Connector gates . . . 88

D Wafer Data Sheet **89**

E Antilocalization Fitting Routines **91**

Acknowledgements

The Marcus lab is an amazing place to do physics. Unlimited helium, unlimited lock-in amplifiers, unlimited $50k gigahertz pulse generators, no broken equipment to be found, and, yes, tools generally kept where they belong. Thanks go to Charlie for invisibly doing the dreary, never-ending, grant writing (and note writing) that made it possible to do exciting world-class research without ever having to worry about a dollar (or a missing tool). But grants alone do not teach students how to become scientists; that requires a role model and a mentor. With preternatural creativity, irrepressible optimism, a keen eye for interesting problems and for craftsmanship and elegance in their solution, nor'easterly energy levels, a willingness to do anything—from the menial to the impossible—to get the research done, and always knowing what to do next, one step at a time, Charlie *is* the consummate experimentalist. Besides that he is a pleasure to work with, quick to make or get the obscure joke, and always ready with the unexpected allusion or anecdote. Charlie's ability to pair students with the right theorist at the most mutually beneficial time is legendary; his willingness—in the interest of promoting the kind of discussions that lead to advancements in science—to suffer gladly (even enjoy) the occasional eccentricity in both is commendable. Thank you.

It was a tremendous privilege for me to spend most of my graduate career working with another great experimentalist. Dominik has experimenter's hands; he somehow just gets stuff to work. The secret behind those hands is that he never turns any knob or solders any resistor randomly: every move he makes in the lab is based on his deep understanding of the physics. The same secret is behind his eye, which never misses a single wiggle or bump in the data and finds the explanation for each one. He is a good friend and significant part of the reason I *enjoyed* my PhD. Thank you.

Amir's grasp of the *fundamentals* of physics, and how the core concepts show up in the most advanced experiments, is an example of how a clear, seemingly simple thought process can lead to the most elegant, important experiments. To work with Amir is to remember that *simplex sigillum veri*, but that only the most accomplished intellect can reduce complicated problems to their fundamental simplicity. I am very lucky I was able to work with Amir at Harvard, then at the Weizmann Institute, and then again at Harvard. Thank you.

The research we do simply cannot be done alone, especially a problem as interesting and difficult at the $5/2$ experiment. As luck would have it, the team expanded to meet the problem. Iuliana has a sharp eye and a physical way of thinking about things that helped us keep making progress even when nothing seemed to be working. She is also dependable with a capital "D." She stuck with the project through almost intolerable difficulties, and kept things running without a minute's interruption even when it was time for me to go have a baby. Marc welcomed me into his lab and became a soothing source of valuable advice and encouragement. I always looked forward to spending a few minutes or a few hours looking at data in Marc's office; he knows that every little piece of data is telling part of a story, and he knows how to go from noisy, messy, working data to a neat, tidy story by reading with a careful eye and asking a few perceptive questions. Eli learned a lot of details amazingly fast and helped keep a seemingly endless experiment running

when everyone else was just too exhausted. Thank you.

For all practical purposes, I learned quantum mechanics, statistical mechanics and condensed matter physics from Heather. Thank you for your patience and help with all those problem sets, and for helping to make work fun back in the good-old days. Alex was always interested and able to help with *any* problem, from the most obscure detail of mathematical physics to Raith alignment difficulties to helping move a sofa up the stairs. He also, in a lab full of creative folks, wins the prize for the most memorable lab art project: thank you for everything, especially the "soda-sculpture." Reilly brought with him tremendous knowledge about all aspects of low-temperature experiments, along with a selfless willingness to help others (including me) apply them. He also brought his Australian friendliness and good humor, and helped make work fun back in the good-new days. Jimmy, tea connoisseur, a cleanroom craftsman and vegetarian, thanks for showing us how to put on boxing gloves and smash the bag. I learn something every time I talk to any member of the lab: Andrew, Christian, Doug, Edward, Hugh, Jason, Jennifer, Josh, Kate, Leo, Lily, Mike, Nadya, Nathaniel, Reinier, Ron, Sarah, Slaven, Susan and Yiming. Thank you.

Yuli, who seems never to have forgotten any number, was kind enough to dial our number in lab over and over again until we all understood spin-orbit coupling. Bert, Bernd and Xiao-Gang were always happy to help us think about the $5/2$ data, while Loren, was always glad to discuss tea or wafers. All the members of Microsoft's *Project Q* team have been a tremendous help, especially Ady and Steve. David G-G has been a source of advice, experience, knowledge, and kindness. Thank you.

So many people work out of everyday sight to keep a research group productive, James, Jim, James, Ralph, Joan, Susan, thanks for keeping everything running smoothly. One of my first projects was to help (watch) while Jim designed the BiasDAC, a tool that has been invaluable for all of our research. Thank you.

To my parents for teaching by example, for having exuberant confidence in me, and for all your love, thank you. To Neer who has only just started helping, you have been a constant delight while I've been doing a lot of typing (you even helped a little at the keyboard, and you would have liked to do more), thank you.

Experiments take a long time; sometimes it seems like I never came home. But when I did come home, without fail it was to a loving reception. Following Manjari to Harvard turns out to have been a fabulous decision: here I've had a chance to work with all the wonderful people I mentioned, learn from them how to be a scientist, push my perfectionism-problem to almost absurd levels (also following some world-class examples), help out with really interesting research, but most rewardingly to love Manjari. *Thank you!*

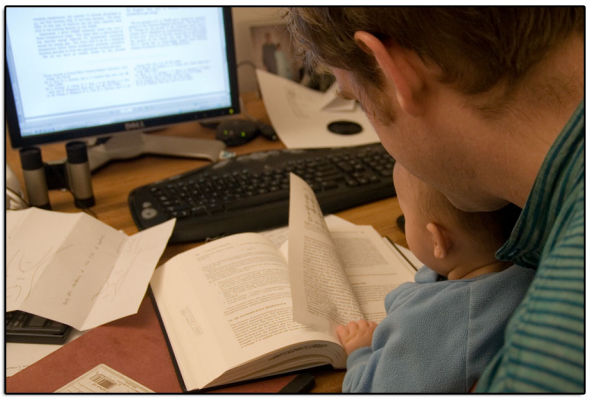

Chapter 1
Introduction

It seems inevitable that arsenic—the garlicky king of poisons and poison of kings—and gallium, an element named after France[1], would combine to form a compound of some intrigue. Indeed, the compound *gallium arsenide* (GaAs) has played host to some very intriguing physics over the years. One feature that makes GaAs so scientifically useful[2] is that we[3] can grow a nearly perfect interface between GaAs and AlGaAs where electrons become trapped in a two-dimensional (2D) universe. When these electrons are under the influence of a strong magnetic field, there is almost no telling what wild physics can happen: nobody predicted that 2D electrons and some magnetic flux would condense into an entirely new state of matter [1], the anyonic fractional quantum Hall fluid, right at the GaAs/AlGaAs boundary.

During my PhD, I have studied how electrons confined to 2D behave when I apply a magnetic field. The laboratory for these studies has been the GaAs/AlGaAs heterostructure[4]. The results of my research are contained in this thesis.

Organization of the thesis

This thesis is organized into three general parts: the introduction, the papers, and the appendices.

The introductions

My PhD work can be divided into two different magnetic field ranges, which I introduce separately in two different chapters. Chronologically[5], I first studied the *low-field* transport properties of electrons in a two-dimensional electron gas (2DEG), in particular, the effects of spin-orbit coupling and magnetic field applied both parallel and perpendicular to the 2DEG. The last two years of my PhD I studied the *high-field* properties of the same system[6], in particular the fractional quantum Hall effect state at filling fraction $\nu = 5/2$. In both introduction chapters, the primary goal is to lay out the problems I have studied during my PhD: why the problem is interesting, the status of the problem before my work, the specific contributions my work has made to understanding

[1] France≡Gallia

[2] Other features of GaAs also make it practically useful. In fact, you are probably carrying some GaAs right now: its in your cell phone.

[3] "We" means humanity in general, but Loren Pfeiffer and Art Gossard—the creators of the GaAs heterostructures I measured for this thesis—in particular.

[4] This small laboratory has been housed within a bigger laboratory provided by Prof. Charlie Marcus, see Acknowledgements.

[5] The chapters in my thesis are not arranged in the same order that we actually conducted the experiments.

[6] The materials were the same (GaAs/AlGaAs heterostructures), but the details were a bit different. The wafers we used for the $5/2$ experiments had electron mobility up to $2000\,\mathrm{m^2/Vs}$, whereas the best mobility in the spin-orbit samples was only $30\,\mathrm{m^2/Vs}$.

the problem, and the current status of the problem. The introductions also discuss some of the non-obvious experimental techniques we used for each set of experiments.

In the case of the 5/2 experiment, the introduction also is intended to provide a fairly complete, physically-oriented theoretical background at a level that is comfortably accessible to the interested experimentalist. As far as I know, there is no such review in the literature, which has not made my life easy over the past several years. Hopefully, the 5/2 introduction can serve as a starting point for other experimentalists who are new to topological quantum computation, new to non-Abelian anyons, or new to incompressible, weakly coupled Cooper pairs of composite fermions.

The papers and appendices

After the introductions, the second part of the thesis consists of our detailed results, in the form of papers that have either been published or submitted for publication. The third part consists of appendices which give very technical details of our procedures and techniques that may be of interest to future experimentalists.

Chapter 2

Introduction to the $5/2$ experiment

2.1 Overview

The work that has occupied the final two years of my PhD—the effort to study (and eventually manipulate) the fractional quantum Hall effect (FQHE) state at filling fraction $\nu = 5/2$ in mesoscopic devices—has been especially challenging but especially rewarding. In Chapter 7, I will describe the outcomes of this work in detail. Briefly, we experimentally observed a plateau near $\nu = 5/2$ in quantum point contacts (QPC), and also found evidence that we can use QPCs to induce quasiparticle tunneling between fractional edge states. This is exciting because tunneling of the quasiparticles at $\nu = 5/2$ is one of the technological capabilities required to test whether these quasiparticles obey non-Abelian statistics [2–6]. If the $\nu = 5/2$ state turns out to be non-Abelian, then needless to say this would be a tremendously exciting discovery: aside from being a new, unique state of matter, a non-Abelian state could in principle be used to implement a topological quantum computer (TQC).

In this chapter I first provide a theoretical introduction. I hope to provide just enough background to allow me to paint an accurate and intuitive picture of the physics of the $\nu = 5/2$ state—at least as it is understood at this time—including the proposed use of $5/2$ for quantum computation. I then review previous experimental work. Finally, I discuss in detail the contributions my PhD work has made to this field, and I discuss possible future directions. (Those wishing to come back to the theoretical review later may skip directly to the experimental contributions of my PhD work in Section 2.4.) In the last section of the introduction, I discuss experimental techniques.

Prologue

Kitaev invented the TQC in 1997 [7]. The only catch is, nobody really knows *exactly* how to build one. One possibility is the method published in 2003 by Duan, Demler and Lukin [8], which is a "general technique that allows one to induce and control strong interaction between spin states of neighboring atoms in an optical lattice," including a way "to realize experimentally the exotic Abelian and non-Abelian anyons" that are required for quantum computation. Another possible way to realize a TQC was introduced in early 2005, just as I was thinking about what I wanted to work on as one last-great-project for my PhD. Das Sarma, Freeman and Nayak proposed using the $\nu = 5/2$ FQHE state to implement (at least elements of) a topological quantum computer [2, 9]. At that time, I decided to spend the last four-to-six months of my PhD working on this interesting problem. Two years later, having answered some significant scientific and technological questions, the problem looks even more interesting, if more challenging, than we had initially realized.

2.2 An experimentalist's theoretical introduction to the fractional quantum Hall effect, the state at $\nu = 5/2$ and topological quantum computation

To motivate our experimental interest in the FQHE state at $\nu = 5/2$, provide the prevailing theoretical picture of how this unusual state of matter forms, and describe how to use this matter to build a computer, requires a fairly intricate arc of reasoning. In this section, I will start this arc with a very brief introduction to the general principles of quantum computation—admittedly a long way from the experiments that comprise my PhD research. However, this starting point allows the intellectual arc to curve gently, and hopefully illuminatingly, through a list of tricky topics on the way to our goal. So here we go.

2.2.1 General introduction to quantum computers

In this section I introduce the idea of quantum computation. For a more detailed treatment, I recommend John Preskill's Cal-tech lecture notes on the topic [10], which are available on the internet. (He calls them lecture notes, but they run to hundreds of pages, and I think he is getting ready to turn them into a book.) My treatment borrows heavily from his, but is of course much shorter and is tuned towards topological quantum computation and the $\nu = 5/2$ FQHE state.

Why go quantum?

All personal computers[1] are *universal* [10], which means any computation that could be done using a quantum computer (QC) could also be done on a home PC. The advantage of the QC is that certain types of computation could be done *much* faster. We will now see how this works.

The unit of quantum information is the qubit. We can model the qubit as a vector in a two dimensional complex vector space with inner product. We can call the qubit basis vectors $|0\rangle$ and $|1\rangle$ (reminiscent of a classical bit), and then we can write down

$$|\psi\rangle = a|0\rangle + b|1\rangle \tag{2.1}$$

where a and b are complex numbers, normalized $|a|^2 + |b|^2 = 1$. When we measure the qubit, the state $|\psi\rangle$ is projected onto the basis. The probability of measuring $|0\rangle$ is $|a|^2$ and of course the probability of measuring $|1\rangle$ is $|b|^2$. This brings up the interesting fact that the output of a quantum computer is not deterministic: repeated measurements with exactly the same inputs will yield a probability distribution, not an "answer" in the sense of a classical computer. This probabilistic behavior is inherent to QCs. Part of the art in developing a good quantum algorithm is to find a way to get the desired output with very high *probability*. This also helps explain why the types of algorithms that have already been developed for QCs involve problems that are hard to solve but easy to check: to factor a large number is hard, but a QC can find an answer fast, which the user can then easily check. If the answer is wrong, the algorithm can be re-run.

This probabilistic behavior makes QCs seem worse than classical computers: even when everything is working perfectly, QCs don't always get the answer right. To see the advantage of a QC, consider 50 qubits instead of just one. A 50 qubit QC can be represented as

[1] Even macs.

$$|\psi\rangle = \sum_{x=0}^{49} a_x |x\rangle \tag{2.2}$$

where $\sum_x |a_x|^2 = 1$, and the basis vectors $|x\rangle$ are either $|0\rangle$ or $|1\rangle$. To perform a computation, we prepare $|\psi\rangle$ in some input state, perform unitary operations on selected qubits (these operations are known as *quantum gates*), and project the result onto the $|0\rangle$, $|1\rangle$ basis. For each $|x\rangle$, the probability of measuring $|0\rangle$ is $|a_x|^2$. And that's it. As promised, this procedure can be done either with a QC or a classical computer. The trick is how long it would take to run the computation on a classical computer. We only have 50 qubits, but to model $|\psi\rangle$ with a classical computer we would need to keep track of 2^{50} complex numbers; that is more than 2000 terabytes (single precision). Now imagine trying to compute rotations of 2000 terabyte matrices: it cannot be done.

Bell's theorem [11] prevents the use of the following shortcut to classically simulate a QC [10]. It might have been possible, since the output of the QC is probabilistic, to use probability distributions and a random number generator along each step of the computation instead of performing exact vector math on terabytes (or more) of data, only to finish the calculation with a probabilistic projection. However, Bell's theorem *specifically* prevents local probabilistic algorithms from reproducing the quantum mechanical result.

In summary, it is the exceedingly complex non-local correlations of the quantum state, along with the enormous size of the vector space ("Hilbert" space) of a quantum system that make it useful for efficient computation of certain types of problems. At the end of this introduction, we will see how the physics of the 5/2 state could meet these criteria.

Lots of schemes, little coherence

There are quite a few ideas for how to actually implement qubits, including optically trapped atoms [8] or ions [12], quantum optics [13], cavity QED [14], NMR [15] and solid state implementations [16, 17]. In fact, few-qubit QCs have already been demonstrated in some of these systems [18–20] but nobody has been able to build a QC with anywhere near enough qubits to be useful. The difficulties, including gate accuracy and noise reduction, can largely be traced back to the fact that qubits are so good at forming non-local correlations that they do not really know when to stop; the qubits become correlated (the more graphic word is entangled) with the environment. This entanglement effectively measures the system, and that measurement *collapses* the qubits onto a set of basis states, thereby destroying *coherence*. This decoherence problem is extremely hard to overcome, since it is very hard to isolate the physical qubits (ie, little atoms or electrons) from the entire rest of the universe. Each proposed QC implementation has schemes to reduce the decoherence. But the implementation I am gearing up to describe—the topological QC—has, uniquely among known implementations, a *built-in* resistance to decoherence. However, before I can describe a topological QC, I need to introduce *anyons*.

2.2.2 Introduction to anyons

Topological quantum computers (TQC) depend on a mathematical construction called the *anyon*. Amazingly, it turns out that this mathematical construction is also a physical reality: the quasiparticles that form in the regime of FQHE plateaus are anyons. In this section, I introduce these amazing little particles. I begin by discussing the quantum mechanical concept of identical particles.

Systems of identical particles are a fundamental topic in quantum mechanics [21]. *Identical* is a technical term: the theory of quantum mechanics states that it is not possible *even in principle*

to distinguish two electrons, two protons, two neutrons, etc. As a result, if we swap two electrons there may not be any observable differences between the two states. More mathematically, we can define a permutation operator P (in 3D) according to

$$P|x_1\rangle|x_2\rangle = |x_2\rangle|x_1\rangle. \tag{2.3}$$

It is easy to confirm that $PP = I$, the identity matrix, and so the only eigenvalues of P are ± 1. This result is a mathematical deduction from the principles of quantum mechanics [21]. The postulates of quantum mechanics go on to identify particles with the eigenvalue $+1$ as bosons and -1 as fermions. All of this is a standard and fundamental topic of quantum mechanics known as "quantum statistics," but is only strictly true for three or more dimensions.

In two dimensions, the situation becomes even more interesting. Kitaev elegantly introduces anyons [7]:

> Anyons are particles with unusual statistics (neither Bose nor Fermi), which can only occur in two dimensions. Quantum statistics may be understood as a special kind of interaction: when two particles interchange along some specified trajectories, the overall quantum state is multiplied by $e^{i\varphi}$. In three dimensions, there is only one topologically distinct way to swap two particles. Two swaps are equivalent to the identity transformation, hence $e^{i\varphi} = \pm 1$. On the contrary, in two dimensions the double swap corresponds to one particle making a full turn around the other; this process is topologically nontrivial. Therefore the exchange phase φ can, in principle, have any value—hence the name *anyon*.

Here is a concrete example of an anyon, which I have adapted from the *Physical Review Letter* where Wilczek first introduced (and named) anyons [22]. Suppose we have some 2D fluid comprised of particles with charge q. Suppose we apply a magnetic field perpendicular to the 2D plane, and for some reason the field forms point-like tubes carrying flux Φ. Finally, suppose the charge q merges onto the edge of the flux tube Φ to form a new type of particle[2]. Now lets rotate this composite particle counterclockwise by exactly 2π. During this rotation, the charge makes a complete loop around the flux, which results in an Aharonov-Bohm phase of $e^{iq\Phi/\hbar}$. But this (unitary) rotation can also be represented via the angular momentum:

$$e^{-i2\pi \mathbf{J}/\hbar} = e^{iq\Phi/\hbar} \tag{2.4}$$

and so the angular momentum can take eigenvalues

$$J = m - {}^{q\Phi}/_{2\pi} = m - {}^{\theta}/_{2\pi} \tag{2.5}$$

where m is an integer and we have defined the angle θ. We will call $e^{i\theta}$ the *topological spin* of the anyon [23]. As we already mentioned, in 3D the only allowed values of θ are 0 and π, because (in the language of groups) a 4π rotation in the the 3D rotation group SO(3) can be contracted smoothly to a trivial path [23]. However, the 2D group SO(2) allows (in principle) any value of θ. Hence, anyons. By a similar argument, moving one anyon around another results in the same, nontrivial Aharonov-Bohm phase as rotating one anyon. We will see this *braiding* again.

At this point, I pause to make several comments. The first is that the situation in one dimension is less interesting, or at least more ambiguous, because in order to swap two particles, they must pass through one another, so it becomes hard to separate quantum statistics from

[2] At this point were are doing a math problem, not worrying about whether such a particle would ever really form.

interaction effects [10]. We already established that anyons do not exist in 3D and higher. So 2D is truly a special situation for quantum statistics. The second comment is that, even in this 3D universe, 2D is not just a mathematical figment, but a physical reality, thanks to the GaAs/AlGaAs heterointerface. Finally, the inherently topological origin (all that matters is the Aharonov-Bohm winding number, not the precise path) of anyons is interesting in the context of QC. If a qubit could be encoded topologically—that is, by using the winding number—then the information would be intrinsically robust against decoherence: small local interactions with the environment would not change the number of times particles have been moved in complete loops around each other.

2.2.3 Integer and fractional quantum Hall effects

Having met anyons, we now turn to a less abstract concept: the Hall effect. The treatment of the integer and fractional Hall effects I present here is designed to lead straight to the 5/2 state. Störmer's Nobel lecture [24] is a masterpiece, and I recommend it as a more general introduction to both the IQHE and the FQHE.

Classically, the Hall effect predicts a simple linear relationship between the Hall resistance, R_{xy} and the magnetic field: $R_{xy} = B/ne$, where n is the electron density and e is the charge of an electron. The basic observation of the quantum Hall effects (both integer and fractional) is that at certain rational values of $\nu = \frac{n}{B}\frac{h}{e}$, R_{xy} gets "stuck" at ν over finite regions in B (as the density n is held constant); that is, plateaus develop in the Hall resistance.

Integer Quantum Hall Effect

To explain the IQHE we need to remember that in a magnetic field the continuous energy spectrum of the 2DEG breaks up into discretely spaced, highly degenerate allowed energy levels $E_n = (n + 1/2)\hbar\omega_c$ called Landau levels. At finite temperature, the Landau levels broaden slightly into a very narrow energy band [25]. When the chemical potential lies within one of these bands, the material is metallic; that is, the electron wave functions are not localized and transport can occur throughout the sample with some finite conductivity[3]. Away from these extended Landau level states, any real material will have localized states (due to slight local variations in electron density caused by tiny local variations in the 2D potential landscape). When the chemical potential is in the region of the localized states, varying the number of electrons only adds or subtracts localized states which carry no current, so the current remains fixed at the full Landau level value. Therefore, when the chemical potential is between Landau levels, the system is *incompressible*.

In a semiclassical picture, the Landau levels correspond to electrons moving in circular orbits of quantized size, due to the Lorentz force. In a bulk region of the 2DEG, the circular orbits cause the electrons to be localized. But within a magnetic length $\ell_B = (\hbar/eB)^{1/2}$ of the edge, the orbits will skip off the edge potential and form quasi-1D channels. One channel forms for each occupied Landau level. A fully quantum mechanical treatment yields the same result [27, 28]. Either way, when the quantum Hall fluid is incompressible, all the current will flow around the edges of the sample in 1D edge channels in a direction (clockwise or counterclockwise) set by the magnetic field. Since each edge can only support current flowing in one direction[4], and since the edges are spatially well separated, backscattering is not possible and the longitudinal

[3]The existence of extended states in 2D is not allowed by scaling localization *at zero magnetic field*, but is now the generally accepted picture for the quantum Hall effects [25–27], which occur at substantial fields. The exact fate of the extended states as the field decreases towards zero does not seem to be completely settled in the literature.

[4]In the hierarchical picture of fractional edge channels [29] the picture is more complicated but the result is the same.

resistance along an edge channel is vanishing. The resistance of each edge state is just the 1D contact resistance, h/e^2[30]. The Hall resistance is quantized because only the edge states carry current, and *their* resistance is quantized.

FQHE and quasiparticles

The FQHE, unlike the IQHE [28], arises due to interactions between electrons. Because of the complete degeneracy of states, there is effectively no kinetic energy associated with the electrons in the Landau level, yet the Coulomb repulsion is still effective. One configuration that may have minimized the energy in this picture would be if the electrons were equally spaced as far apart from each other as possible, forming a *Wigner crystal* [31]. However, the position of the electrons is uncertain to within a magnetic length ℓ. In the range of density and magnetic field where the uncertainty broadened electron wave functions overlap, any Wigner crystal that may have formed could melt and the lowest energy wave function is not necessarily a crystal. In fact, the ground state is described by Laughlin's [32] wave function:

$$\Phi^m(z_1, \ldots, z_N) = \prod_{i<j}(z_i - z_j)^m \mathrm{e}^{-\frac{1}{4\ell^2}\sum |z_i|^2} \tag{2.6}$$

where $z = x + iy$ is the position of a particle and m, which corresponds to filling fraction $\nu = 1/m$, is an *odd* number to preserve Fermi statistics. The exponential term comes from the Landau level wave function [33] and the $(z_i - z_j)$ keeps the particles far apart to reduce Coulomb energy [31]. Importantly, this wave function leads to an incompressible quantum liquid.

Incompressibility, just as in the IQHE case, implies plateaus in R_{xy}. It also implies that, to keep the macroscopic filling fraction pegged at the favorable value, small changes in B or n must cause only well-localized deviations from ν. What this means is that when the magnetic field is tuned to *exactly* the right value for filling fraction $1/m$, the wave function of the system is exactly Eq. 2.6. But when the field is detuned, a *localized quasihole*[5] is created. The wave function of the ground state plus a quasihole localized at position z_0 is obtained by acting on the ground state:

$$\Phi^m_{z_0} \equiv \prod_i (z_i - z_0)\Phi^m. \tag{2.7}$$

It is clear from the $(z_i - z_0)$ term that all the electrons in the ground state feel a barrier at z_0 and are pushed away. The range of the repulsion is short: far away from z_0 the wave function is essentially unaffected. Less immediately obvious is the fact that the quasihole has fractional charge e/m. However, it can be shown [32] that the spatial extent of the "bubble" in the electron fluid excludes exactly $1/m$ of an electron, so the quasihole carries the fractional charge e/m. It can also be shown using topological Berry phase arguments (similar in spirit to our introduction to anyons in Section 2.2.2) that the quantum statistics of the quasiholes are *fractional*, although to do so correctly is extremely non-trivial[6]. Quasiparticles are described by a slightly more complicated wave function, but they also have fractional charge and fractional statistics. The upshot is that these FQHE quasiholes and quasiparticles are *anyons* [27, 34]. Fractional charge has been observed experimentally [35], but to observe the anyonic statistics remains an experimental challenge [2, 36].

[5] Depending on the sign of the detuning, either a quasiparticle or a quasihole can be created. Quasiholes are technically simpler, quasiparticles are treated in the literature [34]

[6] An interesting historical note: papers were published showing the statistics of the quasiholes are Fermi, Bose, and Other. The correct answer, published by Halperin [27] and later expanded and confirmed by Arovas, Schrieffer and Wilczek [34], is "Other"; the quasiholes are anyons with fractional statistics.

Before moving on, it is important to be clear about "flux tubes." Following Wilczek [37], I introduced anyons as a charge/magnetic-flux composite (Section 2.2.2). However, real FQHE quasiparticles *do not* actually carry magnetic flux [38]; the true origin of the fractional statistics is a complicated many-body effect. Having emphasized this detail, I will now move on to the composite fermion picture of the quasiparticles.

Composite fermions

Jain [39] realized that the essential features of the FQHE can be understood intuitively in terms of a new kind of particle—the *composite fermion* (CF). The composite fermion theory is based on the single hypothesis [33] that a system of electrons can reduce its energy if each electron captures an even number $2n$ of *vortices*. Conceptually, a vortex forms when one magnetic flux quantum pierces the 2DEG. Mathematically, the vortices are singular points in a Chern-Simons gauge representation [40]. The electron density at the center of a vortex is zero, increasing to the bulk value at the perimeter. Electrons can reduce their Coulomb interaction by sitting in a vortex; hence, at rational values of $\nu = 1/2n$ the energy of the system is minimized by forming *composite fermions*, which are new particles comprised of an electron that has "captured" $2n$ vortices. (The vortex number has to be even to preserve the Fermi statistics of the CFs). At $\nu = 1/2$, the entire external magnetic field is used up making the CFs, and the Coulomb interaction is essentially screened; the system becomes mathematically equivalent to a system of fermions moving in a zero magnetic field [40]. As the magnetic field is varied away from this effective zero-point at $\nu = 1/2$, the CFs experience Shubnikov-de Hass oscillations as effective Landau levels form. As the deviation from zero field increases, the CFs undergo an effective integer quantum Hall effect, with plateaus at $\nu = \frac{p}{2qp+1}$ when p Landau levels are occupied (p is a positive or negative integer, q is an integer). We have just shown that the FQHE can be conceptualized as an IQHE of CFs [33].

Fractionally charged excitations can occur near $\nu = \frac{p}{2qp+1}$ on the FQHE plateaus. For simplicity, take the case of $\nu = 1/3$. If the magnetic field deviates from exactly $\nu = 1/3$ (for fixed density) by one flux quantum, then one vortex will be formed; this vortex is a quasihole. Because each electron normally carries three vortices at $\nu = 1/3$, a single vortex (which causes the local electron density to go to zero) looks like a *deficit* of $1/3$ electron, so the quasihole charge is $+e/3$. This, then, is another way to think about anyons.

Composite bosons

By extension of the composite fermion picture, [41–44], it is possible to describe odd-denominator FQHE states in terms of composite bosons. At odd-denominator filling fractions, it is possible to describe composite particles that are composed of an electron and an odd number of effective flux quanta (instead of the even number in the composite *fermion* picture), and hence the composite particles have bose statistics. These bosons then condense into a superfluid. The superfluid exhibits a Meisner effect, like other superfluids, expelling the Chern-Simons effective flux quanta and forming vortices. As before, these vortices constitute the fractionally-charged anyonic quasiparticles. This minor extension of the composite fermion picture is useful to have in mind as we move to the $\nu = 5/2$ state.

The $\nu = 5/2$ state

So far we have only discussed the origin of the odd-denominator FQHE plateaus. The experimental observation of an even-denominator plateau at $\nu = 5/2$ [45] cannot be explained in any of the

pictures of the FQHE or IQHE we have discussed. In fact, at this time the actual quantum mechanical wave function of $\nu = 5/2$ state is under considerable debate. One proposal by Moore and Read [46] is to multiply the Laughlin FQHE wave fuction by a Pfaffian factor:

$$\Phi^m(z_1, \ldots, z_N) = \prod_{i<j}(z_i - z_j)^m e^{-\frac{1}{4\ell^2}\sum |z_i|^2} \cdot \mathrm{Pf}\left(\frac{1}{z_i - z_j}\right) \tag{2.8}$$

where the Pfaffian[7] is a way of describing a BCS-like *pairing* [47] of composite fermions [46, 48**?** –50]. The Pfaffian picture is supported by numerical studies [51], although experimental confirmation is, so far, lacking (the work in this thesis is a first step towards an experimental verification—or refutation—of the Pfaffian picture). Experimental evidence is of course needed to help determine the nature of the wave function at $\nu = 5/2$, especially since there are other proposals for the wave function [49, 52].

Although the Moore-Read wave function is only one of many proposals for the $\nu = 5/2$ state, we will study it in some detail for two reasons. The first is that the results of numerical studies suggest the Moore-Read state has the lowest energy. The second is that the Moore-Read state leads to non-Abelian quasiparticle excitations.

The Moore-Read picture of the $\nu = 5/2$ state has some similarities to the Chern-Simons composite-boson picture (presented at the end of the previous section): in both cases, the ground state is a superfluid of bosons that supports vortex quasiparticle excitations. However the Moore-Read state is a BCS-like condensate of Cooper-paired composite fermions, whereas the (abelian) odd-denominator FQHE states are condensates of single bose-like quasiparticles.

The Moore-Read state also differs from other common BCS superfluids in the way the fermions are paired. The Moore-Read wave function pairs the composite fermions in an angular momentum $l = -1$ p-wave orbital instead of the more common $l = 0$ s-wave orbital [53, 54]. This non-zero angular momentum results in the breaking of spin-rotation, spatial-rotation, parity and time reversal symmetries [49]. These broken symmetries can lead to textures in the order parameters for the pairing, and quasiparticle excitations of vanishing excitation energy on these textures, called *zero modes* [49], which I describe below.

Another property of the Moore-Read state—a property which is not unlike typical BCS superfluids but which is different from other FQHE states—is that the vortices are actually "half vortices", with a charge of $e/4$ instead of $e/2$. Physically, one can associate this halving with the pairing of CFs into Cooper pairs. Furthermore, each vortex is associated with an intra-vortex zero mode. To gain a physical sense of the zero-mode, we consider that each vortex is a small, circular edge (like the edge of the Hall bar) with vanishing electron density at the center. Thus each vortex has a domain wall to separate the vacuum at the center from the Cooper-paired phase outside [49]. These domain walls must satisfy the same boundary conditions as the edges of the sample. The result[8] is that, due to the p-wave pairing of the CFs, in addition to positive and negative energy chiral modes on opposite edges (the edge states), there is a zero energy mode that is *shared* between the edges. Applied to the vortices, these boundary conditions endow each vortex with one zero energy mode that is entangled with all the other vortex-zero-modes, leading, for $2n$ vortices, to 2^{n-1} *distinct* degenerate states [55, 56]. This large degeneracy of ground states—due to the zero modes, which arise due to the p-wave pairing of CFs—is what allows the Moore-Read state to be non-Abelian [23, 49].

[7] The Pfaffian is the square root of the determinant of an antisymmetric matrix.

[8] Briefly, the Pfaffian is treated using a BCS mean field theory, which is diagonalized using Bogoliubov-de Gennes equations. The solutions to these equations are allowed excitations, including the zero-mode [49].

Furthermore, in the presence of more than one vortex, a Cooper pair may be broken such that one or two of its constituents are localized within the correlated zero-mode of the vortex cores. A ground state is a superposition which has equal probability for the vortex core to be empty or occupied by one of these fermions [56]. If one vortex encircles another vortex, the phase it acquires will differ by π depending on whether the stationary vortex is occupied or not. Finally, since the ground state is a superposition with equal weights for the two possibilities, this relative π phase shift could transform the system from one ground state to another [56]. Importantly, the information about vortex occupation is stored *topologically*, not locally; only *pairs* of vortices may be occupied or unoccupied, and this occupation can only be changed *topologically*, by braiding the quasiparticles. Small local interactions with the environment cannot change the occupation of a single vortex. Thus, the entangled quantum state is protected from decoherence.

2.2.4 Topological Quantum Computation

We have introduced the general concept of quantum computation, argued that quantum computers would be useful, and discussed decoherence as a main pitfall in actually building a QC. We have introduced anyonic particles, which acquire phase in nontrivial *fractions* of 2π, and identified a physical system (FQHE) where anyons exist. We then outlined how the Moore-Read quantum Hall wave function, which may describe the FQHE state at $\nu = 5/2$, would lead to *non-Abelian* anyons due to the quantum entanglement of vortex zero-modes and their possible occupation by a fermion. So, finally, we are in a position to discuss topological quantum computation and how it could be done using the $\nu = 5/2$ state.

A nice introduction to topological quantum computation is available online: John Preskill's sixty-eight page lecture notes [23] on the topic give quite a physically-grounded introduction. In the next few paragraphs, I motivate the fundamental concepts and in the process I outline how the Moore-Read $5/2$ state could be used to implement a TQC.

Topological quantum computation depends on the existence of particles in 2D that acquire non-trivial phase when they are braided: TQC *requires* an anyon system. An anyon system is characterized by two sets of rules: the *braiding rules* that describe what happens when two anyons are exchanged, and the *fusion rules* that describe what happens when two anyons are combined.

To implement a TQC, the following physical capabilities are required [23]:

- *Pair creation*; the ability to create pairs of anyons. The simplest possible system would contain "chargeons" (with no effective flux) and "fluxons" (with no charge), but particles with both charge and flux can also be used.

- *Pair annihilation*; the ability to bring pairs together and observe whether the pair annihilates completely or (if the pair was carrying some other particle) leaves some detectable particle behind.

- *Braiding*; the quantum gates are performed by exchanging particles to create different members of the topological braid group.

A computation proceeds as follows [23]. Many pairs of anyons are prepared, the pairs are manipulated to form a particular braid, and pairs of anyons are fused to see whether they annihilate completely or not. The braiding operations act on a system with quantum entanglement, which provides the large Hilbert space for quantum computation. The system is then measured by fusion, which is a non-deterministic measurement.

The property of an anyon system that makes it non-Abelian [23] is if for at least some anyon pairs the fusion can occur in two or more different ways. In an Abelian model, any two particles fuse in a unique way. In a non-Abelian model there are some pairs of particles that can fuse in more than one way, and there is a Hilbert space of two or more dimensions spanned by these distinguishable states.

For the non-Abelian Moore-Read anyon model, we can write the fusion rules [53]:

$$\psi \times \psi = \mathbb{I}, \quad \sigma \times \sigma = \mathbb{I} + \psi, \quad \psi \times \sigma = \sigma \tag{2.9}$$

where $\mathbb{I}$ is the ground state (the superfluid condensate), ψ is a single composite fermion (that is, half of a cooper pair), and σ is a charge $e/4$ half-vortex. The fusion rules can be understood physically: when two ψs fuse, they form a Cooper pair and condense into the ground state $\mathbb{I}$. When two σs fuse, they can either reveal that the core was empty ($\mathbb{I}$) or that it contained a fermion (ψ). This is the fusion rule that makes the $\nu = 5/2$ Moore-Read state non-Abelian. The third rule comes from the associativity of the other rules.

The braiding rules for the Moore-Read state are best illustrated with an example [2]. Assume we have four charge $e/4$ half-vortices labeled η_1, η_2, η_3 and η_4. Let η_1 and η_2 form the qubit: if this pair of half-vortices has a fermion in the core then we will call the state of the qubit $|1\rangle$, otherwise it is $|0\rangle$. If we move (say) η_3 around *both* η_1 and η_2, the state acquires some phase if the core is empty, but it acquires that phase *plus* an extra phase factor of -1 if the core is occupied by a fermion. If we instead move η_3 around *only one* of η_1 or η_2, then the state of the qubit flips (that is, an empty vortex acquires a fermion, or a full one loses its fermion)[9].

Das Sarma, Freedman and Nayak [2] have proposed using these braiding rules alone (without taking advantage of the fusion rules explicitly) to at least determine whether the $\nu = 5/2$ state is non-Abelian via an interference experiment[10]. The idea of the experiment is to localize η_1 and η_2 on antidots in a three quantum point contact (QPC) interference device (see Figure 2.1). Two tunneling paths, at QPC-1 and QPC-3, would interfere. Assume for now the interference is positive: $\sigma_{xx} \propto |t_1 + it_2|^2$. Next, η_3 would be allowed to controllably tunnel across QPC-2, which should flip the qubit and change the sign of the interference to $\sigma_{xx} \propto |t_1 - it_2|^2$. If the interference changes as a result of the braid operation, then the $\nu = 5/2$ state must be non-Abelian. This proposal is exceptionally ambitious. It is however, the proposal that motivated our own experimental effort at $\nu = 5/2$.

Shortly after Das Sarma, Freedman and Nayak published their proposal, several other authors published modifications that make the experiment simpler but still capable of probing non-Abelian statistics of the $\nu = 5/2$ state [3–6]. These other proposals all require the use of gates to manipulate the $\nu = 5/2$ state, and typically call for tunneling of quasiparticles between the $\nu = 5/2$ edge states.

In the remaining few sections of this introduction, the tone will become much more experimental. I will review prior experimental work at $\nu = 5/2$, discuss our more immediate experimental goals and results, and provide a brief outlook for future experiments.

[9] The truly goal-oriented researcher would call this operation a NOT gate.

[10] As far as I know, nobody has proposed a way to take advantage of the fusion rules. Presumably a scheme with fusion would eliminate the need to measure the system using interference.

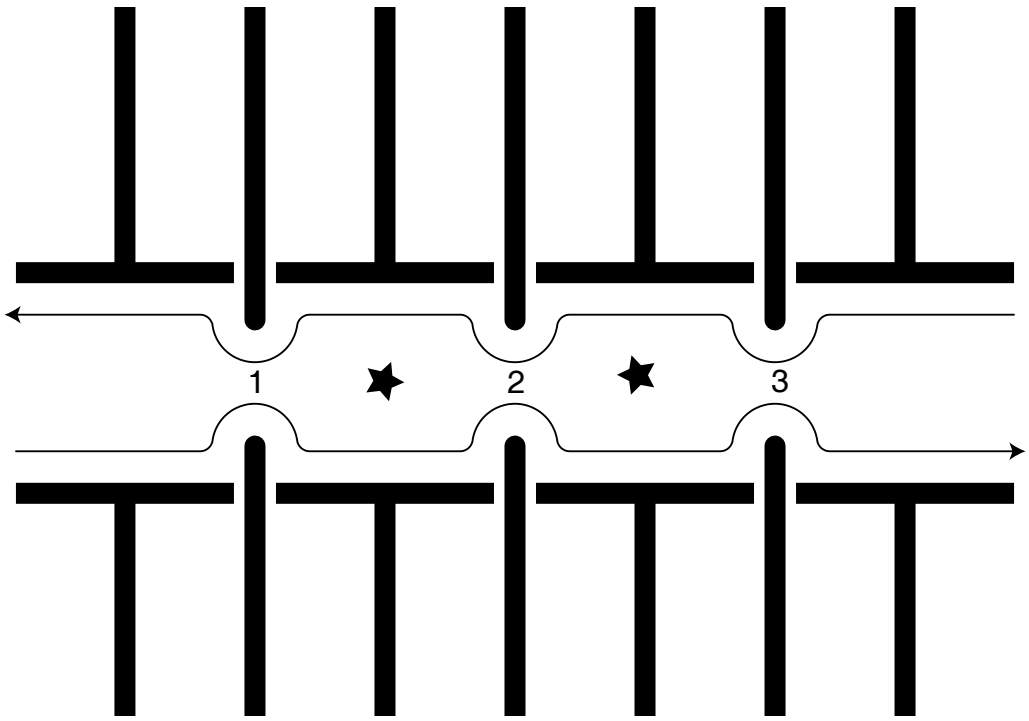

Figure 2.1: Artist's rendering of the device proposed by Das Sarma, Freedman and Nayak. The current flows along the edges as indicated by arrows. Tunneling occurs at the QPCs labeled 1 and 3. The two tunneling paths will interfere either constructively or destructively, influencing the conductance. The two half-flux quasiparticles of a qubit are localized on the two stars. Another half-flux may tunnel at QPC 2. If the $\nu = 5/2$ state is non-Abelian, this braiding operation will switch the interference from constructive to destructive or *vice versa*.

2.3 Prior experimental work

In 2005, when Das Sarma, Freedman and Nayak [2] published their method to experimentally study the non-Abelian statistics of the $\nu = 5/2$ state, it immediately prompted several experimental groups (including our group, of course) to begin studying the manipulation and measurement of the $\nu = 5/2$ state in mesoscopic devices. In terms of studying $5/2$ with gates or in etched structures small enough to observe tunneling between edge states, I am not aware of any published prior experimental work. However, a tremendous amount of experimental work *has* been done to study the $\nu = 5/2$ state in the bulk, and to study *other* FQHE states using QPCs.

Prior $\nu = 5/2$ experiments

The first quantized R_{xy} plateau at $\nu = 5/2$ was observed by Willett and coworkers in 1987 [45]. At that time, the discovery of an even-denominator FQHE state was somewhat of a surprise (although Halperin, four years earlier, had already proposed the possibility of boson-like bound-electron pairs [57]), and there was certainly no consensus then (or even now) about the physics of the state. Over the two decades since then, the quality of available 2DEG GaAs/AlGaAs heterostructures has improved tremendously. The measured $5/2$ energy gap (Δ) has increased from $\Delta = 52\,\mathrm{mK}$ in 1988 [58] to more than 500 mK today [2]. At the present time, the quality of the 2DEG has become so good that the $\nu = 5/2$ state is just one (relatively stable) phase out of many exotic phases that can be observed between $\nu = 3$ and $\nu = 2$ [59]. Important works using tilted magnetic

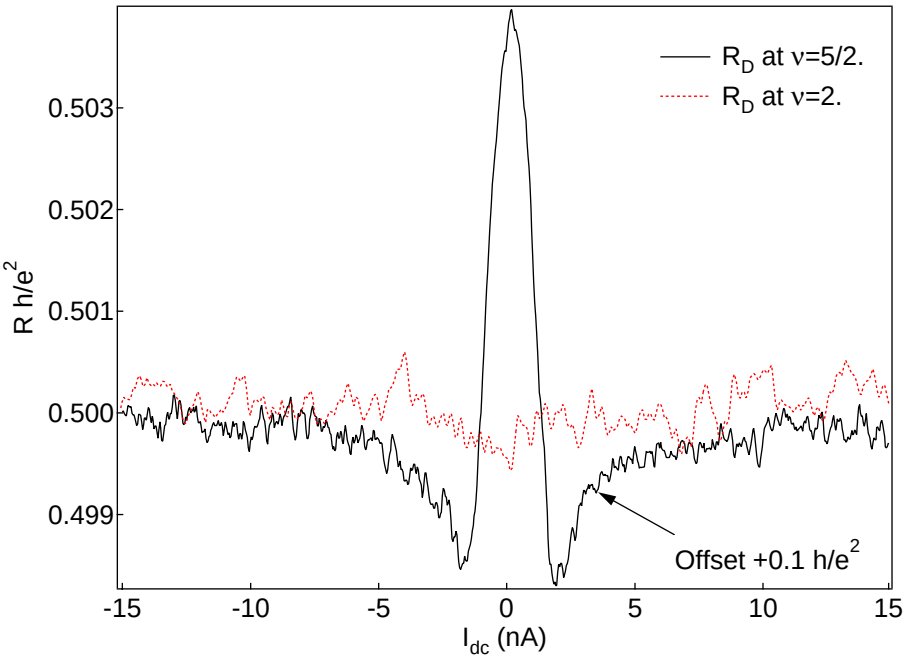

Figure 2.2: Comparison of the I-V characteristic for an IQHE ($\nu = 2$) and FQHE $\nu = 5/2$ plateau. R_D is, in fact, dV/dI, the differential resistance. The IQHE state shows ohmic behavior, while the FQHE behavior is highly nonlinear due to a complicated tunneling density of states at very low temperature and voltage. The FQHE curve is seen to approach ohmic behavior at high I_{dc}.

fields [60, 61] and variable-density samples [62] have led to the conclusion that the $\nu = 5/2$ state is *probably* spin-polarized, which tentatively rules out some competing theoretical explanations. Ongoing experimental work [63] is likely to clarify the spin-polarization properties of the bulk $5/2$ state even further.

Prior FQHE tunneling experiments (and some theory)

The use of a QPC to selectively backscatter fractional edge channels for $\nu < 1$ was experimentally demonstrated as long ago as 1990 by Kouwenhoven and coworkers [64]. Camino, Zhou and Goldman have observed the $\nu = 1/3$ plateau in an etched device with self-aligned gates [65].

In addition to selectively backscattering edge states, a QPC can bring edge states into close enough proximity to allow tunneling between them. For FQHE edge states, including $5/2$ [66], this is predicted [67] to cause the longitudinal resistance to diverge at zero temperature and zero voltage, when *all* of the current tunnels into the counterpropagating edge. Of particular relevance to our results, the theoretical I-V characteristic for tunneling between FQHE edge channels has a very distinct shape [68], illustrated in Figure 2.2. The peak at $I_{dc} = 0$ and the minimum at intermediate I_{dc} are understood to be signatures of tunneling between FQHE edge states [68]. For IQHE edges states the tunneling behavior is ohmic. This behavior has been observed experimentally [69, 70], and found to be in quantitative agreement with theory [29, 68, 71, 72].

2.4 Impact of this work and future directions

The effort to probe the statistics of the $\nu = 5/2$ FQHE state has just begun. Prior to our work (described in detail in Chapter 7), only *bulk* experiments on the $\nu = 5/2$ state had been reported. In fact, it was not known whether the $\nu = 5/2$ state could even exist in a confined area, since the state exists only by virtue of exceptionally delicate bulk many-particle correlations. Furthermore, it was not known whether the specialized, ultra-high mobility GaAs/AlGaAs samples that support the $\nu = 5/2$ state (which have δ-doping layers *both* above and below the 2DEG, see Appendix D) could be processed without destroying the $\nu = 5/2$ state, and whether such material was even gateable using standard top-gate depletion techniques. Furthermore, although the $\nu = 5/2$ state exhibits all the behaviors of a compressible quantum Hall state, there was no experimental evidence that it would definitely even support an edge channel capable of tunneling. Although the existence of edge channels has never been in serious doubt, experimental confirmation is always important, especially since the theoretical proposals to probe the statistics at $\nu = 5/2$ require interference of edge channels. Our experiments have addressed all of these points.

We found that our standard nanofabrication procedure *did* degrade the 2DEG, but I developed an improved procedure to fabricate Hall bars and nanoscale devices without affecting the wafer mobility or the quality of $\nu = 5/2$ features. My complete nanofabrication recipe is printed in Appendix C.

Another difficulty was that the growth parameters that produce these remarkable bulk materials are not necessarily compatible with easy gating. We tested quite a few wafers with good $\nu = 5/2$ features that were ungateable due to switching noise, giant gate drift, unmanageable hysteresis and irreversibility of applied gate-voltage[11]. Eventually, we found a wafer that happened to have both manageable gates *and* good bulk $\nu = 5/2$ features. Unfortunately, at this time there is no clear correlation between growth parameters and useable gates, although some pattern could emerge as we test even more wafers. Incidentally, we also found that all materials were utterly ungateable after illuminating the (cold) sample with an infrared LED[12].

We have observed plateau-like features near $\nu = 5/2$ and $\nu = 2\,1/3$ in QPCs with 1.2 µm and 0.8 µm spacings between the gates. At temperatures above about 18 mK, the plateaus disappear. Below this temperature, the resistance of the plateau-like feature is higher than the bulk-quantized value of $0.4\,h/e^2$, and increases as temperature is decreased. The I_{dc} traces near $\nu = 5/2$ and $\nu = 2\,1/3$ in these QPCs exhibit a characteristic shape, showing a peak in resistance at $I_{dc} = 0$ nA, a minimum near $I_{dc} = 1.2$ nA, and approaching a constant value at higher currents. These observations are consistent with the formation of a gapped, incompressible FQHE state in the QPC at these filling fractions, with QPC-induced tunneling between the edge states. In a QPC with 0.5 µm spacing between the gates, we do not observe a plateau-like feature at any temperature, and the I_{dc} characteristic is flat for the entire range between $\nu = 3$ and $\nu = 2$. This suggests that in our sample no incompressible states form in this QPC, probably due either to confinement or the effects of decreased electron density. All of these measurements were carried out in a magnetic field range where the bulk filling fraction was on the IQHE $\nu = 3$ plateau, while the filling fraction in the QPC was tuned to lower values via the gate voltage.

Interestingly, we find that there is a *peak* in resistance at zero I_{dc} for the $\nu = 5/2$ state, not a *dip* (see Figure 2.3). In the language of an interesting paper by Roddaro [70], this means that the 5/2 state behaves like a *particle* tunneling state, not a *hole* tunneling state. Furthermore, although

[11] All "irreversible" gate behavior was reversible upon warming and re-cooling the device.

[12] We did find, consistent with the literature, that illumination improved the bulk FQHE properties of the material

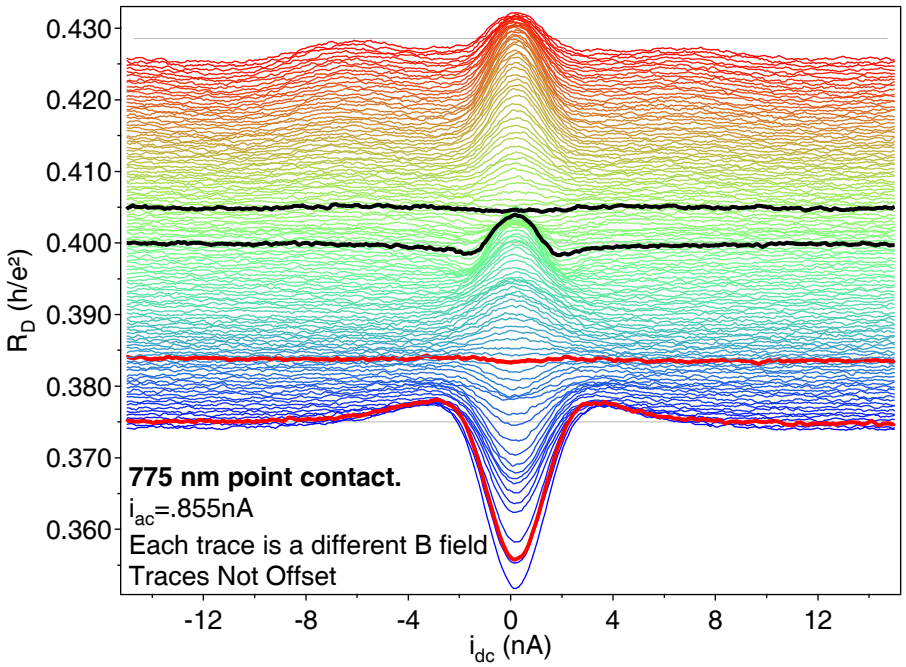

Figure 2.3: A series of I_{dc} curves from the 0.8 µm QPC, each taken at a different magnetic field. The The thick red curve that approaches $R = 0.375\,h/e^2$ at high current is the $\nu = 2^1/_3$ characteristic, which has a dip instead of a peak. The thick black curve that approaches $R = 0.4\,h/e^2$ is the $^5/_2$ characteristic, which shows a peak. At this QPC gate voltage, it was not possible to measure the $\nu = 2^1/_3$ characteristic, because the required magnetic field would take the bulk filling fraction away from $\nu = 3$.

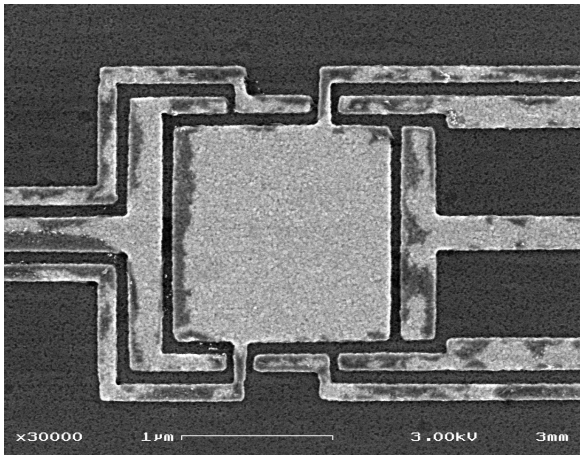

Figure 2.4: A prototype device that could in principle be used to adjust the steepness of the potential in a QPC (using only some of the gates) or in a quantum dot.

we do not observe any plateau-like features for the $\nu = 2^2/_3$ state in the QPC, we do observe a hole-like zero-bias *dip* in resistance for this state, consistent with Roddaro. The impact of these findings upon the theories of $\nu = ^5/_2$ has yet to be fully explored.

Future directions

The opportunities for continued experimental work on FQHE states in general and the $\nu = 5/2$ state in particular are myriad. More detailed studies of the tunneling properties of the $\nu = 5/2$ state, especially at various temperatures, should be carried out. The use of extra gates in and around a QPC or quantum dot to adjust the steepness of the potential profile or increase the electron density inside the QPC (so that, for example, the QPC can have $\nu = 5/2$ while $\nu_{\text{bulk}} = 2$) could possibly help stabilize the $\nu = 5/2$ state within a QPC or quantum dot. For example, see Figure 2.4. It has been suggested [73] that in some cases FQHE states could be *stronger* in a confined area than in the bulk of certain "dirty" samples, if the filling fraction of interest could be restricted to an area (ie, in a QPC or dot) smaller than the scattering length. Devices with more than one tunneling gate could be used to test the theoretical interference predictions. Finally, high-bandwidth studies of the shot-noise of the $\nu = 5/2$ state [74] could turn out to be the best way to probe the statistics of FQHE states, including $\nu = 5/2$.

2.5 Techniques

In this section I discuss some non-obvious experimental details, especially the issue of electron temperature in quantum Hall measurements.

2.5.1 Refrigerator and wiring

We used a Frossati dilution refrigerator with a mixing-chamber base temperature of 5 mK, as measured using a calibrated RuO_2 resistor mounted on the mixing chamber. Coaxial cable was used for electrical wiring from a break-out box, to the refrigerator, and all the way down to Frosatti silver-epoxy filters. The filters were mounted in the bulkhead of a shielded chamber, thermally anchored at the mixing chamber. Within this chamber, the sample was mounted in a socket on a silver cold-finger attached to the mixing chamber. The socket was electrically connected to the filters with copper wire.

2.5.2 LED

Within this chamber we mounted an infra-red light emitting diode. We used digikey part number 516-1262-ND, "Emitter IR 5mm 875nm." We were able to flash this LED at base temperature, although the length of time of the flash was limited to about 5 minutes to avoid crashing the mixing chamber due to excess heat. Attempts to mount the LED at the IVC bulkhead (effectively at the liquid helium bath), bringing the light to the sample with a fiber optic, were unsuccessful. The fiber optic cable was difficult to thermally anchor at the mixing chamber, and therefore heated the sample. Also, the efficiency of the fiber optic coupling, even though we physically mounted the fiber optic into the LED, was poor, and the desired effect of improving the 2DEG mobility was never achieved using this method.

With the LED mounted directly shining on the sample, we used a Keithley 2400 to source 3.0 to 3.6 V with the current compliance limited. Once the LED reached its steady-state temperature, the current at 3.0 V was about 3 mA. We were able to achieve significant improvements in the sample mobility using the LED, although it made the gates unusable.

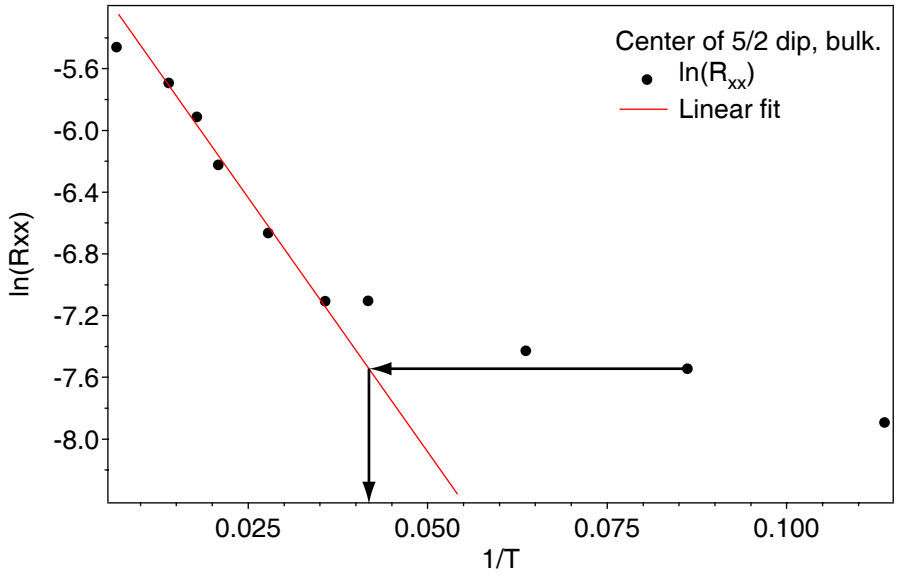

Figure 2.5: An Arrhenius plot of $\ln(R_{xx})$ from the center of a bulk 5/2 dip against mixing chamber temperature. The red line is a fit to a portion of the data, and the slope of this line is used to estimate the activation energy Δ, via $R_{xx} \propto e^{-\Delta/2T}$. The deviation from the line at low temperatures is probably due to variable range hopping. The arrows indicate an ill-advised method to estimate temperature, which requires that the deviation is due to poor cooling of the electrons instead of variable range hopping.

2.5.3 Electron Temperature

With quantum Hall effect measurements it is difficult to measure the temperature of the electrons, because unlike Coulomb blockade peak-width in quantum dots, there is no convenient absolute thermometry. One could attempt to handle this problem using an Arrhenius plot (see Figure 2.5), with $\ln(R_{xx})$—where R_{xx} measured in the center of a quantum Hall minimum—plotted against $1/T_{MC}$—where T_{MC} is the mixing chamber temperature. Assuming the resistance is activated, $R_{xx} \propto e^{-\Delta/2T}$, the plot of $\ln(R_{xx})$ vs $1/T$ should be a straight line. Assuming that at reasonably high temperatures the electrons and the mixing chamber are the same temperature, and assuming any deviations from the line at low temperature are due only to deviations between the mixing chamber and electron temperature, it would be possible to estimate the actual electron temperature using the linear fit (see Figure 2.5). However, these assumptions are quite dubious, and not likely to be valid. In fact, at low temperatures variable range hopping is likely to be the dominant contributor to R_{xx}, which is thought to have a power law temperature dependence [75]. The temperature where hopping becomes dominant is not even necessarily that low: for IQHE it can already be dominant as high as 4 K [76]. So using the center of the quantum Hall dips as a thermometer is not effective.

At lower magnetic fields, it is possible to find a region in field where the R_{xx} minima of the Shubnikov-de Hass oscillations are *just* approaching $R_{xx} = 0$ at base temperature. As the temperature increases, the resistance of these minima is expected to be activated, which in this case is a reasonably good assumtion. Similarly, at low fields, the *amplitude* of the Shubnikov-de Hass oscillations can be analyzed using Dingle plots [77, 78] to estimate a temperature. However, due to the significant difference in Hall resistance between low and high field, there is no guarantee that the low-field electron temperature is applicable to the high-field regime.

Another option is to observe changes in the most delicate quantum-Hall features as temperature changes. In our samples, the feature most sensitive to small changes in temperature near base temperature was the reentrant integer quantum Hall effect (RIQHE). There is no accepted theoretical functional form for the development of this feature with temperature [79], but qualitatively the development of this feature is well known [59, 80, 81]. Very small changes in the temperature lead to quite dramatic changes in the RIQHE features, so it is possible to at least *rank* traces in order of electron temperature. This is actually very useful, since it allows us to check that heating the sample slightly from base temperature actually does make a difference in the electron temperature, which shows at least that the temperature has not saturated. However, since the RIQHE features that are very sensitive from about 30 mK and below are essentially absent at temperatures above about 50 mK, and since there is no functional form for the resistance of these features, it is impossible to make quantitative estimates of the electron temperature.

Chapter 3
Introduction to the spin-orbit coupling experiments

In this chapter, I begin with a brief introduction to the effects of spin-orbit coupling upon transport in a two-dimensional electron gas (2DEG), followed by a brief introduction to conductance fluctuations and random matrix theory. Then, I discuss the place of my work in this field of study. Finally, I record some of our techniques from these experiments.

3.1 Theoretical background

3.1.1 Spin-orbit coupling

Spin-Orbit coupling means that an electron's spin can become coupled to its motion as it moves around in the 2DEG[1]. The way this happens is quite a fascinating relativistic effect: an electric field in the laboratory feels like a magnetic field in the rest frame of the (fast-moving) electron. From special relativity [82], the electron feels effective an magnetic field

$$\mathbf{B}_{\mathrm{SO}} = -(\frac{\mathbf{v}}{c} \times \mathbf{E})(1 - v^2/c^2)^{1/2} \tag{3.1}$$

(where $\mathbf{v}$ is the velocity of the electron) which causes the spin to Larmor precess via $\mathbf{s} \cdot \mathbf{B}_{\mathrm{SO}}$. So we see a magnetic field (or at least an effective magnetic field) creeping into the system even when we did not explicitly apply one. What is really interesting, though, is that this effective field does *not* lift Kramer's degeneracy the way a normal magnetic field would, because spin-orbit coupling does not break time reversal symmetry.

For an electron in a GaAs/AlGaAs heterostructure, spin-orbit coupling can arise via three different mechanisms.

The first two mechanism are due to the GaAs itself: the polar bond between the gallium and arsenic atoms is asymmetric and produces an electric field which produces a spin-orbit contribution known as the *Dresselhaus* term. Silicon, by contrast, is inversion symmetric (it only has one kind of atom) so does not exhibit Dresselhaus-type spin-orbit coupling. Dresselhaus [83] wrote down the full Hamiltonian for 3D conduction band electrons with this type of interaction, but in 2D only two terms survive. One term is linear in the momentum (k) of the electron (note that $k = \sqrt{2\pi n}$ is related to the electron density, which we can control experimentally via a top-gate):

$$H_D^{(1)} = \alpha_1(-\sigma_x k_x + \sigma_y k_y), \tag{3.2}$$

and one term is cubic in k:

$$H_D^{(3)} = \gamma(\sigma_x k_x k_y^2 - \sigma_y k_y k_x^2). \tag{3.3}$$

The third source of spin-orbit coupling in a GaAs/AlGaAs heterointerface is the electric field from the potential which confines the electrons to the 2D boundary. This term, called the

[1] Spin-orbit coupling is not *exclusively* a 2D effect the way anyons are, but I will only talk about the 2D version.

Rashba term [84], will not play a role in symmetrically-doped square wells where there is no net field[2], but does contribute linearly in k for the triangular potential in a single-side-doped sample[3]:

$$H_R = \alpha_2(\sigma_x k_y - \sigma_y k_x), \tag{3.4}$$

The constants in these Hamiltonians, α_1, α_2 and γ have been calculated by adding the spin-orbit interaction as a perturbation to band structure calculations [85, 86], but the answers vary. In Chapter 4 we report how we separately measured these three constants using transport. To explain this measurement, however, I first need to introduce *weak antilocalization*

3.1.2 Weak localization and antilocalization

Ohm's law feels like an old friend. Like an old friend, it sometimes needs a few corrections. Quantum mechanically, the wave function for a particle (such as an electron in a 2DEG) includes a phase that changes as the particle follows any given trajectory. If the electron scatters (changes momentum) several times without losing phase coherence, then interference corrections need to be applied to Ohm's law.

Enhanced backscattering is quite a general phenomenon when coherent waves meet a random array of scatters: it is observed for laser light scattering in a cloudy liquid [87], radar scattering off clouds [88], and electrons scattering off disorder in the 2DEG. When the wave scatters, it follows all kinds of random paths and on average the interference cancels out. However, all closed-loop scattering paths that start and end at the same point are special, because there are always two ways to scatter around a loop—forward and backwards, or forward and *time reversed*—that, unless time reversal symmetry is broken, have exactly the same phase. The interference for these two paths, $e^{i(\varphi_1-\varphi_2)} = e^0 = 1$, will always be *constructive*. So the process for a wave to backscatter right back to where it started is enhanced.

In phase-coherent, weakly disordered[4] conductors, this enhanced backscattering process causes the conductance to decrease by approximately e^2/h, no matter what the overall conductance is[5]. This phenomenon is known as *weak localization* [26, 90, 91]. When at least one magnetic flux quantum threads a closed electron trajectory, then time reversal symmetry is broken. The phase acquired over time-reversed paths will differ by the Aharonov-Bohm phase, the interference will no longer be fully constructive, and weak localization will be lifted. This all only works if the electrons remember their phase, so any path longer than the phase coherence length ℓ_φ will also not contribute to the localization.

So far, we have assumed that the spin of the electrons does not change much over any trajectory. If the sample has negligible spin-orbit coupling, this is often a good assumption. However, if the spin *does* rotate significantly as an electron traverses a closed loop, then we need to include this in the calculation. In Section 2.2.2, we learned that the wave function of a fermion picks up a phase of -1 when rotated by 2π. Spin-orbit coupling can cause such a spin rotation without

[2]For example, the FQHE samples discussed in Chapter 7 are double-doped square-well samples that would be expected to exhibit negligible Rashba effect.

[3]Most of the wafers we have used for top-gate controlled mesoscopic physics have had triangular potentials.

[4]The disorder is considered weak if the conductance is about e^2/h or higher

[5]To see that the magnitude of the correction is independent of the overall conductance requires a subtle argument. For a very clear explanation, including the way this universal correction scales for larger (coherent) conductors of various geometry, I recommend Datta's book [89, Chapter 5].

breaking time reversal symmetry, and the resulting minus sign shows up in the interference[6]. In samples with strong enough spin-orbit coupling, this phase shows up in the transport: the weak localization dip is transformed into an antilocalization *peak* in conductance.

3.1.3 Conductance fluctuations

Another manifestation of quantum interference, which also has a universal magnitude, is universal conductance fluctuations (UCF) [90]. The conductance of a sample is sensitive *in detail* to the position of scatterers in the sample, because the interference depends *in detail* on the path lengths between scattering events. Slightly changing the fermi energy of the sample, or slightly moving some of the scatters can completely change the interference, leading to fluctuations in the sample conductance. Similarly to weak localization, these fluctuations have a universal magnitude of about e^2/h, regardless of the overall conductance of the sample (as long as the overall conductance is higher than about e^2/h). Datta's book offers a very clear explanation of this universality [89].

3.1.4 Physics in the dot and random matrix theory

I turn now turn to the quantum dot [93]. Using nanoscale depletion gates, it is possible to create a zero-dimensional confinement potential for electrons, connected to the 2D reservoirs by quasi-1D quantum point contact (QPC) channels. The confinement causes the continuous dispersion of the free electron gas to break up into discrete allowed energy levels, *à la* the particle-in-a-box problem from introductory quantum mechanics. In this thesis, I only deal with "large" quantum dots (1 μm^2 - 8 μm^2 which contain roughly 100-1000's of electrons), where the picture is more complicated. In fact, the situation is *chaotic*.

The study of quantum chaos is new (only 30 years old) compared to the study of quantum mechanics in general (about 100 years old). A technique to study the quantum chaos in quantum dots, *random matrix theory* (RMT) [94, 95], was (and is) an active area of theoretical research even as we conducted the large-dot experiments reported in Chapters 5 & 6. The exact spectrum of energy levels of a large dot may be too complicated to write down, but according to RMT the statistical distribution of energy level spacings is universal, depending only on the presence or absence of symmetries of the system. Dots can be categorized by symmetry properties such as time reversal symmetry, spin-orbit coupling and spin degeneracy, each category possessing a predictable energy level distribution. RMT can predict certain measurable features of the chaotic system, such as the average and variance of conductance.

The variance of conductance, which arises from the interference of multiple transport paths through the device, is completely analogous to UCF in bulk samples. However, unlike 2D systems, the quantum dot is in many ways an ideal place to study quantum chaos. Because the overall conductance of the device can easily be set to a few e^2/h, the UCF represent a large fractional change in the signal and are easy to measure. Quantum dots can be fabricated in any size, so many of the relevant scales in the problem can be set by the experimentalist. Dots are extremely tunable, so large statistically independent samples of the quantum chaos can be measured just by changing a voltage. Importantly, although dots bestow significant control to the experimentalist, they do not trivialize the problem: In fact, the combined influence of coherence, confinement, electron-electron interactions, spin and spin-orbit coupling [96] makes the physics an extremely rich ground for experimental and theoretical studies.

[6] Because the interference is for *all* electron paths, the spin rotation needs to be averaged, so interference term is $-1/2$, not -1 [92].

3.2 Perspectives on the 2D spin-orbit experiment

In this and the following section, I describe the specific contributions of my PhD research to understanding the problems introduced in this chapter. This section deals with the 2D spin-orbit work reported fully in Chapter 4.

The experiment described in Chapter 4 took place during somewhat of an awakening about the importance of spin-orbit coupling in GaAs/AlGaAs heterostructures. Shortly prior to our experiment, the prevailing view was that there essentially *was* no significant spin-orbit coupling in GaAs. Quoting directly from Beenakker and van Houten [97]:

> We will not discuss the effects of spin-orbit scattering or of superconducting fluctuations, since these may be neglected in [GaAs/AlGaAs heterostructures].

The beginning of the end to that attitude was an important paper by Paul Dresselhaus and coworkers [98] showing weak antilocalization in GaAs/AlGaAs heterostructures that was tunable via a top-gate[7]. Clearly, spin-orbit is *not* negligible in GaAs.

Even before Dresselhaus' experiment, it was known that spin-orbit coupling and antilocalization could be important, especially in other materials such as InGaAs which have very strong spin-orbit coupling. Hikami, Larkin and Nagaoka [99] had included a spin-orbit term in a formula for the shape of weak localization in a magnetic field. Knap and coworkers extended the theory to include different spin-orbit mechanisms [85], but all of these theories used a diffusive approximation, and were not actually applicable to the very clean, ballistic GaAs samples that Dreselhaus, ourselves and others were measuring.

Meanwhile, *spintronics* [100, 101] (the manipulation of electron spin without destroying phase coherence) was becoming a "hot" topic in condensed matter physics. Instead of neglecting spin-orbit coupling, people were employing it as a key feature in devices such as the "Datta and Das" coherent spin rotator [89] and spin-orbit-based spin-filters [102, 103].

This was the state of the field when we were doing our experiment. People wanted to use spin-orbit coupling to make spin-transport devices, but there was no applicable theory to explain antilocalization, one of the most easily observed effects of spin-orbit coupling, in high-mobility GaAs heterostructures. Moreover, although the three materials-specific spin-orbit constants had been calculated [85, 86], and measured using Raman spectroscopy [104], they had never been separately measured using transport. Knowledge of these three constants (see Section 3.1.1) is especially important for spintronic applications, because they affect the spin precession for electrons traveling along specific crystallographic directions; in fact, at certain densities, there could be certain directions where there is *no* precession.

As far as I know, our experiment [105] was the first time that the spin-orbit strength was tuned *in situ* with a gate voltage from complete weak localization to antilocalization. Moreover, our paper included a new theory of antilocalization that was applicable to clean, ballistic (meaning the spin-orbit length was longer than the mean free path) samples. The combination of the theory and our gate-voltage dependent data allowed us to separately measure the contributions of the three spin-orbit mechanisms (Rashba, linear Dresselhaus and cubic Dresselhaus).

In the years since we published our experiment [105], the interest in spintronics has continued [106], and there have been many interesting experimental advances, such as a spin laser [107]. Theoretical proposals for new spintronic devices, such as "Electric-dipole induced spin resonance in disordered semiconductors" published this year in *Nature Physics* [108], appear regularly.

[7] It is surprising but apparently true that writing important papers about spin-orbit coupling is a hereditary trait.

Although it seems like *practical* applications of spintronic devices may need to wait for advances in materials [106], especially (perhaps) magnetic semiconductors, the *scientific* progress spurred by spintronic research is ongoing. For example, Schliemann, Loss and Westervelt [109] have proposed a method to study *zitterbeweung*—a long-standing prediction of relativistic quantum mechanics that leads to an oscillatory term in the Hamiltonian—using spin-orbit scattering in GaAs heterostructures. Another interesting active avenue of research has to do with the importance of Berry's phase in spin-orbit systems [110–112], a point we also highlighted in our paper.

These papers [106, 109, 110] demonstrate one of the two main ways our paper has had an impact on the field of spintronics. Our result is often cited in the theoretical literature when quantitative values of the three spin-orbit materials constants are required to make predictions. The second impact our paper has had is to provide a valid theory to fit other spin-orbit measurements—mostly, it seems, in other materials systems such as InSb/InAlSb. Every so often I receive an email like this one[8], which arrived on 19 Dec, 2006:

> Jeff-
>
> I don't believe we have met, however David Goldhaber-Gordon recommended that I contact you in regards to a physics problem.
>
> I have a group at the University of [somewhere], doing transport measurements on InSb/InAlSb quantum wells for the last few years. Recently we have been doing some low field measurements. InSb has enormous spin-orbit coupling, so as you might suspect, we get a significant anti-weak localization signal. Additionally the samples are of relatively high mobility (>100,000 cm^2/Vs) compared to non-GaAs systems. Some of our samples are in the ballistic regime where the mean free path exceeds the magnetic length.
>
> We have been trying to fit our data with the ballistic theory introduced in a PRL on which you a co-author (PRL, 90 76807 (2003)). We have not found this to be easy. David tells me that you were the fitting expert for the previous gated GaAs results. I was wondering if you could share some insights with us.
>
> Thanks in advance.

This email simultaneously illustrates a feature of our paper and a weakness. The feature is that ours is still essentially the only theory that is applicable in the ballistic regime for fitting antilocalization data. The weakness is that the formulas really are a bear to work with, although I guess they are what they are based on physics.

3.3 Perspectives on the quantum-dot experiments

In this section, I discuss the specific contributions to the literature of the quantum dot experiments described in Chapters 5 & 6. These two chapters (and two papers [113, 114]) present results on a single overarching topic: the study of an extremely rich many-body physics problem. The distinction between the two chapters is that Chapter 5 deals mainly with average conductance while Chapter 6 is primarily about variance.

Just before we measured the spin-orbit properties in our 2D sample, Folk and coworkers [96] had noticed something unexpected about UCF in a quantum dot. Folk's experiment was designed

[8] To protect the privacy of the sender, I have removed names and places

to try to determine whether electron-electron interactions break spin degeneracy in a quantum dot by applying an in-plane field. In Folk's words [96]:

> The original concept for the measurement was that if the system were spin degenerate at low field, then a large in-plane field would lift the degeneracy via Zeeman splitting, with associated changes in the amplitude of conductance fluctuation. If, on the other hand, spin degeneracy at low field were already lifted by interactions, then a large parallel field would not alter spectral statistics and hence conductance fluctuation amplitude. Surprisingly, we find that the conductance fluctuations are indeed suppressed by a strong parallel field (suggesting degeneracy at low field), but in many cases by a significantly greater factor than can be understood in terms of a simple breaking of spin degeneracy. At the end of the paper, we suggest a possible explanation for this large suppression as resulting from field-dependent spin-orbit scattering.

Something unexpect was going on, and the cause was probably spin-orbit coupling. Halperin and coworkers published a theory paper (the very next letter after Folk) supporting spin-orbit as the explanation [115].

Meanwhile, Dominik and I had a chip with strong, well-studied spin-orbit coupling in the 'fridge. We pulled the chip, Dominik made quantum dots, and we got to work trying to sort out what was going on. As we were measuring, Aleiner and Fal'ko published a paper that expanded upon Folk and Halperin's theory that spin-orbit coupling was involved; in fact, they identified "all possible symmetry classes which arise from the interplay between SO coupling and Zeeman splitting in a disordered or chaotic semiconductor quantum dot and describe all the physically achievable parametric dependencies treated as crossovers between distinct symmetry classes," [116]. In other words, they massively expanded the applicability of random matrix theory. Our work [113] provided *quantitative* confirmation of these theories, which represents quite an advance in the understanding of a very complicated many-body problem in physics.

The only small detail is that our results did *not* agree quantitatively with the theory in fairly high parallel magnetic fields. It turns out that this did not represent a failure of the theory, just an opportunity to add one more detail. The same year we were measuring, Fal'ko and Jungwirth [117] and Meyer and Alt'shuler [118, 119] published papers correcting the naive view that in-plane fields influence only the Zeeman energy without affecting the orbital physics. In fact, the parallel field can break time reversal symmetry and couple to the orbital motion of electrons. Adding the Fal'ko/Jungwirth terms to the Aleiner and Fal'ko theory allowed us to understand the average conductance and conductance fluctuations in our dots of various sizes (and with a top-gate) in materials with strong and weak spin-orbit coupling.

Our paper, along with the theory papers I mentioned above—and of course Folk's first observations—helped open up an entire field where spin-orbit coupling and quantum dots are used to understand and control spin. Theoretical and experimental papers continue to report increasingly sophisticated techniques, as exemplified by a recent Letter [120], where single-electron resonant tunneling spectroscopy is used in conjunction with the anisotropy of spin-splitting to measure the relative strength of Rashba and Dresselhaus spin-orbit mechanisms in a quantum dot.

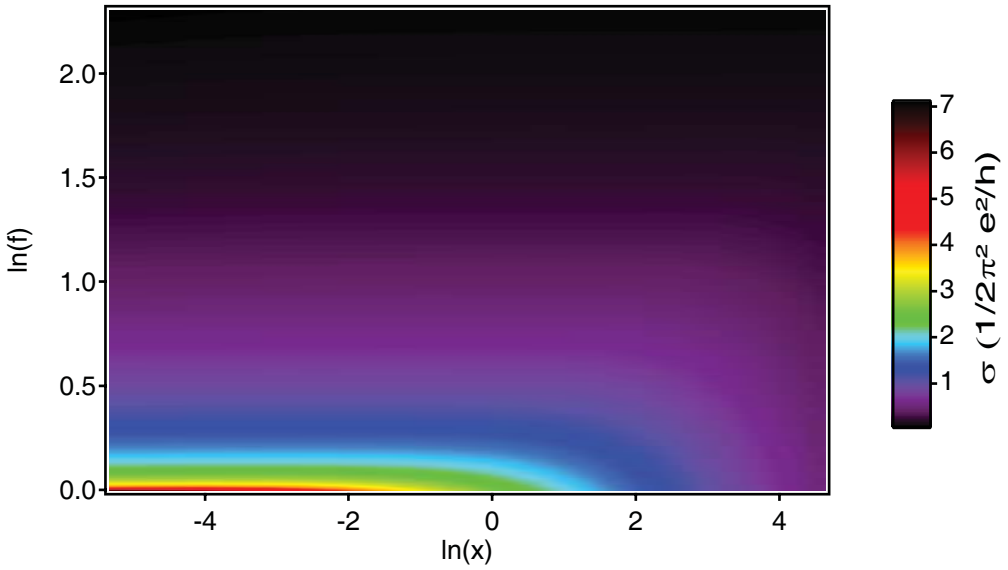

Figure 3.1: This is our calculation of the function $C(f, x)$, the Cooperon term, in Equation 4.2.

3.4 Techniques

3.4.1 Data Acquisition

The data for the 2D paper (Chapter 4) was difficult to acquire because a typical localization feature was only about 0.1% of the overall signal. In fact, it was virtually impossible to see any localization peaks or dips in any single magnetic field trace. In order to achieve acceptable signal-to-noise ratios in finite time, we took hundreds of traces and averaged them. This turned out to be faster—that is, we measured more statistically independent points in a given amount of time—than turning the time constant on the lock-in way up, since the overall noise between successive points was typically larger than the change in the signal.

We also used the transformer on the Princeton Applied Research 124 lock-in amplifiers. Later, we spent a month ensuring the linearity of our measurements. I would tend to avoid using the transformer in the future unless there is really no other way to take data.

3.4.2 Data Analysis

The data acquisition for the 2D paper required very careful measurements, but the data analysis turned out to be even harder. We first tried to fit our data using existing theories [99, 122], but these theories did not yield useful results, even though the fits looked quite acceptable, because they were designed for diffusive samples and were not valid in our ballistic sample. Once we arrived (with Yuli's help) at the correct theory to use, things actually become even harder. The heart of the theory is the Cooperon function, which is the sum of an infinite sum of several integrals. None of them converge particularly fast. In the end, we had the idea to calculate the function only once for a massive 2D parameter space. The result is shown in Figure 3.1. The function is at least smooth. With such slowly converging integrals, we wanted to somehow check that our numerics were working correctly. Fortunately, Zduniak [121] had calculated the Cooperon function in certain limits, and our results matched his (see Figure 3.2), so we were able to proceed with confidence that our numerical methods were correct. The full source-code used for our Cooperon calculation

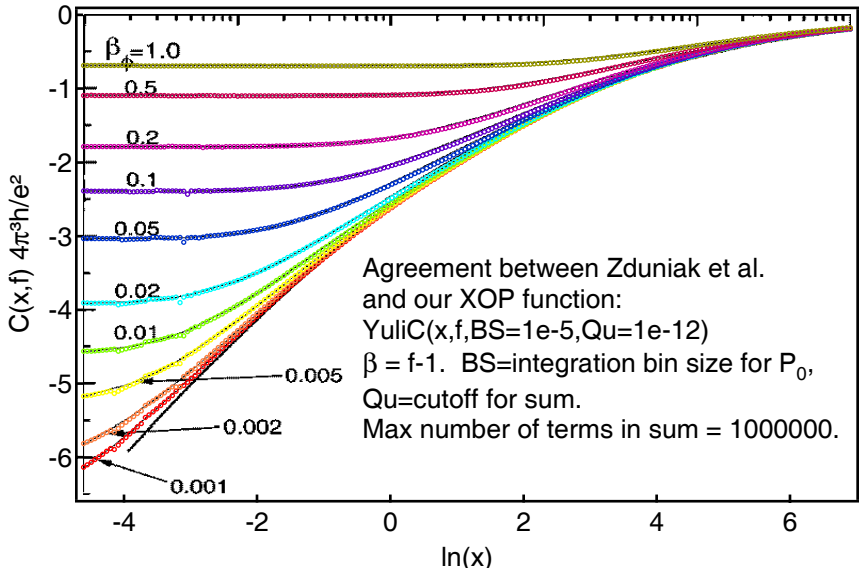

Figure 3.2: We were able to check our numerical methods (colored points) against previously published calculations [121] (black lines).

is listed in Appendix E.

Chapter 4
Gate-Controlled Spin-Orbit Quantum Interference Effects in Lateral Transport

J. B. Miller*, D. M. Zumbühl, C. M. Marcus
Department of Physics, Harvard University, Cambridge, Massachusetts 02138
**Division of Engineering and Applied Science*
Harvard University, Cambridge, Massachusetts 02138

Y. B. Lyanda-Geller
Naval Research Laboratory, Washington, D.C. 20375

D. Goldhaber-Gordon
Department of Physics, Harvard University, Cambridge, Massachusetts 02138
Department of Physics, Stanford University
Stanford, California 94305

K. Campman, A. C. Gossard
Materials Department, University of California at Santa Barbara
Santa Barbara, California, 93106

In situ control of spin-orbit coupling in coherent transport using a clean GaAs/AlGaAs 2DEG is realized, leading to a gate-tunable crossover from weak localization to antilocalization. The necessary theory of 2D magnetotransport in the presence of spin-orbit coupling beyond the diffusive approximation is developed and used to analyze experimental data. With this theory the Rashba contribution and linear and cubic Dresselhaus contributions to spin-orbit coupling are separately estimated, allowing the angular dependence of spin-orbit precession to be extracted at various gate voltages.

[This chapter is published in Phys. Rev. Lett. **90**, 76807 (2003)]

4.1 Introduction

An important component along the path toward realizing quantum “spintronic" devices [100, 101] is a structure that allows manipulation of electron spin without destroying phase coherence. Spin-orbit (SO) coupling has been the focus of recent studies because of its potentially useful role in coherent spin rotators [89], spin interference devices [123], and spin-filters [103, 124]. The mechanisms by which SO coupling affects transport [98, 99, 122, 125] have recently been considered in the context of Aharonov-Bohm (AB) phase and Berry phase [113, 116, 123, 126–129], underscoring the richness of the underlying physics. The results in this and other recent experiments [130] cannot be explained without considering these AB-like effects.

The conductivity of low-dimensional systems shows signatures of quantum interference that depend on magnetic field and SO coupling [26, 90, 99, 122, 131]. In particular, constructive (destructive) backscattering associated with pairs of time-reversed closed-loop electron trajectories in the absence (presence) of significant SO interaction leads to negative (positive) magnetoresistance effects known as weak localization (antilocalization). Antilocalization is the paradigmatic experimental signature of SO coupling in phase coherent electronic systems [125].

In this Letter, we demonstrate *in situ* control of SO coupling in a moderately high mobility GaAs/AlGaAs two-dimensional electron gas (2DEG), inducing a crossover from weak localization (WL) to antilocalization (AL) as a function of an applied top-gate voltage (see Figure 4.1). Theory beyond the diffusive approximation must be used to extract gate-voltage-dependent SO parameters from magnetotransport when the SO precession frequency becomes comparable to the inverse transport scattering time (τ^{-1}) as occurs here, and when the magnetic length becomes comparable to the mean free path. Such a theory, which also takes into account AB-like spin quantal phases and spin-relaxation [132], is developed here and used to estimate *separately* the various SO terms (Rashba, linear and cubic Dresselhaus, defined below) over a range of gate voltages, ranging from WL to AL.

4.2 Previous Theory and Experiments

Conventional WL theories assume SO times much longer than transport scattering times [99, 122, 128] and so cannot be applied to clean materials such as high-mobility 2DEGs. Previous theories that go beyond the diffusive approximation do not treat SO [133, 134], or treat it only as spin-relaxation [121, 135] without accounting for Berry phase effects which play a crucial role, as we show here.

Previous experiments in which SO rates are measured using WL/AL in a gated GaAs heterostructure have not reported *in situ* gate control [98, 136, 137]. Very recently, Koga *et al.* [102] demonstrated gate controlled SO coupling in InGaAs heterostructures using WL/AL, but did not report a full crossover from WL to AL in any single sample. We know of no previous study in which an *in situ* crossover from WL to AL is demonstrated. Modification of Rashba SO coupling using gated quantum wells has been observed using beating patterns in Shubnikov-de Haas oscillations in InGaAs [138, 139], InAs/AlSb [140] and HgTe [141]. Gate controlled SO coupling in GaAs 2D hole systems [142–144] has also been investigated using beating of Shubnikov-de Haas oscillations. The angular variation of SO coupling in GaAs quantum wells has been measured using Raman scattering [104], but to our knowledge has not been extracted from transport data.

4.3 Theory of Two-Dimensional Magnetotransport with Spin-Orbit Coupling beyond the Diffusive Approximation

The Hamiltonian for conduction band electrons in a [001] 2DEG is $\mathcal{H} = \frac{\hbar^2 k^2}{2m^*} + (\sigma \cdot \Omega)$, where m^* is the effective mass, $k = |\mathbf{k}|$ ($\mathbf{k} = (k_x, k_y)$) is the in-plane wave vector, $\sigma = (\sigma_x, \sigma_y)$ is the Pauli spin operator and $\mathbf{\Omega} = (\Omega_x, \Omega_y)$ is the total SO frequency. $\mathbf{\Omega} = \mathbf{\Omega}_{D1} + \mathbf{\Omega}_{D3} + \mathbf{\Omega}_R$ can be written as the vector sum of linear ($\mathbf{\Omega}_{D1}$) and cubic ($\mathbf{\Omega}_{D3}$) Dresselhaus terms and the Rashba term ($\mathbf{\Omega}_R$),

$$\mathbf{\Omega}_{D1} = \alpha_1 \left(-\hat{\mathbf{x}} k_x + \hat{\mathbf{y}} k_y\right)/\hbar, \tag{4.1a}$$

$$\mathbf{\Omega}_R = \alpha_2 (\hat{\mathbf{x}} k_y - \hat{\mathbf{y}} k_x)/\hbar, \tag{4.1b}$$

$$\mathbf{\Omega}_{D3} = \gamma (\hat{\mathbf{x}} k_x k_y^2 - \hat{\mathbf{y}} k_x^2 k_y)/\hbar. \tag{4.1c}$$

where γ arises from the lack of inversion symmetry of the GaAs crystal, while $\alpha_1 = \gamma \langle k_z^2 \rangle$ also depends on the thickness of the wave function in the quantization direction. The Rashba coefficient α_2 depends on the potential profile of the heterointerface. In fitting the data below, we assume the effect of gate voltage, V_g, on Ω ($\equiv |\mathbf{\Omega}|$) is through the carrier density, $n = k^2/2\pi$. Good agreement between theory and experiment (Figure 4.2) supports this assumption, as do previous studies of SO coupling in single-interface heterostructures [85]. Although α_2 can be treated as directly proportional to a *uniform* electric field [145], the magnitude of α_2 in a single-interface heterostructure originates mainly from the band-offset at the heterointerface, which is essentially independent of V_g [86, 140].

The symmetry of the linear (in k) SO terms, $\mathbf{\Omega}_{D1}$ and $\mathbf{\Omega}_R$, allows these terms to be represented as a spin-dependent vector potential $\mathbf{A}$ that affects the orbital motion and phase of electrons, $\sigma \cdot (\mathbf{\Omega}_{D1} + \mathbf{\Omega}_R) \propto \mathbf{k} \cdot \mathbf{A}$ [116, 123, 126–129]. That is, the linear terms affect electronic interference as a spin-dependent AB-like effect. In contrast, the cubic term, Eq. (1c), upon removing terms with the symmetry of Eq. (1a), only causes spin relaxation in the diffusive regime (although it also can produce AB-like effects in the quasi-ballistic regime [123]).

To develop the theory of 2D magnetotransport with SO coupling beyond the diffusive approximation [132], we follow Refs. [133–135], which treat the quasi-ballistic case $\ell_B < \ell$ ($\ell_B = \sqrt{\hbar/2eB}$ is the magnetic length and ℓ is the transport mean free path) without spin-orbit coupling. The approach is to introduce an operator $P = G^R_{\epsilon+\omega}(\mathbf{r}_1, \mathbf{r}_2, \sigma_1) G^A_{\epsilon}(\mathbf{r}_1, \mathbf{r}_2, \sigma_2) \hbar/2\pi\nu\tau$ for the probability of an electron to propagate both forward and backward along a path segment from $\mathbf{r}_1$ to $\mathbf{r}_2$, where G^R (G^A) are single-electron retarded (advanced) Green functions, $\sigma_{1(2)}$ are the Pauli spin operators for particle moving forward (backward), ν is the density of states per spin, and τ is the scattering time. The interference contribution from the n^{th} traversal of a closed path is given by the trace of $(P)^n$. In the presence of SO coupling of the form in Eq. (4.1), formulas in [134] remain valid once a summation over spins is included in the trace.

Introducing the total spin of interfering partial waves, $\mathbf{S} = \sigma_1 + \sigma_2$, we write $Tr[(P)^n] = \frac{1}{2} Tr[(P_1)^n - (P_0)^n]$, where operators P_0 and P_1 describe singlet ($S = 0$) and triplet ($S = 1$) contributions. To calculate $Tr[(P_{0(1)})^n]$, we diagonalize $P_{0(1)}$. We find that when $\mathbf{\Omega}_{D1}$ and $\mathbf{\Omega}_R$ are taken into account, $P_{0(1)}$ has the same eigenfunctions as the Hamiltonian $\mathcal{H}$ for particles with charge $2e$, spin $\mathbf{S}$ and spin frequency $2\mathbf{\Omega}$: $\mathcal{H} = \frac{\hbar^2}{2m^*}(\mathbf{k} - 2e\mathbf{A}_{em} + 2e\mathbf{A}_S)^2$, where $\mathbf{A}_{em}$ is the vector potential associated with the applied perpendicular magnetic field, B, and $\mathbf{A}_S = \frac{m^*}{2e\hbar^3}(-\alpha_1 S_x - \alpha_2 S_y, \alpha_2 S_x + \alpha_1 S_y)$ is the SO vector potential. For $S = 0$, the eigenstates are Landau levels for a charge $2e$ particle in the magnetic field B, analogous to the spinless problem [135]. For $S = 1$, eigenstates of $\mathcal{H}$ and P_1 in general require a numerical solution, although analytic solutions exist when either

α_1 or α_2 equals zero [132]. An analytic solution is found when both α_1 and α_2 may be nonzero, when $\ell_B < \lambda_{so}$, where $\lambda_{so} = (2\alpha_{1(2)}m^*/\hbar^2)^{-1}$ is the distance over which spin rotates appreciably (if $\ell > \lambda_{so}$) or dephases (if $\ell < \lambda_{so}$) due to spin AB-like effects. Performing a unitary transformation $\mathcal{H} \rightarrow \tilde{\mathcal{H}} = U^\dagger \mathcal{H} U$, with $U = \exp(-ie\mathbf{A}_S \cdot \mathbf{r})$, and expanding in coordinates, we find $\tilde{\mathcal{H}} = \frac{\hbar^2}{2m^*}(\mathbf{k} - 2e\mathbf{A}_{em} + S_z\mathbf{a})^2$, where $\mathbf{a} = H_{\text{eff}}\,\mathbf{r} \times \hat{\mathbf{z}}/(2\hbar^2)$, and $H_{\text{eff}} = 2(\alpha_2^2 - \alpha_1^2)m^{*2}/e\hbar^3$ is the effective SO field. P_1 can then be block-diagonalized for each m ($m = 0, \pm 1$) using the Landau basis for particles with charge $2e$ in the magnetic field $B - mH_{\text{eff}}$. Thus, the effect of $\mathbf{\Omega}_{D1}$ and $\mathbf{\Omega}_R$ is to produce spin quantal phases of the AB type [116, 123, 126–129]. Higher expansion terms to $\tilde{\mathcal{H}}$ describe spin flip processes and can be taken into account by introducing a spin relaxation time τ_{so} and its corresponding field scale $H_{so} = \hbar\tau/(2e\ell^2\tau_{so})$. The resulting quantum interference contribution takes the form [132],

$$\Delta\sigma(B) = -\frac{e^2}{4\pi^2\hbar}\left[\sum_{m=-1,0,1} C(x_{1m}, f_{1m}) - C(x_{00}, f_{00})\right] \tag{4.2}$$

where $x_{Sm} = (B - mH_{\text{eff}})/H_{tr}$ describes the AB dephasing in H_{eff}, $C(x, f_{Sm}) = x\sum_{N=0}^{\infty}\frac{P_N^3(f_{Sm})}{1-P_N(f_{Sm})}$, $P_N(f_{Sm}) = y\int_0^\infty \exp(-yf_{Sm}t - t^2/2)L_N(t^2)dt$, $L_N(z)$ are Laguerre polynomials, $y = (2/|x|)^{1/2}$, and $H_{tr} = \hbar/(2e\ell^2)$. The dephasing factors f_{Sm} are given by $f_{1\pm1} = (1 + (H_\varphi + H_{so})/H_{tr})$; $f_{00} = (1 + H_\varphi/H_{tr})$; $f_{10} = (1 + (H_\varphi + 2H_{so})/H_{tr})$, where $H_\varphi = \hbar/(4eL_\varphi^2)$ and L_φ is the phase breaking length.

Equation (4.2) does not include all B-dependent interference terms, notably excluding Cooper-channel contributions due to electron-electron interactions [90] and a reduction of WL due to electron diffraction effects [133]. Also, in an attempt to capture the effects of cubic terms on H_{eff} and H_{so}, we introduce an effective vector potential $\mathbf{A}_S^* = \mathbf{A}_S + \gamma\frac{m^*}{e\hbar^2}({k_y}^2, -{k_x}^2) \sim \mathbf{A}_S + \gamma\frac{m^*}{2e\hbar^2}(k^2, -k^2)$ which leads to an effective SO field,

$$H_{\text{eff}}^* = 2(\alpha_2^2 - \alpha_1^2 + 2\pi n\alpha_1\gamma - \pi^2\gamma^2n^2)m^{*2}/e\hbar^3. \tag{4.3}$$

Equation (4.2) is applicable when $B > H_{\text{eff}}^*$, which corresponds in the present experiment to B between 20-100 μT depending on V_g (see Figure 5.2). We have confirmed that fitting only to data where $B > H_{\text{eff}}^*$ gives, within error bars, the same results as fitting over the entire measured range of B.

Modification of the commutator $[\mathbf{k} + 2e\mathbf{A}_S^*, \mathbf{r}]$ by $\mathbf{A}_S^*$ induces spin flipping terms $\sim \gamma k^3/4$ in the transformed Hamiltonian $\tilde{\mathcal{H}}^*$. The corresponding $H_{so}^* = \frac{1}{36}\pi^2 m^{*2}\gamma^2n^2/e\hbar$, using its expression in the diffusive regime.

4.4 Experimental Details

We now turn to a discussion of the experiment. Three similarly fabricated samples made on three separate heterostructure materials were measured, all showing qualitatively similar behavior. The sample for which data is presented consists of a GaAs/AlGaAs heterostructure grown in the [001] direction with double δ-doping layers set back 143 Å and 161 Å from the 2DEG and a total distance of 349 Å from the surface to the 2DEG. A 200 μm wide Hall bar with 700 μm between voltage probes was patterned by wet etching. A lithographically defined Cr/Au top gate was used to control density and mobility in the Hall bar over the range n = 1.4-7.0 $\times 10^{15}$ m^{-2} and μ = 3.6-31 m^2/Vs. Measurements were made in a ^{3}He cryostat at temperature T = 300 mK using ac lock-in techniques with bias currents ranging from 50 to 500 nA (depending on the gate voltage).

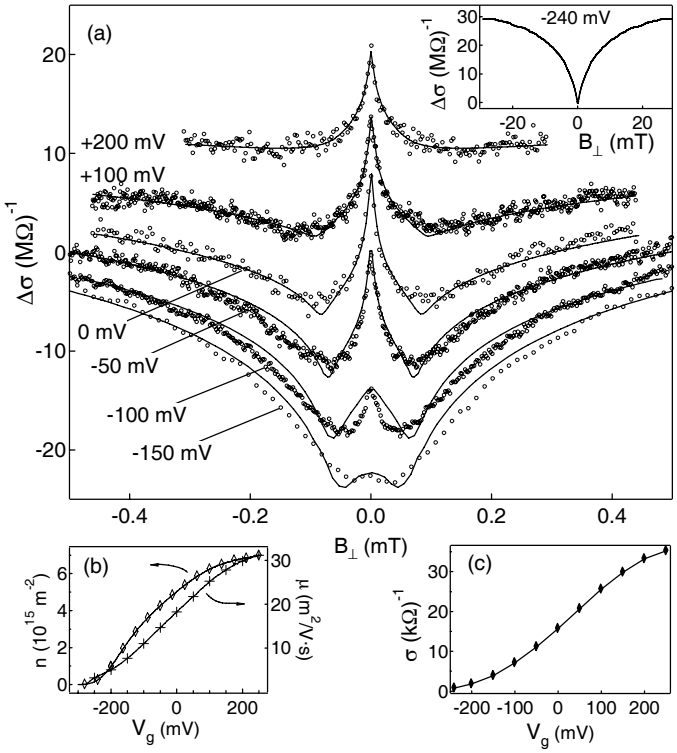

Figure 4.1: (a) Experimental magnetoconductance, $\Delta\sigma = \sigma(B) - \sigma(0)$, (circles) offset for clarity, along with three-parameter fits to Eq. (4.2) (solid curves) for several gate voltages. Inset: Experimental magnetoconductance data for the most negative gate voltage, showing pure WL. (b) Density and mobility as a function of V_g, extracted from longitudinal and Hall voltage measurements. (c) Experimental conductivity, showing strong dependence on V_g. Note that $\Delta\sigma \sim 10^{-3}\sigma$.

At each gate voltage, the bias current was experimentally determined not to affect the results.

4.5 Crossover from WL to AL and Separation of Spin-Orbit Parameters

Figure 4.1 (a) shows the longitudinal magnetoconductance as a function of V_g. A crossover from pure WL (Figure 4.1(a), inset) at $V_g = -240$ mV to essentially pure AL at $V_g = +250$ mV is observed. This crossover demonstrates that a gate can be used to control SO over a wide range, as pure WL corresponds to negligible SO rotations within the phase coherence length L_φ, while AL corresponds to spin rotations $\gtrsim 2\pi$. The solid curves in Figure 4.1(a) are fits of Eq. (4.2) with three free parameters, H_ϕ, H^*_{so}, and H^*_{eff}. H_{tr} is fixed at each gate voltage by measured values of density and mobility.

Figure 4.2 shows extracted parameters H^*_{so} and H^*_{eff} as a function of n^2. H^*_{so} is well described by the predicted linear dependence on n^2, with a best fit (Figure 4.2, solid line) giving $\gamma = 31 \pm 3$ eVÅ^3 with zero y-intercept (see Equation (4.1c)). The density dependence of H^*_{eff} is well described by Equation (4.3), (Figure 4.2, dotted curve), giving fit parameters $\gamma = 28 \pm 4$ eVÅ^3, $\alpha_1 = 4 \pm 1$ meVÅ and $\alpha_2 = 5 \pm 1$ meVÅ. In this way, the three SO parameters α_1, α_2, and γ are separately obtained from transport measurements by explicitly making use of the density dependence of H^*_{eff} and H^*_{so}. Extracted values of H_φ correspond to dephasing times in the range

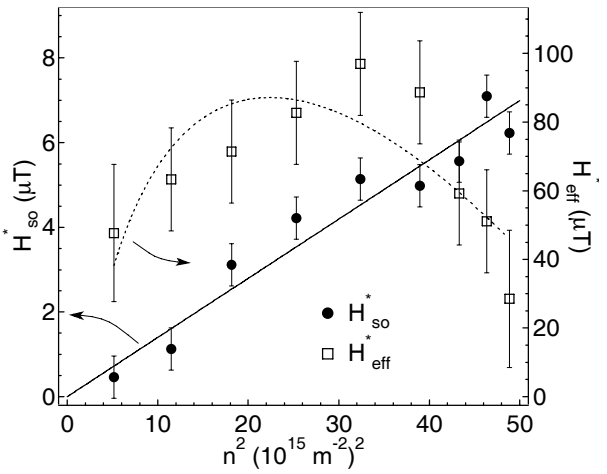

Figure 4.2: Spin-orbit effective fields, H^*_{so} (filled circles) and $H^*_{\rm eff}$ (open squares), as extracted using Eq. (4.2), plotted as a function of sheet density squared. The best fit of Eq. (4.3) to $H^*_{\rm eff}$ (dotted curve) is used to extract γ, α_1 and α_2. Alternatively, the best linear fit to H^*_{so} (solid line) is used to extract γ.

$\tau_\varphi \sim$ 0.1-1.0 ns at 300 mK, which decrease by more than an order of magnitude as temperature is increased to 2.5 K. Within the error bars, H^*_{so} and $H^*_{\rm eff}$ do not depend on temperature over this temperature range.

Figure 4.3(a) displays the magnitudes of the three spin-orbit terms as functions of V_g, n, and μ, determined using Eq. (4.1) and the extracted values of α_1, α_2, and γ. Plotted are values along the [110] direction, $\phi \equiv \tan^{-1}(k_y/k_x) = \frac{\pi}{4}$, where Ω_{D3} is maximum. Error bars indicate uncertainties in the fitting procedure and noise in the data.

4.6 Angular Dependence of Spin Precession Rates

The total spin precession rate, Ω, is plotted as a function of the direction, ϕ, of the electron momentum in Figure 4.3(b). While for most directions Ω is an increasing function of density, it is seen to decrease with increasing density near $\phi = \frac{3\pi}{4}$ and $\frac{7\pi}{4}$. The linear Dresselhaus and Rashba terms (Ω_{D1} and Ω_R) are of comparable magnitude to each other for all densities and in all directions. Near $\phi = \frac{j\pi}{2}$ (j an integer), $\Omega_{D3} \ll \Omega_{D1}, \Omega_R$ and the SO is controlled by the linear terms. For ϕ near $\frac{(2j+1)\pi}{4}$, the cubic term becomes comparable to or even exceeds (at high densities) the linear terms. Depending on ϕ, the linear and cubic terms either add ($\phi \sim \frac{\pi}{4}, \frac{5\pi}{4}$) or subtract ($\phi \sim \frac{3\pi}{4}, \frac{7\pi}{4}$).

The extracted values for γ (31 ± 3 eVÅ^3 using H^*_{so}, 28 ± 4 eVÅ^3 using $H^*_{\rm eff}$) are in good agreement with the value 27.5 eVÅ^3 from band structure calculations [85, 86]. Estimates for α_1 give values for $\langle k_z^2 \rangle$ that correspond to a wave function width of $\sim$ 10 nm in the $\hat{z}$ direction, which is also reasonable. The extracted α_2 corresponds to a uniform [145] electric field $E \sim$ 10 MV/m, using $\alpha_2 = \alpha_0 eE$ and a value of $\alpha_0 = 5.33$ Å^2 from a $\mathbf{k} \cdot \mathbf{p}$ model [85, 86].

4.7 Comparison with previous Theory

We note that previously existing models for WL/AL [85, 122, 128] provide fits to the data that appear qualitatively reasonable, giving values for H_{so} that are $\sim$ 5 times higher than those found

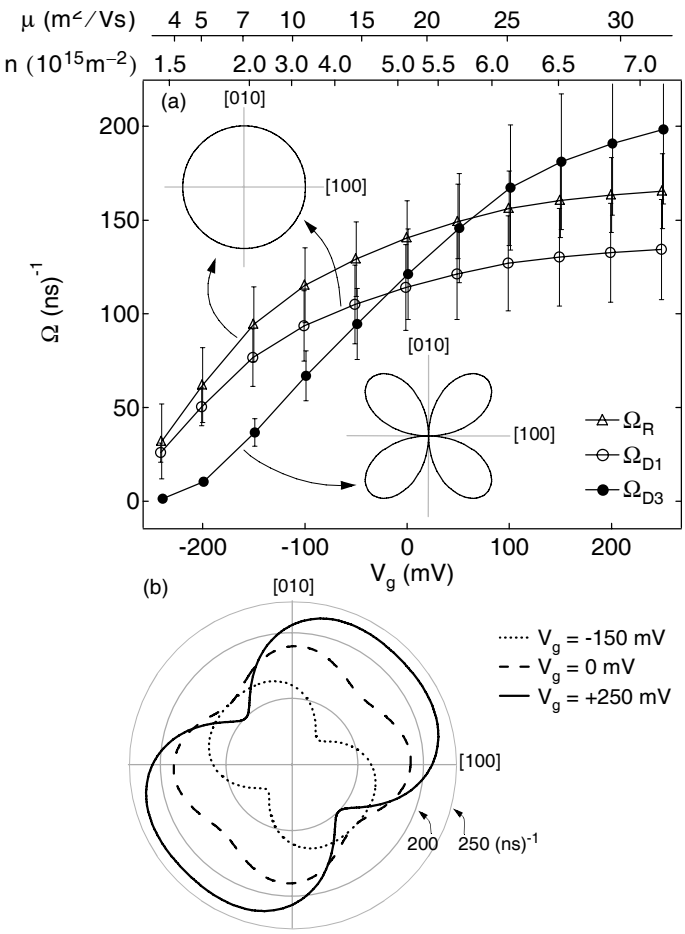

Figure 4.3: (a) Magnitudes of isotropic linear Dresselhaus (Ω_{D1}) and Rashba (Ω_R) terms, and non-isotropic cubic Dresselhaus (Ω_{D3}) term as functions of gate voltage, V_g, density, n, and mobility, μ. Insets show theoretical dependence on momentum direction for the three terms, indicating that the linear terms are isotropic, while the cubic term has a four-fold symmetry and is highly anisotropic. Maximum magnitude (when $\phi = (j + \frac{1}{4})\pi$) is shown for the anisotropic (Ω_{D3}) term. (b) Angular variation of Ω, the magnitude of the total SO precession vector at $V_g = -150$ mV (dotted), 0 mV (dashed), and 250 mV (solid), corresponding to densities of 2.3, 5.0, and 7.0×10^{15} m^{-2} respectively.

using Eq. (4.2). However, these fits also lead to the unphysical result that $\tau_{so} < \tau$. Such unphysical results are not surprising given that, for $V_g > -50$ mV, the SO length, $v_F/\langle\Omega\rangle$, is less than ℓ, while theory [85, 122, 128] assumes diffusive spin evolution $\ell \ll \lambda_{so}, L_\varphi$. Finally we note that a theory for arbitrarily strong SO coupling [129] may also be used to fit this data by including B via L_φ, yielding values for Ω_{D3} and Ω_{D1} for all V_g's which agree with our estimates using Eq. (4.2) to within a factor of ~ 3. However, the theory in [129] does not separate Ω_{D1} and Ω_R terms.

4.8 Conclusion

In conclusion, we have realized an *in situ* gate-controlled crossover from weak localization to antilocalization in a GaAs/AlGaAs 2DEG, experimentally demonstrating that spin rotation can be strongly modulated in a clean, phase-coherent system. New theory addresses spin-orbit effects

in the quasi-ballistic regime and allows separate measurement of the Rashba, linear Dresselhaus, and cubic Dresselhaus terms.

4.9 Acknowledgements

We thank I. Aleiner, H. Bruus and S. Studenikin for illuminating discussions and F. Mancoff for device fabrication. This work was supported in part by DARPA-QuIST, DARPA-SpinS, ARO-MURI, and NSF-NSEC. We also acknowledge support from ONR and NSA (Y. L.-G.), NDSEG (J. B. M.) and the Harvard Society of Fellows (D.G.-G). Work at UCSB was supported by QUEST, an NSF Science and Technology Center.

Chapter 5
Spin-Orbit Coupling, Antilocalization, and Parallel Magnetic Fields in Quantum Dots

D. M. Zumbühl, J. B. Miller*, C. M. Marcus
Department of Physics, Harvard University, Cambridge, Massachusetts 02138
**Division of Engineering and Applied Science*
Harvard University, Cambridge, Massachusetts 02138

K. Campman, A. C. Gossard
Materials Department, University of California at Santa Barbara
Santa Barbara, California, 93106

We investigate antilocalization due to spin-orbit coupling in ballistic GaAs quantum dots. Antilocalization that is prominent in large dots is suppressed in small dots, as anticipated theoretically. Parallel magnetic fields suppress both antilocalization and also, at larger fields, weak localization, consistent with random matrix theory results once orbital coupling of the parallel field is included. *In situ* control of spin-orbit coupling in dots is demonstrated as a gate-controlled crossover from weak localization to antilocalization.

[This chapter is published in Phys. Rev. Lett. **89**, 276803 (2002)]

5.1 Introduction

The combination of quantumcoherence and electron spin rotation in mesoscopic systems produces a number of interesting transport properties. Numerous proposals for potentially revolutionary electronic devices that use spin-orbit (SO) coupling have appeared in recent years, including gate-controlled spin rotators [89] as well as sources and detectors of spin-polarized currents [103, 146, 147]. It has also been predicted that the effects of some types of SO coupling will be strongly suppressed in small 0D systems, i.e., quantum dots [115, 116, 148–150].

In this Letter, we investigate SO effects in ballistic-chaotic GaAs/AlGaAs quantum dots. We identify the signature of SO coupling in ballistic quantum dots to be *antilocalization* (AL), leading to characteristic magnetoconductance curves, analogous to known cases of disordered 1D and 2D systems [85, 98, 99, 105, 122, 125, 151]. AL is found to be prominent in large dots and suppressed in smaller dots, as anticipated theoretically [115, 116, 148–150]. Results are generally in excellent agreement with a new random matrix theory (RMT) that includes SO and Zeeman coupling [116, 150]. Moderate magnetic fields applied in the plane of the 2D electron gas (2DEG) in which the dots are formed cause a crossover from AL to weak localization (WL). This can be understood as a result of Zeeman splitting, consistent with RMT [116, 150]. At larger parallel fields WL is also suppressed, which is not expected within RMT. The suppression of WL is explained by orbital coupling of the parallel field, which breaks time-reversal symmetry [117, 118]. Finally, we demonstrate *in situ* electrostatic control of the SO coupling by tuning from AL to WL in a dot with a center gate.

In mesoscopic conductors, coherent backscattering of time-reversed electron trajectories leads to a conductance *minimum* (WL) at $B = 0$ in the spin-invariant case, and a conductance *maximum* (AL) in the case of strong SO coupling [99, 122]. In semiconductor heterostructures, SO coupling results mainly from electric fields [152] (appearing as magnetic fields in the electron frame), leading to momentum dependent spin precessions due to crystal inversion asymmetry (Dresselhaus term [83]) and heterointerface asymmetry (Rashba term [84]).

5.2 Previous Experiments

SO coupling effects have been previously measured using AL in GaAs 2DEGs [98, 105, 151] and other 2D heterostructures [85]. Other means of measuring SO coupling in heterostructures, such as from Shubnikov-de Haas oscillations [140, 153, 154] and Raman scattering [104] are also quite developed. SO effects have also been reported in mesoscopic systems such as Aharonov-Bohm rings, wires, and carbon nanotubes [123, 130, 155–160]. Recently, parallel field effects of SO coupling in quantum dots were measured [96, 161]. The observed reduction of conductance fluctuations in a parallel field [96] was explained in terms of SO effects [115, 116, 150], leading to an extension of random matrix theory (RMT) to include new symmetry classes associated with SO and Zeeman coupling [116, 150].

5.3 Random Matrix Theory

This RMT addresses quantum dots coupled to two reservoirs via N total conducting channels, with $N \gg 1$. It assumes $(\gamma, \epsilon_Z) \ll E_T$, where $\gamma = N\Delta/(2\pi)$ is the level broadening due to escape, Δ is the mean level spacing, $\epsilon_Z = g\mu_B B$ is the Zeeman energy and E_T is the Thouless energy (Table 5.3). Decoherence is included as a fictitious voltage probe [116, 150, 162–164] with dimension-

A	Δ	τ_d	E_T/Δ	$\epsilon_\perp^{so}/\Delta$	$\epsilon_\parallel^{so}/\Delta$	a_1, a_2	b_2
$^-$m^2	$^-$eV	ns				$(\mathrm{ns})^{-1}\mathrm{T}^{-2}$	$(\mathrm{ns})^{-1}\mathrm{T}^{-6}$
1.2	6.0	0.35	33	0.15	0.04	6.6, 6.6	0.24
5.8	1.2	1.7	73	0.32	0.33	3.2, 0	140
8	0.9	2.3	86	3.6	3.1	1.4, 0.9	3.7

Table 5.1: Dot area $A = L_1 L_2$ (130 nm edge depletion); spin-degenerate mean level spacing $\Delta = 2\pi\hbar^2/m^* A$ ($m^* = 0.067 m_e$); dwell time $\tau_d = h/(N\Delta)$; Thouless energy $E_T = \hbar v_F/\sqrt{A}$; $\epsilon_\perp^{so}/\Delta$ and $\epsilon_\parallel^{so}/\Delta$ for the fits in Figure 5.1; B^2 coefficients a_1 and a_2 from one and two parameter fits; B^6 coefficient b_2 from two parameter fit, see text.

less dephasing rate $N_\varphi = h/(\Delta\tau_\varphi)$, where τ_φ is the phase coherence time. SO lengths $\lambda_{1,2}$ along respective principal axes [110] and [1$\bar{1}$0] are assumed (within the RMT) to be large compared to the dot dimensions $L_{1,2}$ along these axes. We define the mean SO length $\lambda_{so} = \sqrt{|\lambda_1\lambda_2|}$ and SO anisotropy $\nu_{so} = \sqrt{|\lambda_1/\lambda_2|}$. SO coupling introduces two energy scales: $\epsilon_\perp^{so} = \kappa_\perp E_T (L_1 L_2/\lambda_{so}^2)^2$, representing a spin-dependent Aharonov-Bohm-like effect, and $\epsilon_\parallel^{so} \sim ((L_1/\lambda_1)^2 + (L_2/\lambda_2)^2)\epsilon_\perp^{so}$, providing spin flips. AL appears in the regime of strong SO coupling, $(\epsilon_\perp^{so}, \epsilon_\parallel^{so}) \gg \tilde{\gamma}$, where $\tilde{\gamma} = (\gamma + \hbar/\tau_\varphi)$ is the total level broadening. Note that large dots reach the strong SO regime at relatively weaker SO coupling than small dots. Parameters λ_{so}, τ_φ, and $\kappa_\perp$ (a factor related to trajectory areas) are extracted from fits to dot conductance as a function of perpendicular field, $B_\perp$. The asymmetry parameter, ν_{so}, is estimated from the dependence of magnetoconductance on parallel field, $B_\parallel$.

The quantum dots are formed by lateral Cr-Au depletion gates defined by electron-beam lithography on the surface of a GaAs/AlGaAs heterostructure grown in the [001] direction. The 2DEG interface is 349 below the wafer surface, comprising a 50 GaAs cap layer and a 299 AlGaAs layer with two Si ffi-doping layers 143 and 161 from the 2DEG. An electron density of $n \sim 5.8 \times 10^{15}\,\mathrm{m}^{-2}$ [1] and bulk mobility $\mu \sim 24\,\mathrm{m}^2/\mathrm{Vs}$ (cooled in the dark) gives a transport mean free path $\ell_e \sim 3\,^-$m. This 2DEG is known to show AL in 2D [105]. Measurements were made in a ^{3}He cryostat at 0.3 K using current bias of 1 nA at 338 Hz. Shape-distorting gates were used to obtain ensembles of statistically independent conductance measurements [165] while the point contacts were actively held at one fully transmitting mode each ($N = 2$).

5.4 Antilocalization and Confinement Suppression of Spin-Orbit Effects

Figure 1 shows average conductance $\langle g \rangle$, and variance of conductance fluctuations, var(g), as a function of $B_\perp$ for the three measured dots: a large dot ($A \sim 8\,\mu\mathrm{m}^2$), a variable size dot with an internal gate ($A \sim 5.8\,\mu\mathrm{m}^2$ or $8\,\mu\mathrm{m}^2$, depending on center gate voltage), and a smaller dot ($1.2\,\mu\mathrm{m}^2$). Each data point represents ~ 200 independent device shapes. The large dot shows AL while the small and gated dots show WL. Estimates for λ_{so}, τ_φ and $\kappa_\perp$, from RMT fits are listed for each device below the micrographs in Figure 5.1 (see Table 5.3 for corresponding $\epsilon_\perp$ and $\epsilon_\parallel$). When AL is present (i.e., for the large dot), estimates for λ_{so} have small uncertainties ($\pm 5\%$) and give upper and lower bounds; when AL is absent (i.e., for the small and gated dots) only a lower bound for λ_{so} (-5%) can be extracted from fits. The value $\lambda_{so} \sim 4.4\,\mu\mathrm{m}$ is consistent with all dots and in good agreement with AL measurements made on an unpatterned 2DEG sample from the

[1] All measured densities are below the threshold for second subband occupation $n \sim 6.6 \times 10^{15}\,\mathrm{m}^{-2}$, which is known from Shubnikov-de Haas measurements and a decreasing mobility with increasing density near the threshold.

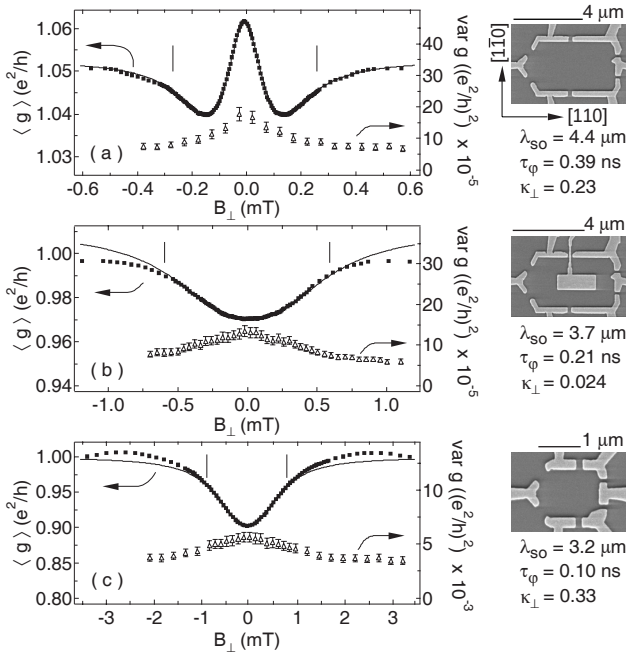

Figure 5.1: Average conductance $\langle g \rangle$ (squares) and variance of conductance $\mathrm{var}(g)$ (triangles) calculated from ~ 200 statistically independent samples (see text) as a function of perpendicular magnetic field $B_\perp$ for (a) $8.0\,\mu\mathrm{m}^2$ dot (b) $5.8\,\mu\mathrm{m}^2$ center-gated dot and (c) $1.2\,\mu\mathrm{m}^2$ dot at $T = 0.3\,\mathrm{K}$, along with fits to RMT (solid curves). In (b), the center gate is fully depleted. Vertical lines indicate the fitting range, error bars of $\langle g \rangle$ are about the size of the squares.

same wafer [105].

Comparing Figures 5.1(a) and 1(c), and recalling that all dots are fabricated on the same wafer, one sees that AL is suppressed in smaller dots, even though λ_{so} is sufficient to produce AL in the larger dot. We note that these dots do not strongly satisfy the inequalities $L/\lambda_{so} \ll 1, N \gg 1$, having $N = 2$ and $L/\lambda_{so} = 0.64\ (0.34)$ for the large (small) dot. Nevertheless, Figure5.1 shows the very good agreement between experiment and the new RMT.

5.5 Suppression of Antilocalization by an In-Plane Magnetic Field

We next consider the influence of $B_\parallel$ on $\langle g \rangle$. In order to apply tesla-scale $B_\parallel$ while maintaining subgauss control of $B_\perp$, we mount the sample with the 2DEG aligned to the axis of the primary solenoid (accurate to $\sim 1^\circ$) and use an independent split-coil magnet attached to the cryostat to provide $B_\perp$ as well as to compensate for sample misalignment [96]. Figure 5.2 shows shape-averaged magnetoconductance (relative to $B_\perp \gg \phi_0/A$, i.e., fully broken time-reversal symmetry), $\delta g(B_\perp, B_\parallel) = \langle g(B_\perp, B_\parallel) \rangle - \langle g(B_\perp \gg \phi_0/A, B_\parallel) \rangle$ as a function of $B_\perp$ at several values of $B_\parallel$, along with fits of RMT [116, 150] with parameters λ_{so}, τ_φ and $\kappa_\perp$ set by a single fit to the $B_\parallel = 0$ data. The low-field dependence of $\delta g(0, B_\parallel)$ on $B_\parallel$ [Figure 5.2(b)] allows the remaining parameter, ν_{so}, to be estimated as described below.

Besides Zeeman energy ϵ_Z (calculated using $g = -0.44$ rather than fit), parallel field combined with SO coupling introduces an additional new energy scale, $\epsilon_\perp^Z = \frac{\kappa_z \epsilon_Z^2 A}{2E_T} \sum_{i,j=1,2} \frac{l_i}{\lambda_i} \frac{l_j}{\lambda_j}$, where

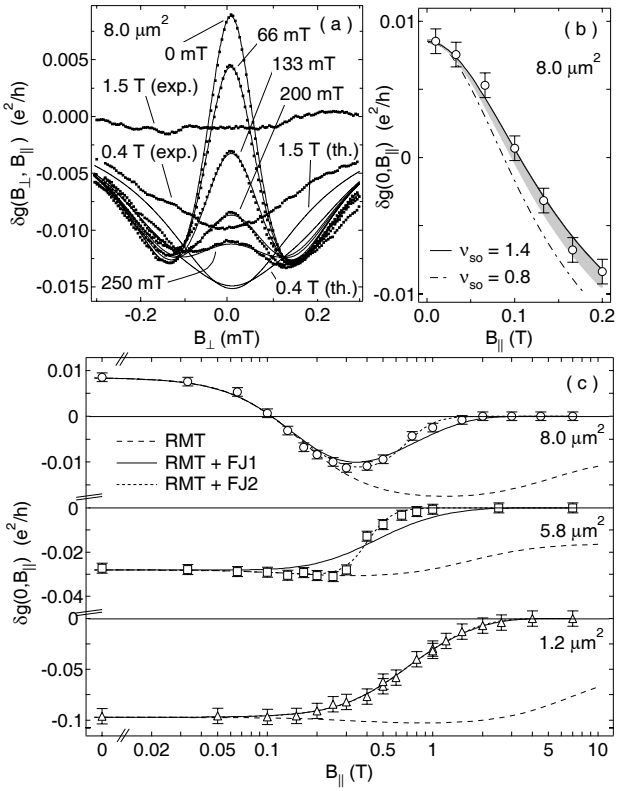

Figure 5.2: (a) Difference of average conductance from its value at large $B_\perp$, $\delta g(B_\perp, B_\parallel)$, as a function of $B_\perp$ for several $B_\parallel$ for the 8.0 $^-$m^2 dot at $T = 0.3$ K (squares) with RMT fits (curves). (b) Sensitivity of $\delta g(0, B_\parallel)$ to ν_{so} for the 8.0 $^-$m^2 dot, $1 \leq \nu_{so} \leq 2$ (shaded), $\nu_{so} = 1.4$ (solid line) and $\nu_{so} = 0.8$ (dashed line) (c) $\delta g(0, B_\parallel)$ (markers) with RMT predictions (dashed curves) and one parameter (solid curves) or two parameter fits (dotted curves) using RMT including a suppression factor due to orbital coupling of $B_\parallel$, see text.

κ_Z is a dot-dependent constant and $l_{1,2}$ are the components of a unit vector along $B_\parallel$ [116, 150]. Because orbital effects of $B_\parallel$ on $\delta g(B_\perp, B_\parallel)$ dominate at large $B_\parallel$, $\epsilon_\perp^Z$ must instead be estimated from RMT fits of var(g) with already-broken time reversal symmetry, which is unaffected by orbital coupling [**?**].

The RMT formulation [116, 150] is invariant under $\nu_{so} \to r/\nu_{so}$, where $r = L_1/L_2$ [2], and gives an extremal value of $\delta g(0, B_\parallel)$ at $\nu_{so} = \sqrt{r}$. As a consequence, fits to $\delta g(0, B_\parallel)$ cannot distinguish between ν_{so} and r/ν_{so}. As shown in Figure 5.2(b), data for the 8$^-$m^2 dot ($r \sim 2$) are consistent with $1 \leq \nu_{so} \leq 2$ and appear best fit to the extremal value, $\nu_{so} \sim 1.4$. Values of ν_{so} that differ from one indicate that both Rashba and Dresselhaus terms are significant, which is consistent with 2D data taken on the same material [105].

[2] The symmetry is precise if one takes $\epsilon_\perp^Z = \kappa_z \frac{\epsilon_Z^2}{2E_T} \frac{A}{\lambda_{so}^2}$. See Ref. [116, 150].

5.6 Breaking of Time-Reversal Symmetry due to an In-Plane Magnetic Field

Using $\nu_{so} = 1.4$ and values of λ_{so}, τ_φ, and $\kappa_\perp$ from the $B_\parallel = 0$ fit, RMT predictions for $\delta g(B_\perp, B_\parallel)$ agree well with experiment up to about $B_\parallel \sim 0.2\,\mathrm{T}$ [Figure 5.2(a)], showing a crossover from AL to WL. For higher parallel fields, however, experimental δg's are suppressed relative to RMT predictions. By $B_\parallel \sim 2\,\mathrm{T}$, WL has vanished in all dots [Figure 5.2(c)] while RMT predicts significant remaining WL at large $B_\parallel$.

One would expect WL/AL to vanish once orbital effects of $B_\parallel$ break time-reversal symmetry. Following Ref. [117, 118] (FJ), we account for this with a suppression factor $f_{FJ}(B_\parallel) = (1 + \tau_{B\parallel}^{-1}/\tau_{esc}^{-1})^{-1}$, where $\tau_{B\parallel}^{-1} \sim aB_\parallel^2 + bB_\parallel^6$, and assume that the combined effects of SO coupling and flux threading by $B_\parallel$ can be written as a product, $\delta g(0, B_\parallel) = \delta g_{RMT}(0, B_\parallel) \cdot f_{FJ}(B_\parallel)$. The $B_\parallel^2$ term reflects surface roughness or dopant inhomogeneities; the $B_\parallel^6$ term reflects the asymmetry of the quantum well. We either treat a as a single fit parameter (a_1, Table 5.3), using $b = 1.4\,10^8\,\mathrm{s^{-1}T^{-6}}$ from device simulations [3], or treat both a and b as fit parameters (a_2 and b_2, Table 5.3). Fitting both parameters only improves the fit for the (unusually shaped) center-gated dot.

5.7 Effects of Temperature on Antilocalization

Increased temperature reduces the overall magnitude of δg and also suppresses AL compared to WL, causing AL at 300 mK to become WL by 1.5 K in the $8^-\mathrm{m}^2$ dot [Figure 5.3(a)]. Fits of RMT to $\delta g(B_\perp, 0)$ yield λ_{so} values that are roughly independent of temperature [Figure 5.3(b)], consistent with 2D results [151], and τ_φ values that decrease with increasing temperature. Dephasing is well described by the empirical form $(\tau_\varphi[\mathrm{ns}])^{-1} \sim 7.5\,\mathrm{T[K]} + 2.5\,(\mathrm{T[K]})^2$, consistent with previous measurements in low-SO dots [166, 167]. As dephasing increases, long trajectories that allow large amounts of spin rotations are cut off, diminishing the AL feature.

5.8 *In Situ* Control of Spin-Orbit Coupling with a Center Gate

Finally, we demonstrate *in situ* control of the SO coupling using a center-gated dot. Figure 5.4 shows the observed crossover from AL to WL as the gate voltage V_g is tuned from $+0.2\,\mathrm{V}$ to $-1\,\mathrm{V}$. At $V_g = -1\,\mathrm{V}$, the region beneath the center gate is fully depleted, giving a dot with area $5.8^-\mathrm{m}^2$ that shows WL. In the range of $V_g \geq -0.3$ V, the amount of AL is controlled by modifying the density under the gate. For $V_g > 0\,\mathrm{V}$ the AL peak is larger than in the ungated $8^-\mathrm{m}^2$ dot. We interpret this enhancement not as a removal of the SO suppression due to an inhomogeneous SO coupling [168], which would enhance AL in dots with $L/\lambda_{so} \ll 1$ (not the case for the $8^-\mathrm{m}^2$ dot), but rather as the result of increased SO coupling in the higher-density region under the gate when $V_g > 0\,\mathrm{V}$.

One may wish to use the evolution of WL/AL as a function of V_g to extract SO parameters for the region under the gate. To do so, the dependence may be ascribed to either a gate-dependent λ_{so} or to a gate-dependence of a new parameter $\kappa_\parallel = \epsilon_\parallel^{so}/(((L_1/\lambda_1)^2 + (L_2/\lambda_2)^2)\epsilon_\perp^{so})$. Both options give equally good agreement with the data (fits in Figure 5.4 assume $\lambda_{so}(V_g)$), including the parallel field dependence (not shown). Resulting values for λ_{so} or $\kappa_\parallel$ (assuming the other fixed)

[3] V. Falko, T. Jungwirth, private communication.

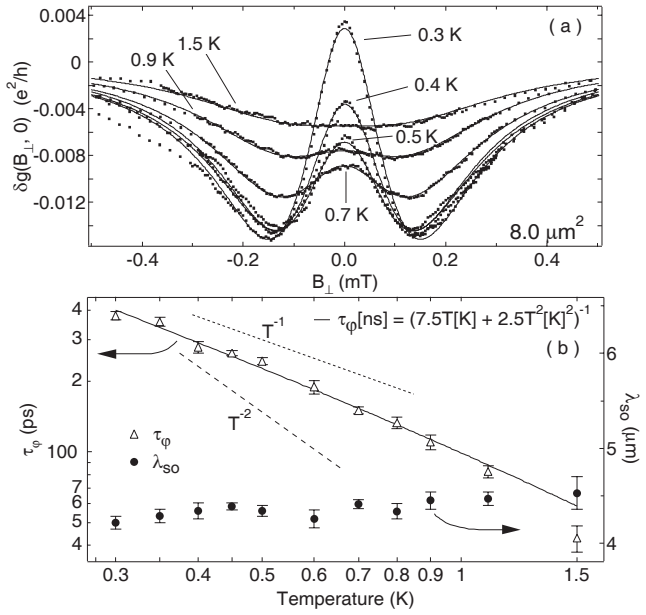

Figure 5.3: (a) Difference of average conductance from its value at large $B_\perp$, $\delta g(B_\perp, 0)$, for various temperatures with $B_\parallel = 0$ for the 8.0 $^-$m^2 dot (squares), along with RMT fits (solid curves). (b) Spin-orbit lengths λ_{so} (circles) and phase coherence times τ_φ (triangles) as a function of temperature, from data in (a).

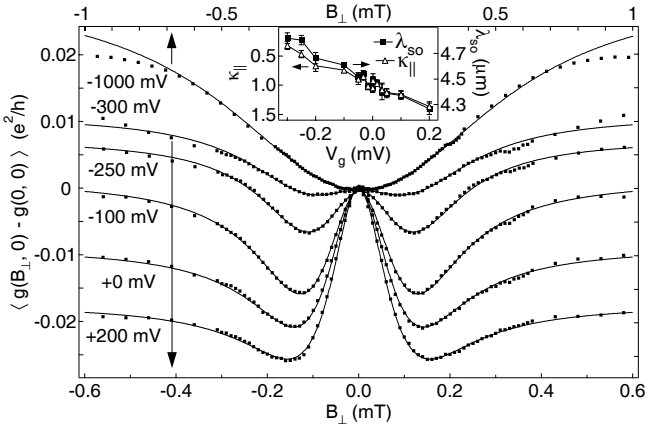

Figure 5.4: Difference of average conductance $\langle g \rangle$ from its value at $B_\perp = 0$ as a function of $B_\perp$ for various center gate voltages V_g in the center-gated dot (squares), along with fits to RMT [116, 150]. Good fits are obtained though the theory assumes homogeneous SO coupling. Error bars are the size of the squares. Inset: λ_{so} and $\kappa_\parallel$ as a function of V_g extracted from RMT fits, see text.

are shown in the inset in Figure5.4. We note that the 2D samples from the same wafer did not show gate-voltage dependent SO parameters [105]. However, in the 2D case a cubic Dresselhaus term that is not included in the RMT of Ref. [116, 150] was significant. For this reason, fits using [116, 150] might show $\lambda_{so}(V_g)$ though the 2D case did not. Further investigation of the gate dependence of SO coupling in dots will be the subject of future work.

5.9 Acknowledgements

We thank I. Aleiner, B. Altshuler, P. Brouwer, J. Cremers, V. Falko, J. Folk, B. Halperin, T. Jungwirth and Y. Lyanda-Geller. This work was supported in part by DARPA-QuIST, DARPA-SpinS, ARO-MURI and NSF-NSEC. Work at UCSB was supported by QUEST, an NSF Science and Technology Center. JBM acknowledges partial support from NDSEG.

Chapter 6
Conductance Fluctuations in Open Quantum Dots with Spin-Orbit Coupling and Zeeman Fields

D. M. Zumbühl, J. B. Miller*, C. M. Marcus
Department of Physics, Harvard University, Cambridge, Massachusetts 02138
**Division of Engineering and Applied Science*
Harvard University, Cambridge, Massachusetts 02138

D. Goldhaber-Gordon
Department of Physics, Harvard University, Cambridge, Massachusetts 02138
Department of Physics, Stanford University
Stanford, California 94305

J. S. Harris, Jr.
Departement of Electrical Engineering
Stanford University, Stanford, California 94305

K. Campman, A. C. Gossard
Materials Department, University of California at Santa Barbara
Santa Barbara, California, 93106

Conductance fluctuations in GaAs quantum dots with spin-orbit and Zeeman coupling are investigated experimentally and compared to a random matrix theory formulation that defines a number of regimes of spin symmetry depending on experimental parameters. Accounting for orbital coupling of the in-plane magnetic field, which can break time-reversal symmetry, yields excellent overall agreement between experiment and theory.

[This chapter is published in Phys. Rev. B **72**, 081305 (2005)]

6.1 Introduction

The combination of quantum confinement, spin-orbit (SO) coupling and Zeeman effects in lateral semiconductor quantum dots gives rise to rich physics, including novel spin-rotation symmetries [116, 150], a suppression of SO effects due to confinement [96, 113, 115, 116, 148–150] leading to very long spin life times [148, 149, 169–171] and lifting of the SO suppression by an in-plane field [96, 115, 116, 150] as well as by a spatial dependence of the SO parameters [168]. Further, magnetic fields $B_\parallel$ applied in the plane of the 2D electron gas (2DEG) change the electron dispersion and in particular can break time reversal symmetry (TRS) [113, 117, 118, 172], adding additional complexity to this system.

In this communication, we present an experimental study of the variance of conductance fluctuations $\mathrm{var}\, g$ through open quantum dots defined by lateral gates on a GaAs/AlGaAs 2DEG. The $B_\parallel$ dependence of the variance $\mathrm{var}\, g(B_\perp \neq 0, B_\parallel)$ with TRS broken by a perpendicular field $B_\perp \neq 0$ is seen to depend strongly on the SO strength and can be characterized by novel spin-rotation symmetries found in Ref. [116, 150], which gives good fits to our data. Further, $\mathrm{var}\, g(B_\perp, B_\parallel)$ is seen to become independent of $B_\perp$ at large $B_\parallel$ due to effects of $B_\parallel$ breaking TRS. This is in good agreement with theory [117, 118] as well as experiments on average [113] and correlations [172] of conductance fluctuations.

6.2 Previous Work

Theory of low-dimensional, diffusive systems has long predicted conductance fluctuations [173, 174] to be reduced by both SO coupling [127, 175] as well as Zeeman effects [176–178]. Random matrix theories [94, 95, 176, 179] offer a universal classification of statistical properties such as the average and variance of conductance in terms of the fundamental symmetry classes. These theories were widely confirmed by experiments in diffusive 2D and 1D systems in both metals and GaAs 2DEG's, including observed reductions in variance due to Zeeman splitting [180, 181], SO coupling [151, 182] and breaking of TRS both in the presence [183] and absence of SO coupling [184].

In open quantum dots, an observed large reduction of conductance fluctuations in $B_\parallel$ [96, 161, 185, 186] has been explained by SO effects that increase upon application of $B_\parallel$ while SO effects at $B_\parallel = 0$ are confinement suppressed [115]. This has led to an extended random matrix theory (RMT) [116, 150], including a classification of transport properties in terms of spin-rotation symmetries. Subsequent experiments found AL [113, 187] in high density dots due to strong SO coupling at $B_\parallel = 0$, allowing the SO length λ_{so} to be extracted. Orbital effects of $B_\parallel$ were observed via a suppression of weak (anti)localization [113] as well as in correlations of conductance fluctuations [172]. In this study, we report on effects of $B_\parallel$ on the variance in dots of various SO strength.

6.3 Spin-Rotation Symmetry Classes

The RMT [116, 150] gives the variance (at zero temperature $T = 0$) in terms of symmetry parameters: $\mathrm{var}\, g \propto s/(\beta\Sigma)$ [116, 150], where β is the conventional parameter describing time-reversal symmetry, s is the Kramers degeneracy parameter and Σ characterizes mixing of different spins when Kramers degeneracy is already broken. Spin rotation symmetry is classified as either not broken ($s = 2, \Sigma = 1$), partially broken ($s = 1, \Sigma = 1$) or completely broken ($s = 1, \Sigma = 2$). The

variance is reduced by a factor of two when a crossover into the class with next-lower symmetry occurs. The Kramers degeneracy can be lifted by a Zeeman field as well as SO coupling if $B_\perp \neq 0$. Once Kramers degeneracy is broken ($s = 1$), mixing of spins ($\Sigma = 2$) is due to SO coupling and can be possible already at $B_\parallel = 0$ due to SO coupling or can be revived by $B_\parallel$ when SO coupling is confinement suppressed [115] at $B_\parallel = 0$. Finite temperatures and decoherence strongly reduce var (g) [116, 150], but the relative reduction factor $R = \mathrm{var}\, g(B_\perp \neq 0, B_\parallel = 0)/\mathrm{var}\, g(B_\perp \neq 0, B_\parallel \gg 0)$ is affected only weakly.

6.4 Experimental Techniques

Four quantum dots of various sizes were measured, made on two different 2DEG's with electron densities $n = 2 \times 10^{11} cm^{-2}$ and $n = 5.8 \times 10^{11} cm^{-2}$, see Ref. [113, 172] for details. Figures 1 and 2 show device micrographs (insets). Measurements were made in a ^{3}He cryostat at 0.3 K using current bias of 1 nA at 338 Hz. In order to apply tesla-scale $B_\parallel$ while maintaining sub-gauss control of $B_\perp$, we mount the sample with the 2DEG aligned to the axis of the primary solenoid (accurate to $\sim 1^\circ$) and use an independent split-coil magnet attached to the cryostat to provide $B_\perp$ [96]. The Hall effect measured in a GaAs Hall bar as well as the location of weak (anti)localization extrema in transport through the dot itself (visible $B_\parallel \lesssim 2T$) were used to determine $B_\perp = 0$.

Statistics of conductance fluctuations were gathered using two shape-distorting gates [165] while the point contacts were actively held at one fully transmitting mode each ($N = 2$). Based on about ~ 400 (~ 200) statistically independent samples for the low density (high density) dots, the average and variance of conductance were obtained. Measurements were taken at various fixed $B_\parallel$ as a function of $B_\perp$, with high resolution around $B_\perp = 0$, increasing the number of statistically independent samples for $B_\perp \neq 0$ by about a factor of 5.

6.5 Characterization of Spin-Orbit Strength at Zero In-Plane Field

The average conductance $\langle g(B_\perp)\rangle$ is used to characterize the strength of SO coupling. The large dot on high density material shows AL due to SO coupling [Fig. 6.1(a)], while the smaller dot on the same material displays WL [Fig. 6.1(b)], showing that SO effects in the small dot are suppressed due to the extra confinement, as previously reported [113]. Fits of $\langle g(B_\perp)\rangle$ to the RMT [116, 150] give the average SO length $\lambda_{so} = \sqrt{|\lambda_1\lambda_2|}$, where $\lambda_{1,2}$ are the SO lengths along the main crystal axes, the phase coherence time τ_φ and $\kappa_\perp$, a parameter related to typical trajectory area. The SO inhomogeneity $\nu_{so} = \sqrt{|\lambda_1/\lambda_2|}$ can be extracted from $\langle g(B_\parallel)\rangle$ in the presence of AL, and is taken as $\nu_{so} = 1.4(1.0)$ for the high(low) density devices. An additional parameter κ' of order one in the RMT—relevant in the strong SO limit—is taken as $\kappa' = 1$ for all devices. For fit details see Ref. [113], parameters are listed in Table I. In absence of AL, only a lower bound on λ_{so} can be found. The extracted coherence times are comparable for all devices and consistent with previous experiments [167]. Note that the SO length λ_{so} is comparable to the device diameter $L = \sqrt{A}$ of the big dot.

On the low density material, both devices show WL, see Figure 6.2, indicating that for both dots $\lambda_{so} \gg L$, the regime of confinement suppressed SO coupling. Note that while both 8 μm^2 dots have nominally identical geometries, only the device on the high density 2DEG shows AL. Constrained by experiments observing WL (rather than AL) in identical devices made on this wafer [167] down to the lowest dilution-refrigerator temperatures, a lower bound $\lambda_{so} \gtrsim 8.5\,\mu$m

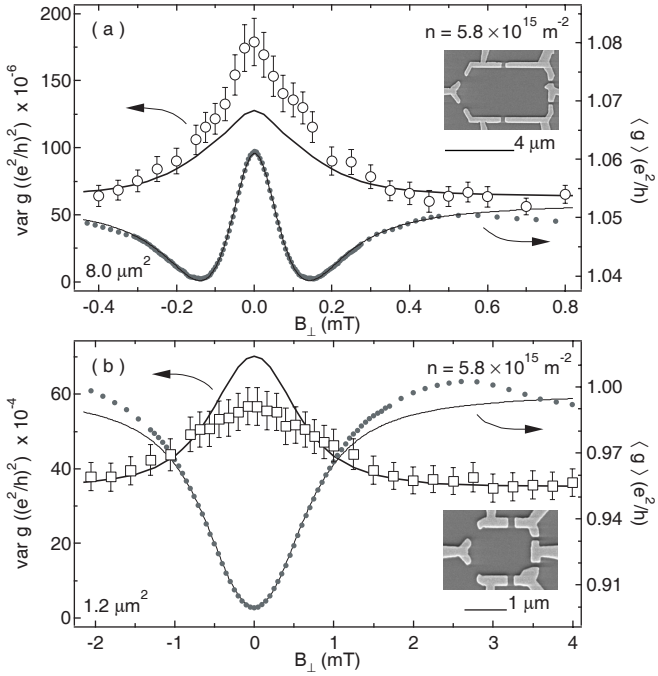

Figure 6.1: Average $\langle g(B_\perp)\rangle$ (solid dots) and variance $\mathrm{var}\, g(B_\perp)$ (open symbols) of conductance as a function of magnetic field $B_\perp$ perpendicular to the 2DEG at a temperature $T = 300\,\mathrm{mK}$ and zero magnetic field $B_\parallel = 0$ in the plane of the 2DEG, measured in the devices on high density 2DEG. Insets show device micrographs. AL due to SO coupling is seen in the big $8\,\mu\mathrm{m}^2$ dot (a). WL is seen in the smaller $1.2\,\mu\mathrm{m}^2$ dot (b) fabricated on the same material, demonstrating confinement suppression of SO effects. Both dots show a larger variance at $B_\perp = 0$ when TRS is not broken. Fits of the RMT [116, 150] to $\langle g(B_\perp)\rangle$ are shown as dashed curves. Solid curves are the RMT for $\mathrm{var}\, g(B_\perp)$ with the same parameters as obtained from fits to $\langle g\rangle$ times an overall correction factor (see text).

n	A	τ_φ	λ_{so}	ν_{so}	$\kappa_\perp$	f_{var}	ξ	a	b
m^{-2}	$\mu\mathrm{m}^2$	ns	μm					$\mathrm{ns}^{-1}\mathrm{T}^{-2}$	$\mathrm{ns}^{-1}\mathrm{T}^{-6}$
2.0	3.0	0.18	8.5	1.0	0.15	1.0	2.8	0.5±0.1	0.028
2.0	8.0	0.21	8.5	1.0	0.25	0.6	3.0	0.37±0.07	0.028
5.8	1.2	0.10	3.2	1.4	0.33	1.9	1.0	6.6±1	0.14
5.8	8.0	0.39	4.4	1.4	0.23	0.7	0.45	1.4±0.4	0.14

Table 6.1: Carrier density n, dot area $A = L^2$, coherence time τ_φ, spin-orbit parameters λ_{so} and ν_{so}, RMT parameters $\kappa_\perp$, f_{var} and ξ and FJ parameters a and b, see text.

is estimated. It is noted that a $\lambda_{so} = 8.5\,\mu\mathrm{m}$ noticeably reduces the WL correction amplitude at the lowest temperatures $T = 50\,\mathrm{mK}$. The resulting low-temperature saturation of coherence times extracted using theory neglecting SO effects is consistent with the large dot results of Ref. [167].

6.6 Variance at Zero In-Plane Field

The variance of conductance fluctuations $\mathrm{var}\, g(B_\perp)$ at $B_\parallel = 0$ is seen to be reduced upon application of a small perpendicular field $B_\perp$ [Figures 6.1 and 6.2]. This is due to breaking of TRS by $B_\perp$ and is well known [165, 188]. Using the parameters obtained from fits to $\langle g(B_\perp)\rangle$ and an additional overall factor f_{var} (Table I) to match the RMT variance at $B_\perp \neq 0$ with the experi-

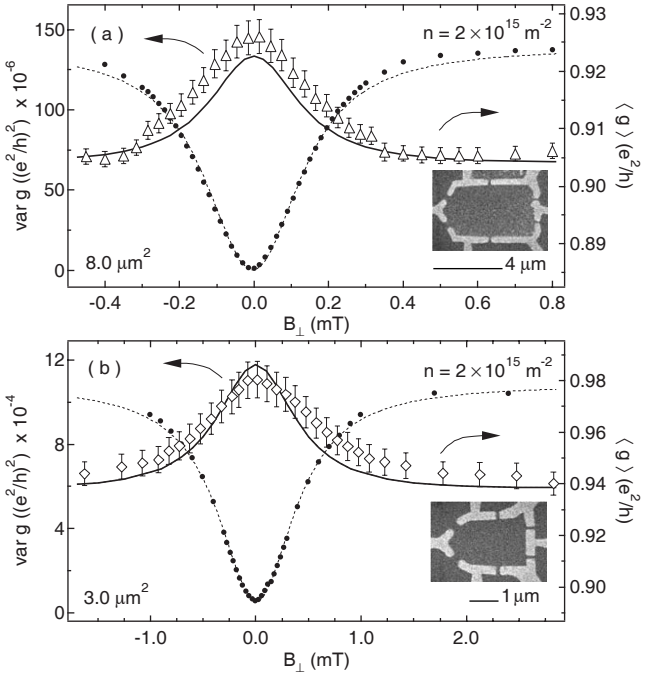

Figure 6.2: Average $\langle g(B_\perp)\rangle$ (solid dots) and variance $\mathrm{var}\, g(B_\perp)$ (open symbols) at a temperature $T = 300\,\mathrm{mK}$ and $B_\parallel = 0$, measured in the devices on low density 2DEG. Both devices display WL, indicating that SO effects are weak. Note that while both $8\,\mu\mathrm{m}^2$ dots have nominally identical geometry, only the high density device shows AL. RMT is shown as dashed and solid curves, as described in the caption of Figure 1.

ment, the solid RMT curves in Figures 6.1 and 6.2 are obtained from Eq. (37) of Ref. [116, 150], which includes effects of thermal smearing and decoherence. The RMT—applicable for $N \gg 1$ in chaotic dots—calculates a ratio $\mathrm{var}\, g(B_\perp = 0, B_\parallel)/\mathrm{var}\, g(B_\perp \neq 0, B_\parallel)$ of two, independent of $B_\parallel$ (see below). Theories valid for $N = 2$ are not currently including SO effects [189].

6.7 Effects of Spin-Rotation Symmetry on the Variance

The variance in an in-plane field $B_\parallel$ when TRS is broken by $B_\perp \neq 0$ depends strongly on the SO properties. The open symbols in the main panels of Figures 6.3 and 6.4 show that the variance is reduced upon application of $B_\parallel$ and saturates at large $B_\parallel$, giving reduction factors $R = \mathrm{var}\, g(B_\perp \neq 0, B_\parallel = 0)/\mathrm{var}\, g(B_\perp \neq 0, B_\parallel \gg 0)$ between $R \sim 1.6$ for the dot showing pronounced SO effects at $B_\parallel = 0$ and $R \sim 4$ for the low density dots showing WL at $B_\parallel = 0$. Reduction factors as small as $R \sim 1.3$ are seen in center gated devices with stronger SO coupling (not shown). Within the RMT these new experimental results are explained in terms of spin-rotation symmetries: in dots showing AL, SO coupling breaks Kramers degeneracy $s = 1$ and mixes up and down spins to some extent at already $B_\parallel = 0$ if $B_\perp \neq 0$, resulting in small reduction factors $1 \leq R \leq 2$. In dots showing WL, on the other hand, spin-rotation symmetry is intact at $B_\parallel = 0$ ($s = 2, \Sigma = 1$) but can be broken upon application of $B_\parallel$, resulting in reduction factors $R \sim 4$ (low density dots).

Breaking of spin rotation symmetry—besides the Zeeman effect $\epsilon_Z = g\mu_B B$ ($|g| = 0.44$) which breaks Kramers degeneracy—is caused by SO coupling combined with $B_\parallel$, introducing a new energy scale [115, 116, 150] $\epsilon_\perp^Z = \xi^2 \epsilon_Z^2/(2E_T)(A/\lambda_{so}^2)$. A is the device area, ξ is a geometry

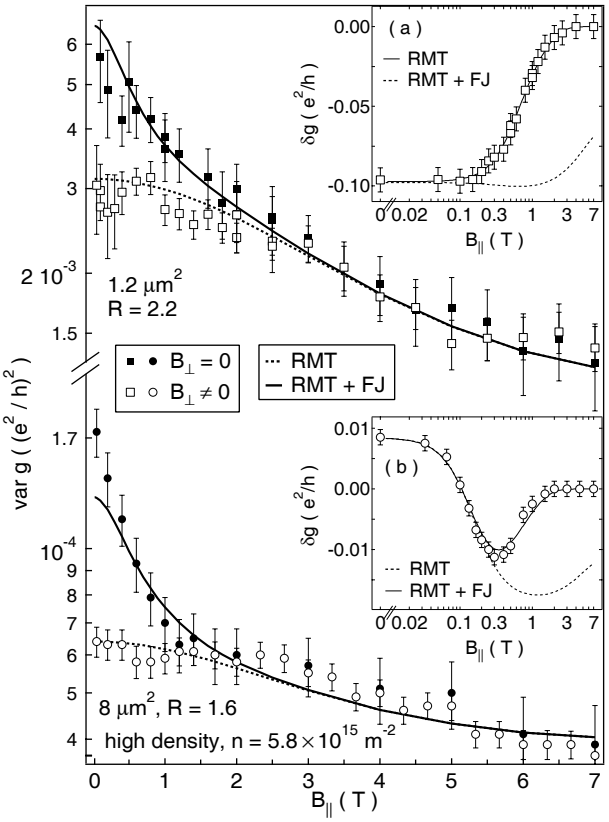

Figure 6.3: Variance of conductance fluctuations through high density devices as a function of in-plane field $B_\parallel$ with $B_\perp = 0$ (solid symbols) and $B_\perp \neq 0$ (open symbols) sufficiently large to break TRS. It is seen that the big dot with strong SO effects at $B_\parallel = 0$ shows a smaller reduction of the variance in $B_\parallel$ than the small dot. Insets show $\delta g(B_\parallel) = \langle g(B_\perp = 0, B_\parallel)\rangle - \langle g(B_\perp \neq 0, B_\parallel)\rangle$ (open symbols). Dashed curves show RMT, the solid curves are RMT+FJ, see text.

and $B_\parallel$ direction-dependent coefficient and E_T is the conventional Thouless energy. The associated field scale, given by $\epsilon_\perp^Z \gtrsim \tilde{\gamma}$, where $\tilde{\gamma}$ is the level broadening due to escape and decoherence [113], becomes large in small dots and in the weak SO limit and is inaccessible in the smallest dot, giving $R \sim 2$ due to breaking of Kramers degeneracy only. In the bigger, low density dots, where this field scale is one to two Tesla, the SO strength λ_{so} cannot be independently extracted from a $\mathrm{var}\, g(B_\parallel)$ measurement because of the extra coefficient ξ. Using ξ as the only fit parameter, the dashed RMT curves in Figures 6.3 and 6.4 are obtained, giving good agreement for all devices.

6.8 Orbital effects of $B_\parallel$ on the Variance

Finally, we turn to orbital effects of $B_\parallel$ on the variance measured when TRS is not externally broken ($B_\perp = 0$). As $B_\parallel$ is increased from zero, $\mathrm{var}\, g(B_\perp = 0, B_\parallel)$ is seen to decrease sharply, approaching $\mathrm{var}\, g(B_\perp \neq 0, B_\parallel)$. At large $B_\parallel$, the measured variance becomes independent of $B_\perp$ within the errorbars (solid symbols, Figures 6.3 and 6.4) while the RMT predicts that the variance with $B_\perp = 0$ is twice the value at $B_\perp \neq 0$, independent of $B_\parallel$. On a comparable $B_\parallel$ field scale, quantum corrections to the average conductance, $\delta g(B_\parallel) = \langle g(B_\perp = 0, B_\parallel)\rangle - \langle g(B_\perp \neq 0, B_\parallel)\rangle$, are seen to be vanishing upon application of $B_\parallel$ in all devices (open symbols, insets), whereas the RMT calculates a reduced but finite δg (dashed curves, insets). Suppression of δg in $B_\parallel$ was

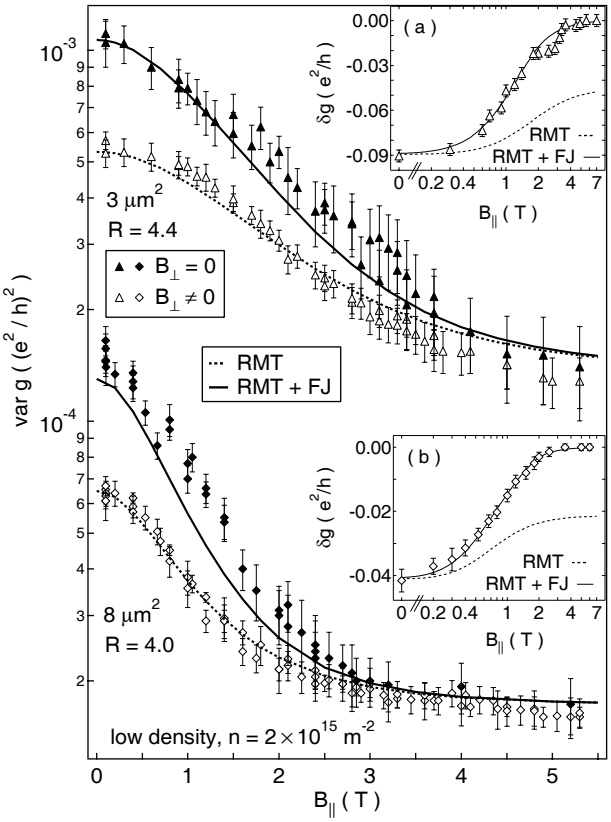

Figure 6.4: As Figure 3 but for low density devices. Due to effects of $B_\parallel$ to break TRS, the variance for $B_\perp = 0$ is seen to be reduced to the variance for $B_\perp \neq 0$ on the same $B_\parallel$ field scale where WL/AL effects are suppressed by $B_\parallel$ (insets).

previously reported [96, 113] and is due to effects of $B_\parallel$ to break TRS [117, 118].

Following Ref. [117] (FJ), the suppressions of average and variance can be accounted for by a factor $f_{FJ}(B_\parallel) = (1 + \tau_{B_\parallel}^{-1}/\tau_{esc}^{-1})^{-1}$, where $\tau_{B_\parallel}^{-1} \sim aB_\parallel^2 + bB_\parallel^6$ and $\tau_{esc}^{-1} = N\Delta/h$ is the escape time. The $B_\parallel^2$ term reflects interface roughness and dopant inhomogeneities; the $B_\parallel^6$ term is due to the asymmetry of the well. It is assumed that the combined effects of the RMT and flux threading by $B_\parallel$ can be written as products $\delta g(B_\parallel) = \delta g_{RMT}(B_\parallel) f_{FJ}(B_\parallel)$ and $\mathrm{var}\, g(B_\perp = 0, B_\parallel) = \mathrm{var}\, g_{RMT}(B_\perp \neq 0, B_\parallel)(1 + f_{FJ}(B_\parallel))$ [1]. The coefficient a is obtained from a fit to the experimental $\delta g(B_\parallel)$ while b is estimated from device simulations[2] (Table I). The resulting theory curves for both $\delta g(B_\parallel)$ (solid curves, insets) and $\mathrm{var}\, g(B_\perp = 0, B_\parallel)$ (solid curves, main panels) are in good agreement with the experiment. We emphasize that the theoretical variance curves are not fit. The coefficients a, b estimated from correlation functions [172] are consistent with the values obtained here from $\delta g(B_\parallel)$.

6.9 Conclusion

In summary, the variance of conductance fluctuations in open quantum dots in presence of SO coupling and in plane fields $B_\parallel$ is understood in terms of symmetries in the system, including

[1] V. Fal'ko and T. Jungwirth, private communication

[2] V. Fal'ko and T. Jungwirth, private communication

novel spin rotation symmetries as well as time reversal symmetry, which can be broken both by perpendicular fields $B_\perp$ and parallel fields $B_\parallel$.

6.10 Acknowledgements

We thank I. Aleiner, B. Al'tshuler, P. Brouwer, J. Cremers, V. Fal'ko, J. Folk, B. Halperin, T. Jungwirth and Y. Lyanda-Geller. This work was supported in part by DARPA-QuIST, DARPA-SpinS, ARO-MURI and NSF-NSEC. We also acknowledge support from NDSEG (J. B. M.) and the Harvard Society of Fellows (D.G.-G). Work at UCSB was supported by QUEST, an NSF Science and Technology Center.

Chapter 7
Experimental observation of the $\nu = 5/2$ state in a quantum point contact

J. B. Miller*, I. Radu†, D. M. Zumbühl†§, E. Levenson-Falk‡,
M. A. Kastner†, C. M. Marcus‡
L. N. Pfeiffer¶, K. W. West¶

*Division of Engineering and Applied Science, Harvard University, Cambridge, Massachusetts 02138

†Department of Physics, Massachusetts Institute of Technology, Cambridge, Massachusetts 02139

§Institut für Physik, Universität Basel, Klingelbergstr. 82, CH-4056 Basel, Switzerland

‡Department of Physics, Harvard University, Cambridge, Massachusetts 02138

¶Bell Labs, Lucent Technologies, Murray Hill, New Jersey 07974

We study the transport properties of quantum point contacts (QPCs) fabricated on a GaAs/AlGaAs two dimensional electron gas that exhibits well-developed fractional quantum Hall effect, including at bulk filling fraction $\nu_{\mathrm{bulk}} = 5/2$. We find that a plateau at effective filling factor $\nu_{\mathrm{QPC}} = 5/2$ is identifiable in point contacts with lithographic widths of 1.2 μm and 0.8 μm, but not 0.5 μm. We study the temperature and dc-current-bias dependence of the $\nu_{\mathrm{QPC}} = 5/2$ plateau as well as neighboring fractional and integer plateaus in the QPC while keeping the bulk at $\nu_{\mathrm{bulk}} = 3$. Transport near $\nu_{\mathrm{QPC}} = 5/2$ in the QPCs is consistent with a picture of chiral Luttinger liquid edge-states with inter-edge tunneling, suggesting that an incompressible state at $\nu_{\mathrm{QPC}} = 5/2$ forms in this confined geometry.

[This chapter is similar to an article to appear in *Nature Physics*, August 2007.]

7.1 Introduction

The discovery [45] of a fractional quantum Hall effect (FQHE) at the even-denominator filling fraction $\nu = 5/2$ has sparked a series of experimental [60–62, 190–193] and theoretical [51, 194, 195] studies, leading to a prevailing interpretation of the $5/2$ state as comprised of paired composite fermions condensed into a BCS-like state [46, 48**?** –50]. Within this picture, excitations of the $5/2$ ground state possess nonabelian statistics [55, 56, 196] and associated topological properties. The possibility that such a topological state can be accessed in the laboratory has prompted recent theoretical work aimed at experimentally testing the nonabelian character of the $5/2$ state [3–6, 197], and building topologically protected quantum gates controlled by manipulating the excitations of the $5/2$ state [2, 198, 199].

While proposed tests of the statistics of excitations of the $5/2$ state make use of confined ($\sim$ few micron) geometries, previous studies of the $5/2$ state have been conducted in macroscopic (100 µm - 5 mm) samples. Although experiments using mesoscopic samples with a quantum point contact (QPC) are now routine, the $5/2$ state is exceptionally fragile; only the highest quality GaAs/AlGaAs heterostructures exhibit a $5/2$ state even in bulk samples. Experimental investigation of the statistics of the $5/2$ ground state is crucial, especially since alternative models have been proposed to explain the $5/2$ state in confined geometries [200] and in the bulk [49, 52].

In this paper we study the $5/2$ state in the vicinity of a quantum point contact. Near a QPC, the electron density is not uniform, so the notion of a QPC-filling fraction is not well defined. However, based on transport measurements, it is possible to define an effective filling fraction in the vicinity of the QPC (ν_{QPC}), as discussed below. Below 30 mK, a plateau-like feature with diagonal resistance (also defined below) near, but above, the bulk quantized value of $0.4\,h/e^2$ is evident at $\nu_{\mathrm{QPC}} = 5/2$ in QPCs with 1.2 µm and 0.8 µm spacings between the gates. On this plateau, we find a peak in the differential resistance at dc-current bias $I_{\mathrm{dc}} = 0$ and a dip around $I_{\mathrm{dc}} \sim 1.2$ nA, a characteristic shape that is consistent with QPC-induced quasiparticle tunneling between fractional edge states [68]. We also observe a zero-bias peak at $\nu_{\mathrm{QPC}} = 2\,1/3$, whereas we find a zero-bias dip near $\nu_{\mathrm{QPC}} = 2\,2/3$ [201], consistent with previous QPC studies for $\nu_{\mathrm{QPC}} < 1$ [70].

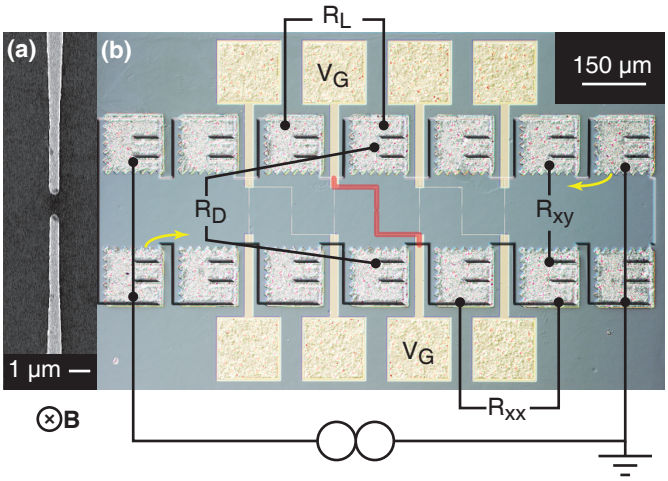

Figure 7.1: (a) SEM micrograph of the 0.5 µm QPC. (b) Optical micrograph of the entire device (the outline of the wet-etched Hall bar has been enhanced for clarity). The measurement circuit for the red-highlighted QPC is drawn schematically, with the direction of the edge-current flow indicated by the yellow arrows.

As the temperature increases from 30 mK to 70 mK, the plateaus in the QPC disappear. Fractional plateaus are not observed in a 0.5 µm QPC, and the I_{dc} characteristic is flat for all magnetic fields. Together, these observations suggest that the 5/2 state is destroyed in the 0.5 µm QPC, but can survive and exhibit quasiparticle tunneling [66, 69, 70, 202–204] in the larger QPCs.

7.2 Measurement Techniques

We measure R_{xy}, R_{xx}, R_D and R_L (Fig. 7.1) as four-wire differential resistances ($R = dV/dI_{ac}$) [205]. In the IQHE regime, these resistances can be readily interpreted in terms of edge channels [206, 207], where N_{bulk} is the number of edge channels in the bulk and N_{QPC} ($\leq N_{bulk}$) is the number traversing the QPC. The bulk Hall resistance, $R_{xy} \sim h/e^2(1/N_{bulk})$ [208], probes the number of edge states in the bulk region. The bulk longitudinal resistance, R_{xx}, vanishes when R_{xy} shows a plateau. The diagonal resistance across a QPC, $R_D \sim h/e^2(1/N_{QPC})$, is sensitive only to the number of edge channels traversing the QPC, and hence provides a QPC-analog to the bulk R_{xy}. The longitudinal resistance across the QPC, $R_L \sim R_D - R_{xy}$, contains information about both the bulk and the QPC-region, and is not directly analogous to the bulk R_{xx}. On bulk IQHE plateaus, the filling fraction is equivalent to the number of edge states, $\nu_{bulk} = N_{bulk}$. By analogy, in the QPC, where the filling fraction is not well defined due to nonuniform density, we define an effective filling fraction in the QPC: $\nu_{QPC} \sim h/e^2(1/R_D)$.

The edge state interpretation for R_{xy}, R_{xx}, R_D, and R_L has been extended to the FQHE [29, 64, 207, 209–214]. Within this generalized picture, a quantized plateau in $R_{xy} \sim h/e^2(1/\nu_{bulk})$ corresponds to the quantum Hall state at filling fraction ν_{bulk}, and a plateau in $R_D \sim h/e^2(1/\nu_{QPC})$ indicates that an incompressible quantum Hall state has formed in the vicinity of the QPC with effective filling fraction ν_{QPC}. We associate deviations from precisely quantized values with tunneling, which we study below as a function of temperature and bias.

To simplify the study of quantum states in the vicinity of the QPC, the perpendicular magnetic field (B) and gate voltage of the QPC (V_g) are tuned such that ν_{bulk} is fixed at an integer quantum Hall effect (IQHE) plateau whenever ν_{QPC} is at a value of interest. With $R_{xx} \sim 0$ and R_{xy} quantized to an IQHE plateau, features in R_D and R_L measurements can be attributed to the QPC region and not the bulk.

7.3 Previous Experiments

Previously, QPCs have been used to selectively transmit integer [215, 216] and fractional edge channels [64, 217], and to study inter-edge tunneling between fractional edge channels [69, 203], including in the regime where the bulk is intentionally set to an IQHE plateau [70, 204]. Comparisons with these results are discussed below. QPCs have also been employed in studies of noise [218] and (along with etched trenches) interference of quasiparticles [219] in the FQHE regime. In all of these studies $\nu < 2$, where the FQHE gaps are typically much larger [220, 221] than those with $\nu > 2$.

7.4 Experimental Details

The sample is a GaAs/AlGaAs heterostructure grown in the [001] direction with electron gas layer 200 nm below the surface, with Si δ-doping layers 100 nm and 300 nm below the surface. A

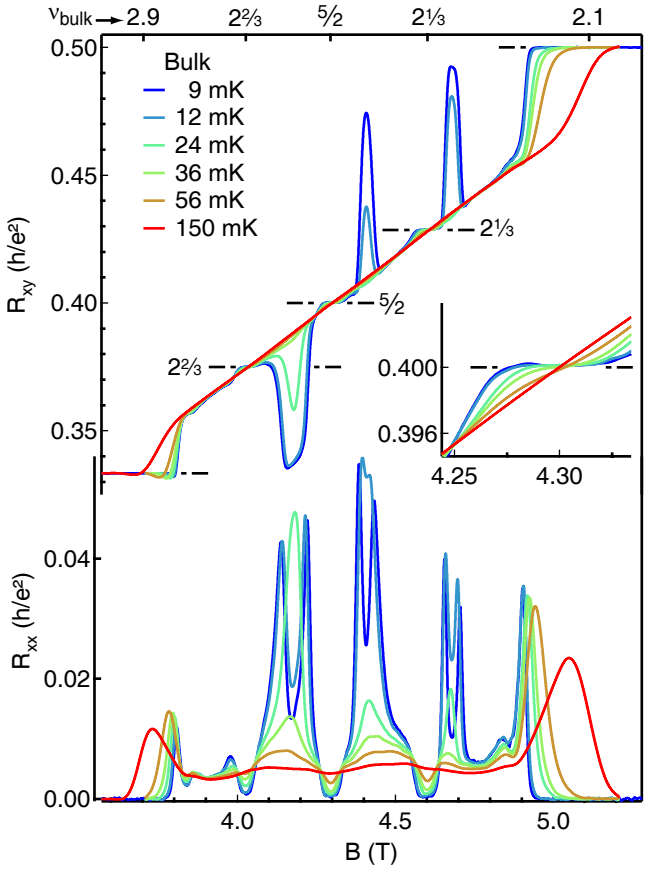

Figure 7.2: Bulk transport measurements, including temperature dependence. The inset is an enlargement of the R_{xy} data near $\nu_{bulk} = 5/2$.

150 µm-wide Hall bar is patterned using photolithography and a H_2O:H_2SO_4:H_2O_2 (240:8:1) wet-etch, followed by thermally evaporated Cr/Au (5 nm/15 nm) top-gates patterned using electron-beam lithography (see Fig. 7.1). The gates form QPCs with lithographic separation between gates of 0.5, 0.8 and 1.2 µm [222]. Depleting the electron gas beneath only one side of a QPC has no effect on transport measurements. Measurements are performed in a dilution refrigerator with base temperature 6 mK using standard four-wire lock-in techniques, with an ac current-bias excitation (I_{ac}) ranging from 0.2 nA to 0.86 nA, and a dc current-bias ranging from 0 to 20 nA. The differential resistances (dV/dI_{ac}) are measured in four places, as shown in Fig. 7.1. All quoted temperatures are measured using a RuO_2 resistor mounted on the mixing chamber. The bulk mobility of the device measured at base temperature is 2000 m^2/Vs and the electron density is $2.6\times10^{15}\,m^{-2}$.

7.5 Bulk Measurements

Bulk R_{xx} and R_{xy} measurements for the filling fraction range $\nu_{bulk} = 3$ to 2, measured in the vicinity of the 1.2 µm QPC before the gates are energized, are shown in Fig. 7.2. R_{xx} and R_{xy} are also measured in a region of the Hall bar without gates, and found to be virtually indistinguishable, showing that the surface gates do not significantly affect the 2DEG. R_{xx} and R_{xy} in an un-gated region show no changes caused by energizing gates.

As temperature is increased, R_{xy} near $\nu_{bulk} = 5/2$ evolves from a well-defined plateau at

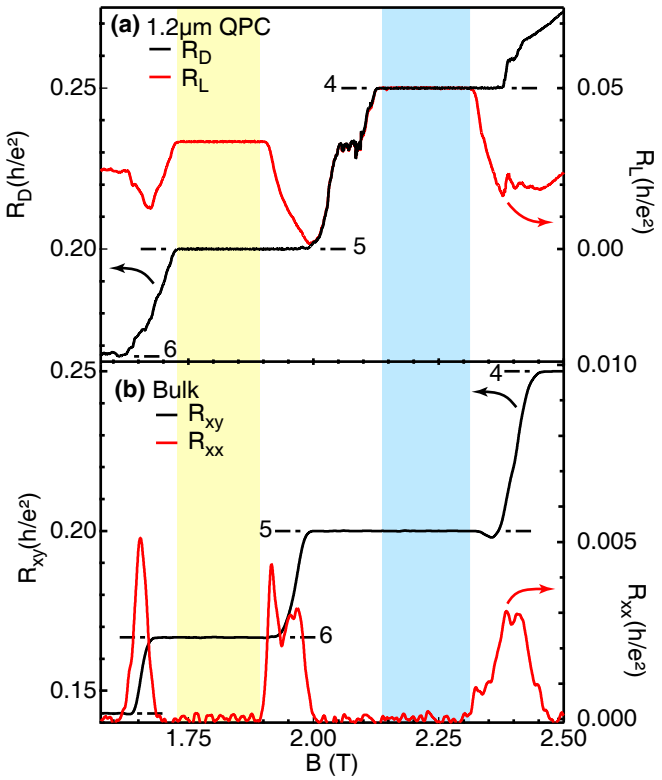

Figure 7.3: Typical IQHE magnetoresistance measured concurrently in the QPC (a) and the bulk (b). Quantized resistance values are indicated in units of h/e^2. The yellow stripe indicates $\nu_{\mathrm{QPC}} = 5$ and $\nu_{\mathrm{bulk}} = 6$. Likewise, the blue stripe indicates $\nu_{\mathrm{QPC}} = 4$ and $\nu_{\mathrm{bulk}} = 5$.

R_{xy}=0.4 $\pm$ 0.0002 h/e^2 to a line consistent with the classical Hall effect for a material with this density. There is a stationary point in the middle of the plateau where R_{xy} is very close to 0.4 h/e^2, consistent with scaling seen in other quantum Hall transitions [25, 223]. Activation energies Δ for the three fractional states $\nu_{\mathrm{bulk}} = 5/2$, $2\,1/3$ and $2\,2/3$ are extracted from the linear portion of the data in a plot of $\ln(R_{xx})$ vs $1/T$ (using the minimum R_{xx} for each FQHE state, and $R_{xx} \propto e^{-\Delta/2T}$), giving $\Delta_{2\,2/3} \sim 60$ mK, $\Delta_{5/2} \sim 130$ mK and $\Delta_{2\,1/3} \sim 110$ mK, consistent with previous measured values [45, 59, 81].

7.6 Demonstration of the QPC in IQHE and FQHE regimes

We now focus on measurements with one QPC formed, as shown in Fig. 1. Low-field R_D and R_L data from the 1.2 μm QPC along with concurrently measured R_{xy} and R_{xx} show regions where one IQHE state forms in the bulk with a lower IQHE state in the QPC (see Fig. 7.3). Figure 7.3 also shows the appearance of a plateau-like feature in the QPC between $\nu_{\mathrm{QPC}} = 5$ and $\nu_{\mathrm{QPC}} = 4$ in both the 1.2 μm and 0.8 μm QPCs which remains unexplained. At higher magnetic fields (Fig. 7.4), R_D and R_L show FQHE plateaus while the bulk is quantized at the IQHE value $\nu_{\mathrm{bulk}} = 2$.

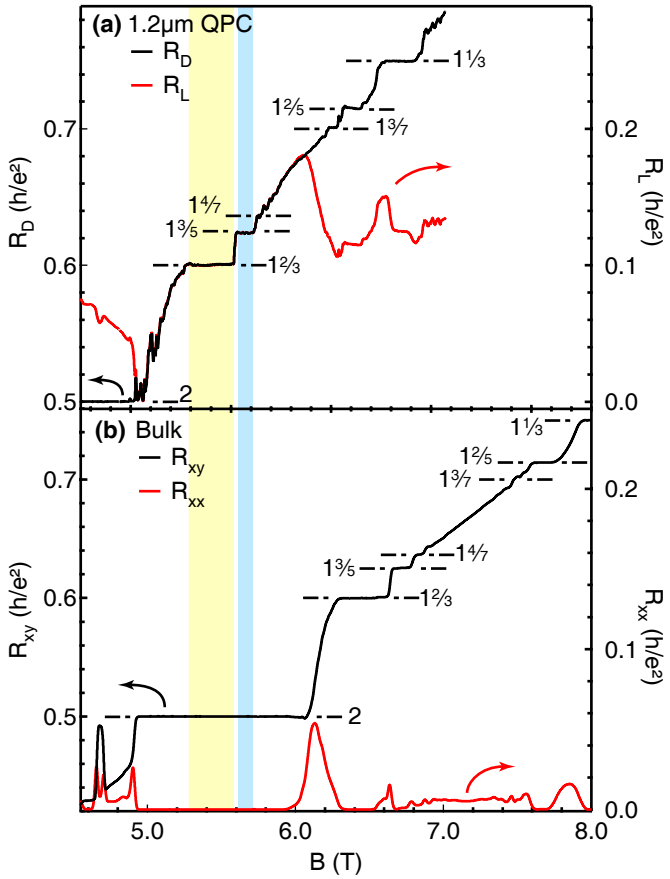

Figure 7.4: Typical FQHE magnetoresistance measured concurrently in the QPC (a) and the bulk (b). Quantized resistance values are indicated in units of h/e^2. The colored bands indicate field regions where selected FQHE states form in the QPC and $\nu_{\text{bulk}} = 2$.

7.7 Observation of plateaus at $\nu = 5/2$

We now concentrate on the range $\nu_{\text{QPC}} = 3$ to $\nu_{\text{QPC}} = 2$ with $\nu_{\text{bulk}} = 3$ (Fig. 7.5). Plateau-like structure near $\nu_{\text{QPC}} = 5/2$ is evident in the 1.2 μm and 0.8 μm QPCs, but is not seen in the 0.5 μm QPC. Near $\nu_{\text{QPC}} = 2\,1/3$ we also see plateau-like behavior in the 1.2 μm QPC, and somewhat less well developed plateaus in in the 0.8 μm QPC (although ν_{bulk} is not on a plateau when $\nu_{\text{QPC}} \sim 2\,1/3$), but again these features are suppressed in the 0.5 μm QPC. We do not observe any plateaus near $\nu_{\text{QPC}} = 2\,2/3$ in any of the QPCs. The reentrant integer quantum Hall effect features [80], which are clearly visible in the bulk, do not survive at all in the QPCs.

We interpret the plateau-like features in the two larger QPCs as indicating that the incompressible states at $\nu_{\text{QPC}} = 5/2$ and $\nu_{\text{QPC}} = 2\,1/3$ are not destroyed by the confinement. The linear, plateau-less behavior in the 0.5 μm QPC is reminiscent of a classical Hall line, suggesting that no incompressible states survive in this QPC.

7.8 Temperature data in the QPC

Temperature dependence for a representative V_g setting of the 1.2 μm QPC is shown in Fig. 7.6. Below 30 mK, a distinct plateau-like feature is evident. This plateau disappears between 30 to

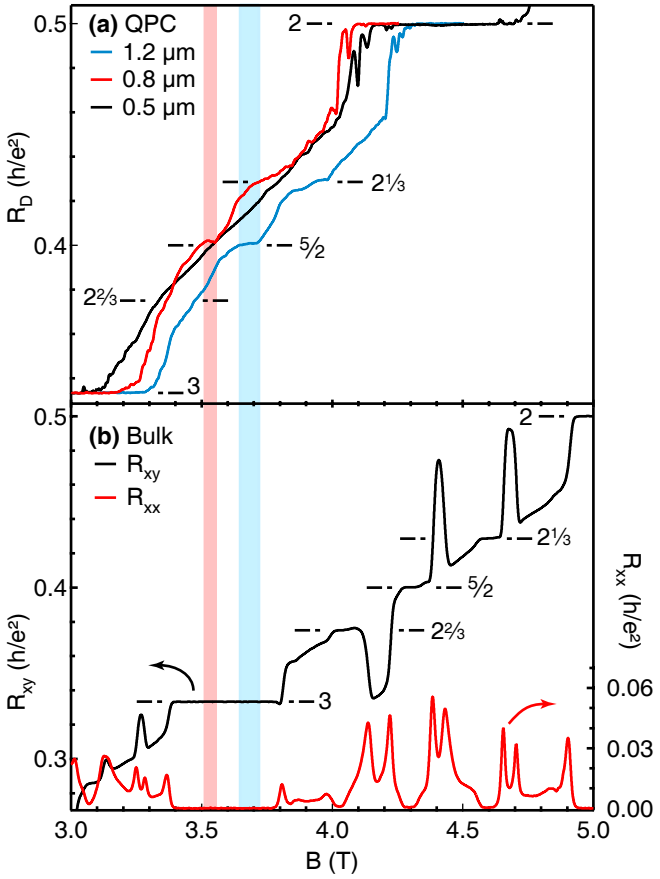

Figure 7.5: Typical magnetoresistance from $\nu = 3$ to $\nu = 2$, measured concurrently in the QPC (a) and the bulk (b). In (a), the R_D curves are from three different QPCs, of lithographic size 0.5 μm (black), 0.8 μm (red) and 1.2 μm (blue). The colored stripes highlight regions in field where the resistance in the 1.2 μm and 0.8 μm QPCs forms a plateau-like feature near $\nu_{QPC} = 5/2$ with $\nu_{bulk} = 3$. The applied gate voltages V_g are -2.2, -2.0 and -1.9 V for the 1.2, 0.8 and 0.5 μm QPCs and the ac lock-in excitation is 0.86 nA.

70 mK, consistent with the disappearance of the plateaus in the bulk. However, unlike the bulk, where the 5/2 plateau disappears symmetrically around a stationary point at $R_{xy} = 0.4\,h/e^2$ as temperature increases, in the QPC there is an additional resistance: R_D exceeds the quantized value of $0.4\,h/e^2$ by $26\,\Omega \pm 5\,\Omega$. We also note that the the extra resistance on the plateau decreases as the temperature increases, behavior consistently observed in both the 0.8 μm and 1.2 μm QPCs. We interpret this as indicating that the temperature dependence comes not only from the thermal excitation of quasiparticles, but also from the temperature dependence of their backscattering.

7.9 I_{dc} data

The dependence of the differential resistance on dc source-drain bias I_{dc} (Fig. 7.7) provides additional insight into this excess resistance. At base temperature, the resistances R_D vs I_{dc} near $\nu_{QPC} = 5/2$ and $\nu_{QPC} = 2\,1/3$ in the 1.2 μm (Fig. 7.7c) and 0.8 μm (not shown) QPCs show pronounced peaks at $I_{dc} = 0$, a dip at intermediate values, and saturation to a constant value at high currents. In these QPCs, the I_{dc} behavior near $\nu_{QPC} = 2\,2/3$ (not shown) is inverted, with a pro-

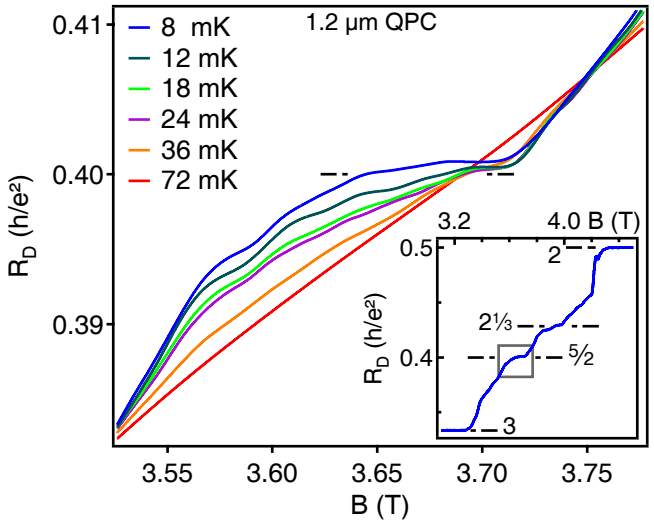

Figure 7.6: Temperature dependence of the 5/2 state in the 1.2 μm QPC. The inset shows an expanded range of the 8 mK trace with the grey box indicating the range of the data in the main panel. All traces are measured with V_g=-2.7 V and an ac lock-in excitation of 0.86 nA. $\nu_{bulk} = 3$ for the entire B range of the main panel, but not the full range of the inset.

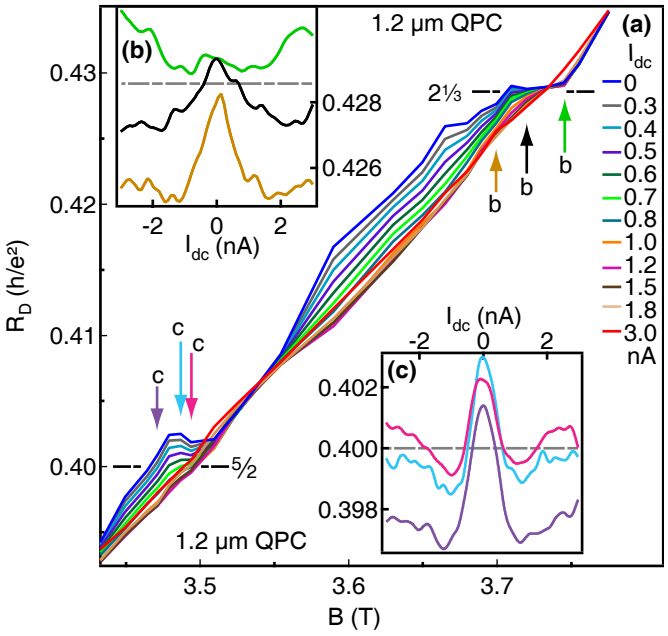

Figure 7.7: Dependence upon dc current bias of the 5/2 and 2 1/3 states in the 1.2 μm QPC. The main panel (a) shows the R_D data as a function of magnetic field; each trace represents a different $I_{dc}$from 0 nA to 3 nA. R_D as a function of I_{dc} for selected magnetic fields (indicated by the color-coded arrows) are shown in (b) and (c). The dotted grey lines in the insets indicate resistance values of $3/7h/e^2$ (b) and $2/5h/e^2$ (c). All traces are measured with $V_g = -2.4$ V and an ac lock-in excitation of 0.2 nA. $\nu_{bulk} = 3$ for all fields shown in this figure.

nounced dip at $I_{dc} = 0$ a peak at intermediate values, and high-current saturation. In the 0.5 μm QPC the I_{dc} traces are flat for all filling fractions between $\nu_{QPC} = 3$ and $\nu_{QPC} = 2$. All the traces in Fig. 7.7 are measured with an ac-lock-in excitation $I_{ac} = 0.2$ nA, (while the data in all other figures

have been measured with $I_{ac} = 0.86\,\text{nA}$).

Fig. 7.7 provides a key point of comparison to previous experimental and theoretical work on the FQHE. In a recent experiment [70], a QPC is used to measure tunneling differential resistance characteristics (I_{dc} curves) for $\nu_{QPC} < 1$ while ν_{bulk} is fixed on an IQHE plateau. Our I_{dc} data for $2 < \nu_{QPC} < 3$ and $\nu_{bulk} = 3$, with a distinct peak at zero bias and dips at intermediate biases, resembles the I_{dc} curves in that work. In Ref. 70 it is convincingly argued that the I_{dc} curves are a signature of quasiparticle tunneling between the FQHE edge states, based on quantitative comparison to applicable theory. That theory states that the characteristic for tunneling between FQHE edge states [29, 72, 224] is expected to have a peak at zero bias and a minimum at intermediate biases [67, 68], whereas tunneling between IQHE edge channels is expected to yield a flat (ohmic) curve. The data we present for $\nu_{QPC} = 5/2$, both the temperature dependence and the I_{dc} curves, are consistent with the formation of a FQHE state with tunneling-related backscattering.

We interpret that a mechanism for the deviation of R_D from $0.4\,h/e^2$ near $5/2$ and $2\,1/3$, as well as the peak-and-dip behavior of the I_{dc} data, could be tunneling between edge channels on opposite sides of Hall bar in the vicinity of the QPC. We do not believe the data can be explained by transport via thermally excited particles through the (small) bulk region of the QPC, since this process would be expected to have the opposite temperature dependence.

7.10 Conclusion

In conclusion, we have observed plateau-like features near $\nu_{QPC} = 5/2$ and $\nu_{QPC} = 2\,1/3$ in QPCs with 1.2 µm and 0.8 µm spacings between the gates. The plateaus disappear between 30-70 mK. At lower temperature, the resistance of the plateau-like feature is higher than the bulk-quantized value of $0.4\,h/e^2$, and increases as temperature is decreased. Near $\nu_{QPC} = 5/2$ and $\nu_{QPC} = 2\,1/3$ in these QPCs the differential resistance exhibits a characteristic shape, showing a peak at $I_{dc} = 0\,\text{nA}$, a minimum near $I_{dc} = 1.2\,\text{nA}$, and approaching a constant value at higher currents. These observations are consistent with the formation of gapped, incompressible FQHE states in the QPC, with QPC-induced tunneling between the edge states. In a QPC with 0.5 µm spacing between the gates, we do not observe a plateau-like feature at any temperature, and I_{dc} is flat for the entire range between $\nu_{QPC} = 3$ and $\nu_{QPC} = 2$. This suggests that in our sample no incompressible states form in this QPC, because of either confinement or the effects of decreased electron density. All of these measurements have been carried out in a magnetic field range where the bulk filling fraction was on the IQHE $\nu_{bulk} = 3$ plateau, while the ν_{QPC} was tuned to lower values via the gate voltage.

7.11 Acknowledgements

We gratefully acknowledge helpful discussions with M. Fisher, B. Halperin, A. Johnson, E. Kim, B. Rosenow, A. Stern, X.-G. Wen and A. Yacoby. Research supported in part by Microsoft Corporation Project Q, and HCRP at Harvard University, and ARO (W911NF-05-1-0062), the NSEC program of the NSF (PHY-0117795) and NSF (DMR-0353209) at MIT.

Appendix A
Raith Users Guide

I made a lot of devices during the course of my PhD. One of the trickiest parts of the device fabrication process is electron-beam lithography. A small part of the trickiness is that making arbitrarily-shaped 30 nm gold lines (that is, lines of gold only about 200 atoms wide) is near the edge of technological capability. It is near the edge, but it is not *over* the edge. At Harvard, the main part of the trickiness is the "Raith," a slightly rickety pile of passable hardware and defective software. Over the course of time, the Raith users at Harvard developed methods to "outsmart" the defective software and push the hardware to the white-knuckle edge of functionality (ie, we got the thing to work to spec). I wrote these methods down in *Jeff's (Fairly Comprehensive) Raith Usage Notes*, a document that became the *de facto* Raith user's manual at Harvard [225]. I'm rather proud of this little document, which I have included in its original form in this Appendix.

[*Jeff's (Fairly Comprehensive) Raith Usage Notes* start on the next page]

Jeff's (Fairly Comprehensive) Raith Usage Notes

Jeff Miller, Marcus Group, Harvard University. Print this out on cleanroom paper. Version 20040929.1

This document is intended to be a friendly, fairly comprehensive guide to using the Raith Electron Beam Lithography system, including tricks to get small dots to write nicely even if the Raith is not being nice. Written primarily as an appendix to Jeff's thesis, it should be updated whenever somebody learns a new trick.

Pre-Raith Preparation

Design the Device

Use DesignCAD to make your device. Here are a few basic design tips, I'll add more later if I feel like it.

In general, the depletion length is approximately the same as the depth of the 2DEG, and the wavelength of the electron is determined by the density of the material. For example, say you have a material with a wavelength of 50 nm and the 2DEG is 100 nm below the surface, and you want to make a point contact that is will have at least 3 conductance plateaus. You need to space the gates at least 350 nm apart (100 nm each for depletion length, 50 nm each per plateau).

Once the design is finished, it is useful to specify the write-order of the gates. Gates will be written in the order that they were added to the DesignCAD file. Of course, you were not likely to have designed the device in the same order you would like it to write, so you will have to make a new file and paste the gates into it in the correct order. Alternatively, I have written a little DesignCAD macro that you can use to specify the write order of the gates. I usually write my "smallest" gates first, and I am careful to write the gates that would be most sensitive to Raith stage drift consecutively.

Make a GDS file

- From DesignCAD, export your design as a DXF file.
- Using LinkCAD (installed on the design computer), convert to a GDS file.
- Save the GDS file on a diskette for transfer to the Raith computer.

Spin On PMMA

For quantum-dot-sized gates (features sizes down to 50 nm or smaller) it is best to use a single layer of PMMA. The recipe here results in a PMMA thickness around 200 nm, which is thick enough to result in easy lift-off but thin enough that narrow towers of resist between nearby gates do not tend to fall over.

- 3-solvent clean (TCE→Acetone→Methanol), 5 min each, in ultrasound.
- Bake 2 min at 180°C (to drive off water)
- Spin on PMMA 950K 3% in Chlorobenzene. Set up spinner with a 5 s spin-up at 500 RPM followed by a 40 s spin at 4000 RPM. Use a ramp rate of 2000 RPM. Use a glass pipet to place a few drops of PMMA on the sample during the 5 s spin-up.
- Bake 10 min at 180°C to harden PMMA.

Raith Procedures

Copy GDS file to Raith Computer

- Insert the disk with your GDS file into the Raith computer (the CPU is located directly under the loading port)
- Copy the file into an appropriate directory on the Raith computer hard drive. The Raith computer monitor (as opposed to the Leo computer) is the one on the left.

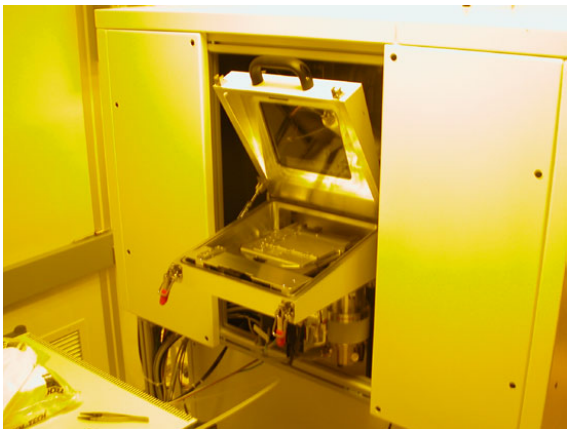

Sample loading port on the Raith.

Load Sample

- Carefully remove the sample holder from the sample loading port. Do not drop the sample holder (as some people have previously done).
- If there is any silver paint on the front of the sample holder, carefully clean it off with acetone and a cleanroom wipe or a cleanroom Q-tip.
- Liberally blow-off the front and back of the sample holder using compressed nitrogen. Be sure to remove all dust and cat hair from the three holes on the back of the holder; anything sitting in these holes will lead to drift.

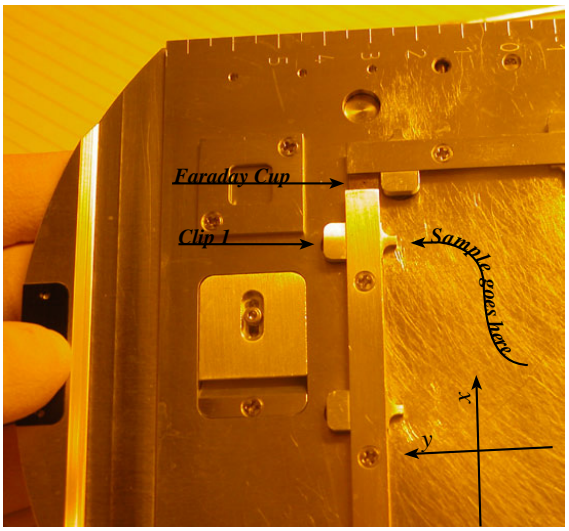

Front of the sample holder, showing the Faraday cup and clip 1. Secure your chip with clip 1, oriented correctly as indicated.

- Wearing gloves to protect the Raith from your greasy, hairy, dandruffy hands, replace the sample holder into the loading port. Install your chip as shown, correctly oriented.
- Use only soft tweezers around sample holder. Note the numerous scratches caused by inconsiderate people who have used metal tweezers.
- Close the port and fasten the two clamps.

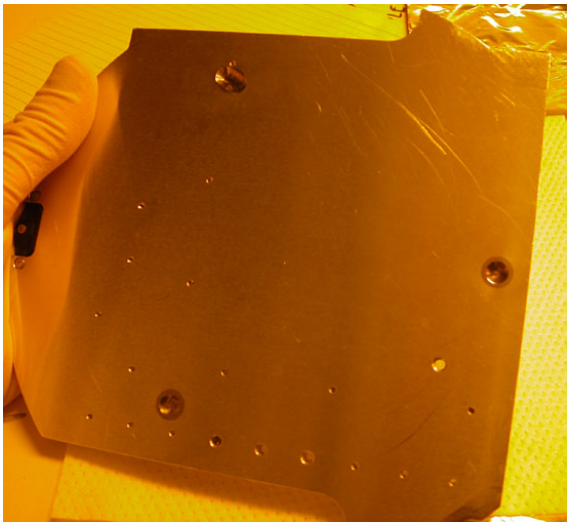

Back of the sample holder. Be sure to blow out the indicated holes.

The Raith computer is on the left, the Leo SEM computer is on the right. The joystick (far left) is used to move the SEM stage.

- Start the Raith software, and activate your user account.
- If needed, activate the “Navigator Exchange” window by clicking on the stop-light near the Roman numeral I on the command bar. Click the Load Sample

button.

- If all goes well, your sample will be loaded in about 10 minutes. If wearing a bunny suit (or snowpants) causes a psychological need for you to pee, now would be a good time, because the next few steps take a while.

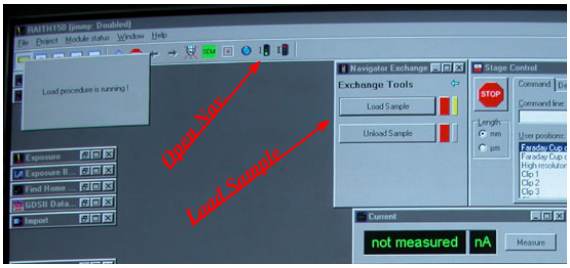

To display the Navigator Exchange window, click the "I stoplight." Load and unload sample buttons are available in the Navigator Exchange window.

Initial Setup

- After sample is loaded, Raith asks several questions: "Reset coordinate system?" (Yes); "Switch on beam?" (Yes); "Select accel. Voltage" (30 kV); "Aperture size" (10 µm); "No values for astigmatism and aperture align in database" (OK).
- The beam current ramps up over about 1 minute or less. Note the time in your lab book, it is nice to know how long the beam has been warming up before you begin writing.
- While the beam is ramping up, open the "Find home" window, and click the lightning bold to find home in the x-direction, then the y-direction. I do this operation every time I load the Raith, because I think it reduces drift problems caused when the sample holder is poorly seated on its three-pin suspension system.

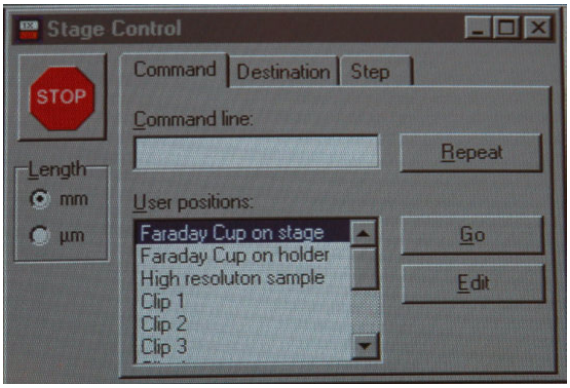

- In the "Stage control" window, under the "command" tab, select "Faraday cup on holder" and click go. This drives the stage to the Faraday cup.
- Turn on the beam by clicking the beam blank/unblank button on the Raith computer command bar:

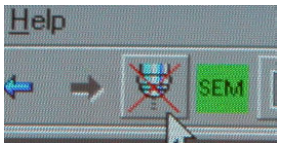

- On the Leo SEM computer (the right computer), turn on the "SEM control" window by clicking on the red-and-green-circular-dial-looking button on the command bar.

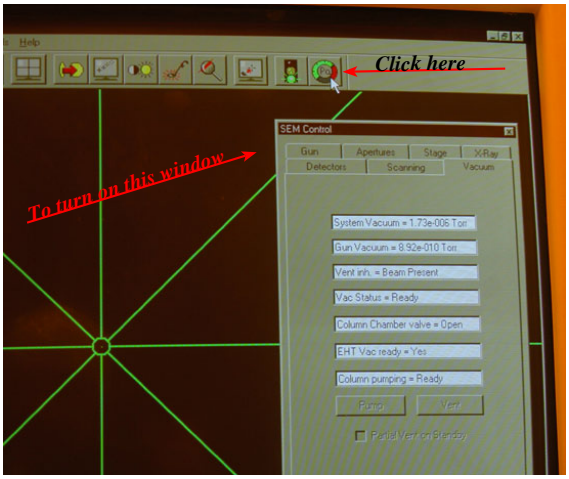

- Click on the "Detectors" tab and set "Signal A" to "SE2." Set the brightness to about 52%, the contrast to about 43%.
- To set the zoom of the Leo, first click on the zoom/focus button on the Leo control bar (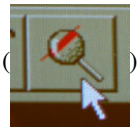) hold the left mouse button of the SEM mouse, and move the mouse left or right (to zoom out or in). Zoom all the way out.
- Look for the Faraday Cup.
- Use the joystick to move center the left-hand edge of the Faraday cup under the green crosshairs. If the green crosshairs are not visible, they can be toggled using the indicated button.

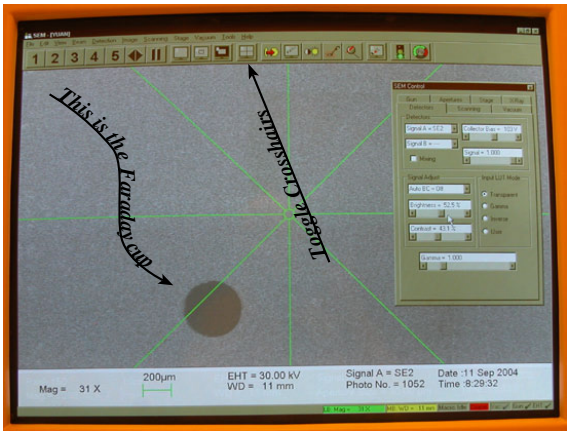

- Focus on the metal burr on the left hand side of the Faraday cup. To focus, hold the center mouse button on the Leo mouse and drag left or right.

- Click the "Apertures" tab on the SEM control panel.

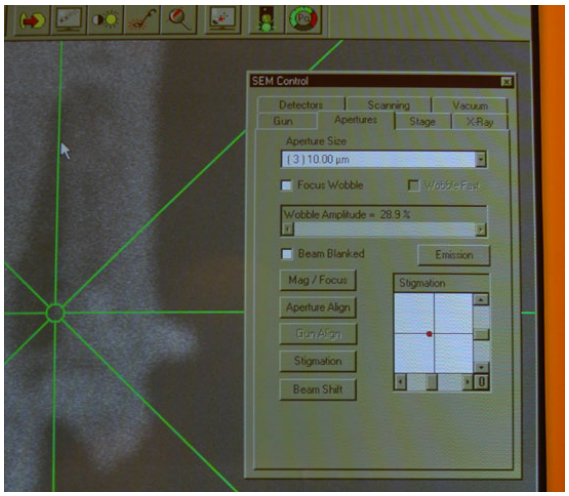

- Zoom to about 50 kXClick the "Focus Wobble" box, then the "Aperture Align" button. After clicking the "Aperture Align" button, the current values for the aperture alignment appear in a green box at the bottom of the SEM screen. Double click this box to enter the alignment values from your previous Raith session as a starting point.
- Fine tune the aperture alignment by either dragging the red dot in the SEM control panel, or by moving the slider bars, or by (after clicking the Ap. Align button) left-click-dragging up/down or left-right on the SEM image. The alignment is correct when the image does not move due to focus wobble, but instead only changes focus.

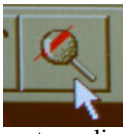

Click on the magnifying glass button on the control bar to return to zoom/focus mode. (Otherwise when you try to zoom/focus, you will accidentally adjust the aperture align). Refocus, zoom in, repeat.

- Click the "Stigmation" button. Enter the previous good stigmation values in the green box. Unless somebody turns the filament off or otherwise crashes the system, the stigmation values are fairly stable from day-to-day, so write your values down to use next time.
- Zoom to about 100 kX or higher. Fine tune the stigmation. The idea is to first focus, then try to improve the focus and eliminate directionally-preferential focusing by adjusting the stigmation.
- Again refocus, zoom in, repeat.
- A sufficiently long time after ramping up the beam (I usually think 20-30 minutes is long enough) center the crosshairs over the Faraday cup and zoom all the way in.
- Open the Current window and click the "Measure" button to measure the beam current.

- This is a good time to set up the default exposure parameters. Open the "Exposure" window.

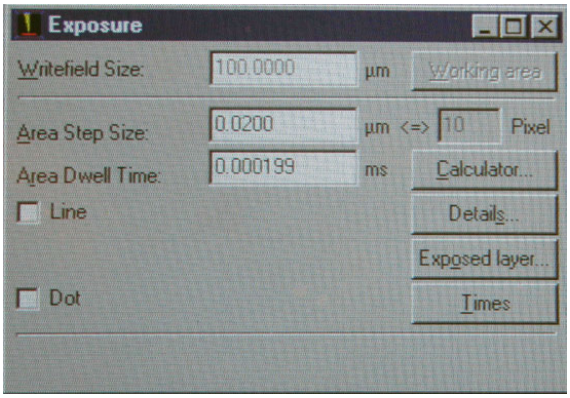

- Click on the "Calculator" button to open the "Exposure Parameter Calculator" window.

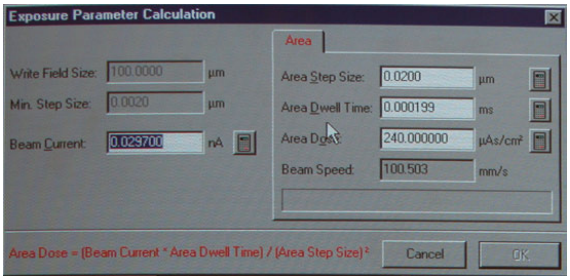

- Enter the Area Step Size (0.006 µm) and the Area Dose (100 µAs/cm^2). Click on the calculator icon on the Area Dwell Time line to calculate the dwell time (aprox 0.00134 ms). Note that the Beam Current is shown to higher precision in this window than anywhere else in the Raith software.
- Check that the beam speed is less than about 4 mm/s to avoid breaks and other problems.

Set up the coordinate system

- Blank the beam
- Use the stage control window to drive to clip 1. If you want to watch the stage move, you can switch to TV view mode by clicking the TV button on the SEM control bar: . Switch back to SEM view by clicking .
- Zoom to about 250x. Make sure the beam is unblanked. You should be able to see the upper right-hand side of the sample clip, which looks like this:

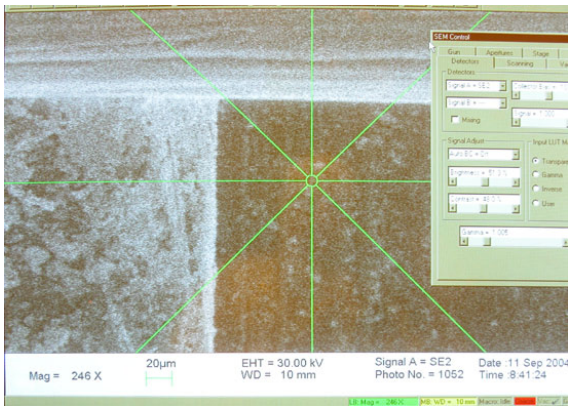

- Use the joystick to move along the clip edge until it begins to taper in. Soon you will be able to see the corner of your chip. Don't linger too long, or you could start to expose the PMMA, although at this low magnification you have up to 30 seconds before you start to expose.

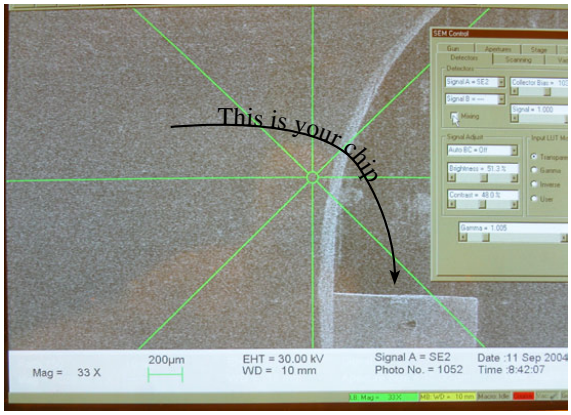

- Zoom in to about 500x.
- As quickly as possible, use the joystick to navigate along the edge of your chip to a place where you expect to find alignment marks.
- Focus on anything you can find (i.e., the edge of the chip).
- Find your alignment marks, trying to stay near the edges of the chip to avoid exposing active areas of the chip. If you need to stop and think, blank the beam.
- Focus on the alignment cross as well as possible.
- Center the crosshairs on the cross, zooming in to minimize error.

- Open the “Adjust UVW (Global)” window, and click on the “Origin Correction” tab.

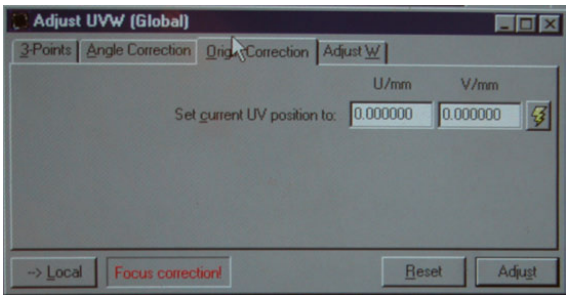

- If the button at the lower left reads “-> Global”, click it so that it reads “-> Local.” (You want to set the Global UVW).

Enter the coordinate position of your alignment cross in the U and V set-variable area. For instance, if the center of your design is (0,0), your alignment cross may be located at (0,-0.475).

- Click the “Adjust” button to adjust the origin of the UV coordinate system. (Note: the XY coordinate system never changes, but the UV system should be changed to match your photolithography step, as we are now doing).
- Click the “Angle Correction” tab.

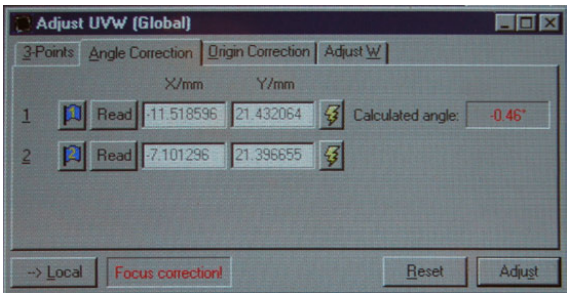

- Click the “Read” button on line 1.
- Keep the beam on, and move to the exact center of another alignment cross which is supposed to be horizontally colinear with your origin.
- Click the “Read” button on line two, and click adjust. The angle of the UV coordinate system has now been set. However, thanks to Raith software technology, your origin has been screwed up. Go back to your first cross, center on it, and repeat the origin correction step. NOW, the origin and angle of the UV coordinates are set, so it should be possible to move around your sample by entering absolute or relative coordinates in the “Stage Control” window.

Focus Correction

Good focus is critical not just to achieve small-size features, but also to get robust, reproducible results in terms of exposure. In other words, if the spot-size of the beam changes from one write session to the next, you will not be able to control the dose correctly.

The method presented below will yield three results. First, you will be able to correctly set the working distance to the surface of the PMMA with an accuracy of better than 1 µm. By contrast, if you try to focus on one of your alignment marks (below the PMMA, additional 200 nm error) or some silver paint (unknown thickness) your accuracy will probably only be about 50 µm (or much worse). A 50 µm error in working distance corresponds to an increase of about 131 nm in the spot diameter—a terrible error for devices with 50 nm feature sizes! Second, you will be able to see the size and shape of the beam before your write, so you know when to stop tweaking the focus and aperture and start writing (a time saver) and you can verify consistency between write sessions. Finally, you can reliably correct for the angle of your chip (using three-point correction) so that the focus is correct not just at your alignment marks, but anywhere you want to write.

- Choose three (non-colinear) points on your chip to use as the focus locations. I typically choose the center of three alignment marks distributed around my target mesas.

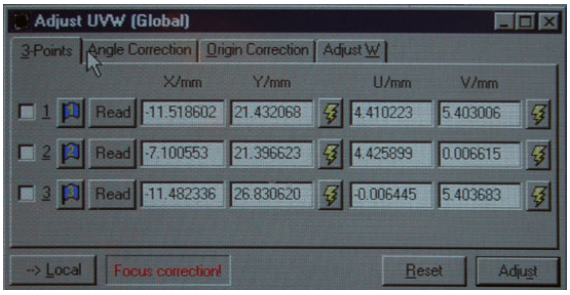

- Enter the (u,v) values for these three points into the U and V columns of the "Adjust UVW (Global)" window.
- Make sure you see the message, "Focus Correction!" displayed in red on the "Adjust UVW (Global)" window. If not, turn focus correction on under "Project→ Options."
- Make sure the beam is blanked, then click the UV lightning bold on line 1 to move to your first point. If your point is an alignment cross, then first focus on the cross as well as possible up to a zoom of about 50 kX.
- Use the joystick to move a bit away from the cross, and zoom in to about 300 kX.

Center-click the "Short/Spot" button to stop the beam from rastering and to hard-bake a spot into the PMMA at the location of the crosshairs. Wait for 30 seconds, then center-click the button again to return to normal SEM mode. Because the working distance is probably off by up to 0.1 mm, the beam will not be very concentrated on the spot and it takes a long time (30 s) to burn a visible spot.

- After returning to normal SEM mode, it may or may not be possible to see a faint, ghostly blob. You may need to zoom out to about 100-200 kX if the spot is quite large.
- Focus on the ghostly blob. When the focus is correct, the ghostly blob looks more like a ghostly doughnut; that is, brighter around the edges and darker in the middle.

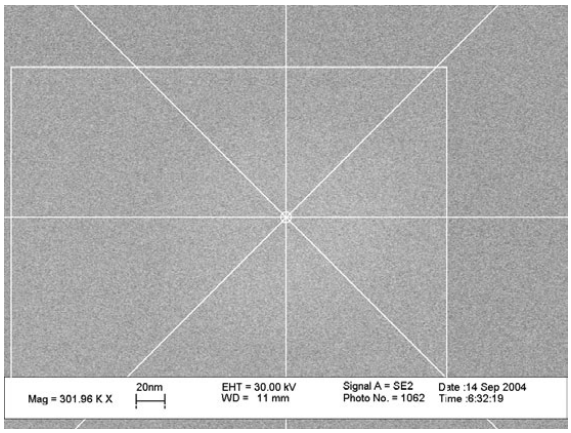

This ghostly blob is the result of a 30 second burn after focusing as well as possible on the nearby alignment mark. A creative eye is required, and it doesn't hurt to believe in ghosts.

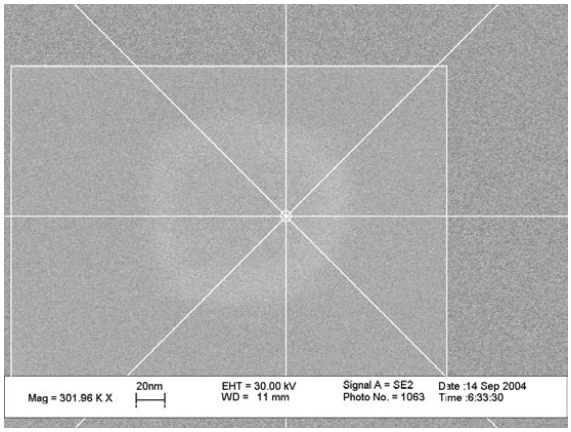

Here is the same 30 second spot, in focus. You can tell the spot is in focus because it looks like a ring or a doughnut. Notice the diameter is about 120 nm.

- After focusing, tap the joystick to move away from your 30 second spot, and burn another spot for about 10 seconds. This spot should have a much smaller diameter because the beam is much better focused (which is also why a shorter burn time can be used).
- Focus on the 10 second spot, move away from it, and burn a 5 second spot.

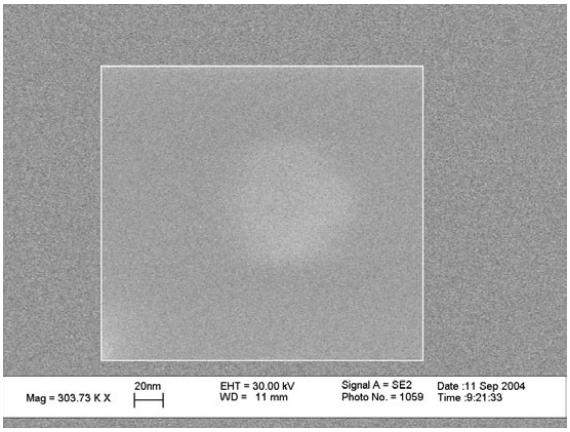

A spot burned for 10 s, after focusing on a 30 s spot.

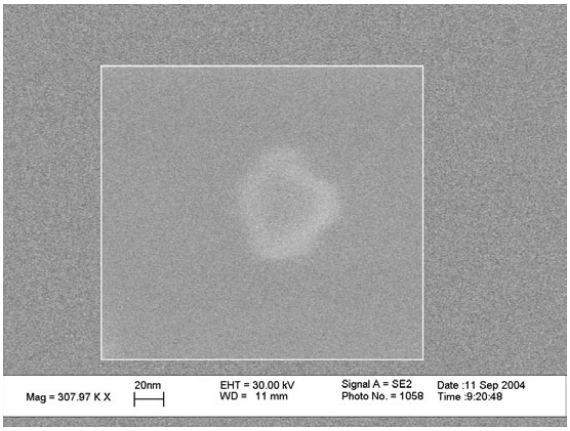

The same 10 s spot, after focusing.

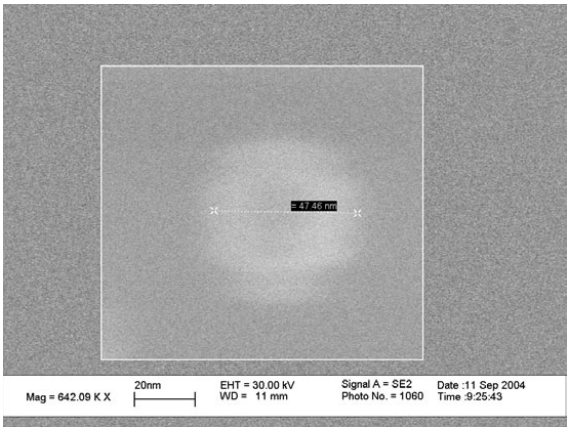

A 5 s spot, in focus. You will know that the working distance is correct when the diameter is 40-50 nm; no more focusing is required. Note that the zoom here is ~650 kX.

- When the spot size is 40-50 nm, the working distance is correct for this (u,v) location.

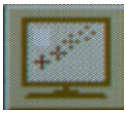

If the spot is not circular, you will need to adjust the aperture until it is circular. I always click the marker button to put two measurement markers on the SEM image to check the diameter in the two "45 degree" directions, otherwise the optimistic eye can be fooled into believing that an oval is a circle.

- Once the working distance and the aperture are correctly set, these values need to be fed to the Raith computer. In the "Adjust UVW (Global)" window, click the "Read" button on line 1 to get the (x,y) coordinates and the working distance of the current location. Type the current (u,v) coordinates into the U and V columns. These values can be found in the "Coordinates" window. It is important to enter the (u,v) values correctly, or the entire UV coordinate system could become stretched, rotated, or shifted!

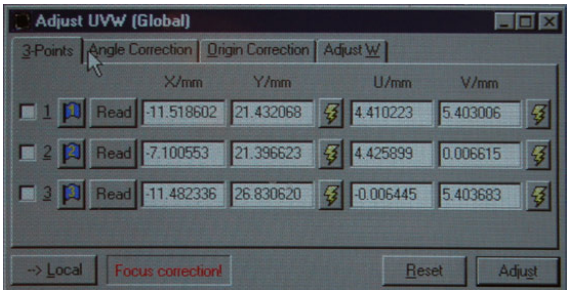

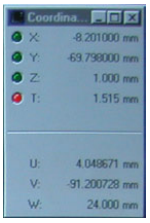

- Click the checkbox on line 1 to tell the Raith that everything is set.
- Blank the beam, click the UV lightning bolt on line 2 to move to your next focus location, and repeat the entire focus procedure.
- Repeat for line 3.
- When all three checkboxes are clicked, click the "Adjust" button, which causes the Raith to use the new values for focus correction.
- Think your done? No way! The Raith software now requires you to repeat the ENTIRE procedure. Uncheck all the boxes and repeat the entire focus procedure again. Seriously. Don't ask me why the raith software doesn't work. At least this time the focus is

usually easier.

- After finishing the entire focus correction procedure for the second time, the focus correction is usually correct. Verify this by moving to several selected locations and burning a 5 second spot, which should be 40-50 nm in diameter. If so, focus correction is finished.

Write Field Alignment

Finally, the beam needs to be aligned to the UV system.

- Open the "Microscope Control" window and double check that the magnification is 550 and the Field Size is 100 µm.
- Make sure the "Align Writefield" window is visible.

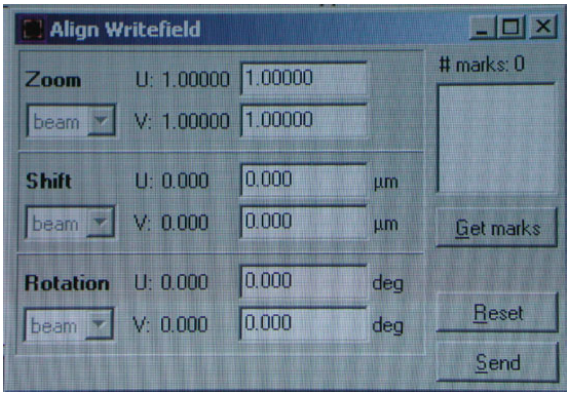

- Zoom to about 550X and position the crosshairs on some easily identifiable feature. Zoom in to a few kX to make sure the crosshairs are correctly positioned, then zoom back to 550X.

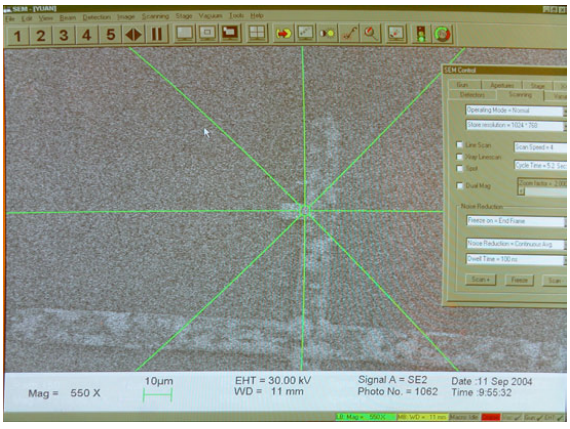

- Click the green SEM button on the Raith computer

to freeze the SEM image and assign control of the LEO to the Raith.
- Blank the beam.
- Open a new position list (File→New Position List) and make sure it is selected.
- Click on Filter→Align Writefield. The Align Writefield Window opens.

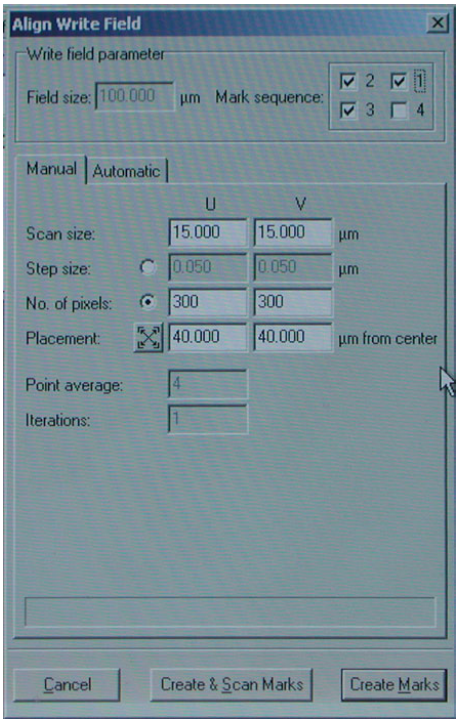

- In the "Manual" tab, set the Scan Size to 50x50 µm.
- Click the "Create & Scan Marks" button.
- The magnification will be automatically set, and a slow scan image will be displayed on the Raith computer.

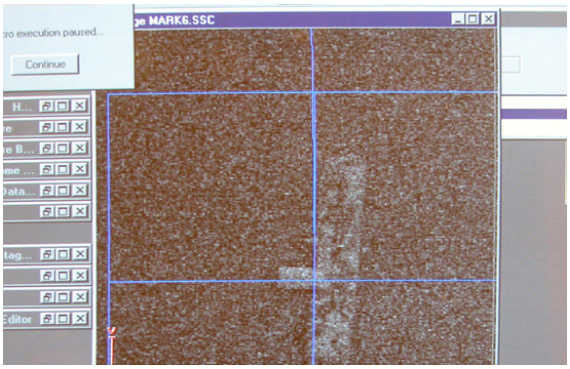

- While holding the “Ctrl” key, drag the center of the green cross to match the crosshairs on the SEM image (the cross turns blue).
- Click “continue.” Two more slow scans will be presented, align the cross in each one.
- The Raith asks if you want to accept the changes. You can examine the changes to Zoom, Shift and Rotation in the “Align Writefield” window. Accept the changes.
- Unblank the beam, reactivate user control of the SEM (click the button).
- Move just off the edge of your alignment mark, zoom in to 300 kX and burn a new spot. Zoom out enough to see the spot and a good portion of the alignment mark. If you do not move the joystick and there is no drift, the crosshairs will be exactly centered on the burn-spot.
- Click

and blank the beam, repeat align writefield procedure with a scan size of 10 µm.
- After the align writefield procedure is complete, again go back to the SEM and make sure the spot is exactly in the crosshairs. Repeat again with a scan size of 5 µm, then again with 1 µm.
- Repeat the align writefield procedure until the changes are acceptably small. Specifically, the change in zoom should be a factor between 0.99975 and 1.00025, which for a 100 µm writefield, yields a zoom error of 25 nm or less per writefield, which should not result in stitching errors. The shift error should be just a few nm, and the rotation error should be a few 0.001’s of a degree.
- Write these values down in your lab book. Interestingly, the values for zoom have been about 1.37767 and 1.40704 for years.
- At this point, you could re-measure the current (using the Faraday Cup) if you desire. If you do, be sure to double-check your origin when you return to the sample, as large stage movements have occasionally resulted in measurable shifts. If necessary, you can re-origin the UV coordinate system without ruining all the work you have already done.

Writing the pattern

At long last, it is time to write the pattern. Writing an exposure matrix, is the first step in any Raith fabrication; before writing any device on valuable 2DEG, an exposure matrix should be written on junk (be sure the junk is the same material as the 2DEG, as different materials can have different electron backscattering properties). Once the device is shown to repeatably work at some exposure, it is time to write the real device on the real 2DEG.

- Open the “GDSII Database” window., and make sure the GDSII window is active
- Click on File→Open Pattern.
- Click “Edit.”
- Hit ctrl-a to select all your gates, etc.
- Click Modify→Dose→Set, and enter a dose value of 1.0. This ensures that all gates are assigned a dose. If you forget this step, the Raith won’t bother to write any of your gates.
- Click the button to view the editing tool palette. Zoom in if desired. Double click on gates to view more information, and set alternative dose levels to certain gates if desired. (For instance, on a particularly thin gate, you may wish to boost the dose to 1.2, to give that gate 20% more dose).

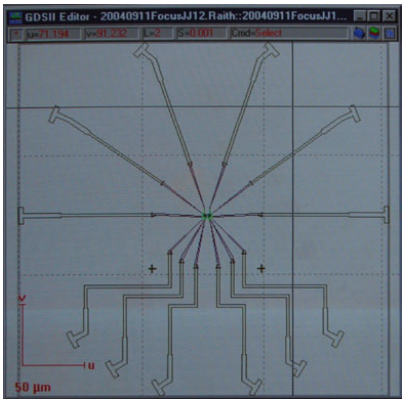

- Close the “GDSII Editor” but be sure to save the new GDSII data.
- Click File→New Position List.
- Drag your pattern from the GDSII database onto the position list.
- Right click→Properties (on the pattern in the position list) to open the “Exposure Properties” window.
- Enter the layers you would like to write. Typically, for an exposure matrix, you will enter just the 1-3 layers with the smallest features. When writing the real device, I typically write just these small features (i.e., everything that fits into a single working area) and then specify a second “position” in the position list for the larger gates.
- Enter the working area and position. These steps are actually a bit confusing. The working area is the portion of your design that you would like to write. For instance, if you are writing an exposure matrix, you may only want to write the central 10 µm of your device. You could therefore specify the working area to be -5 µm to 5 µm in both U and V. However, you may instead want to specify a working area that is an integer multiple of the writefield size (writefield size is 100 µm) because it simplifies the calculation of the position (special Raith feature). In that case, you would design your layers in such a way that exposure-matrix-sized chunks are defined by layer. If the total size of your pattern is larger than a single writefield size, I urge you to specify the working area in enough integer multiples of writefields to contain the pattern. For example, if your pattern is 2.2 mm by 1 mm, specify a working area of U: -1150 µm to 1150 µm; V: -550 µm to 550 µm. The result is a working area that is large enough to contain the entire pattern, built out of integer multiples of 100 µm. Also note that the critical area around (0,0) is not divided up between different write-fields, so you don’t have to worry about the Raith “stitching” your device incorrectly.

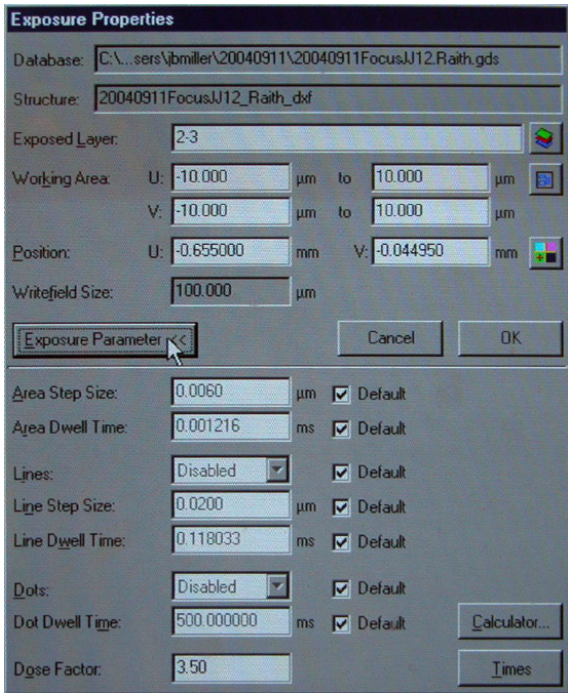

- Now specify the position. The position you enter into the exposure properties window specifies the location of the center of lower-left-most writefield. By the way, if the working area is smaller than one writefield, then the lower-left corners of the writefield and the working area are coincident. For instance, say you want to write a 10 µm square portion of your device at the center of your mesa, centered at position (0,0). If you specify a working area in both U and V of -5 µm to 5 µm, with a writefield size of 100 µm, then you need to enter the values (0.045 mm,0.045 mm) for the position. This is a little confusing and can lead to errors, so an alternative method would be to specify an working area of -50 µm to 50 µm. Restrict the size of the pattern by choosing only select layers. In this case, the position would be (0,0), which is much less likely to cause confusion. Finally, for example, say you want to write your 2.2 mm by 1 mm pattern with a working area of U: -1150 µm to 1150 µm, V: -550 µm to 550 µm at the center of the mesa. The correct position to specify is (-1.1 mm,-0.5 mm).
- Set the dose Factor. For example, if you specified the default dose to be 100 µAs/cm^2(using the dose calculator window) but you want to write the pattern at 300 µAs/cm^2, enter 3.0 into the Dose Factor

box (click the “Exposure Parameter” button to display the Dose information). Usually, if you set up the dose when you measured the beam current, all the boxes can be clicked “Default.”

- Create more positions if desired. One way is to shift-drag existing positions to copy them, then modify some of the parameters as needed. Another way, particularly useful for exposure matrices, is to select the position then click Filter→Matrix Copy. The “Create Position Matrix” window opens, and you can specify a step-size and a dose-factor. The selected position will be duplicated as many times as you specify, offset by the step-size and with the specified dose factor increments.
- When you have all the positions you want, click Scan→All. The Raith moves the stage to the correct location and exposes the PMMA. On screen, you will see a graphical representation of the order in which the gates are written. Incidentally, this representation is the size of the working area, so if you have specified a smaller area you can track the progress much more clearly. If you want to be sure something is actually, happening, you can double check that the red LEDs on the High Speed Pattern Processor are moving and the current (measured when the beam is blanked) is fluctuating on the picoammeter.

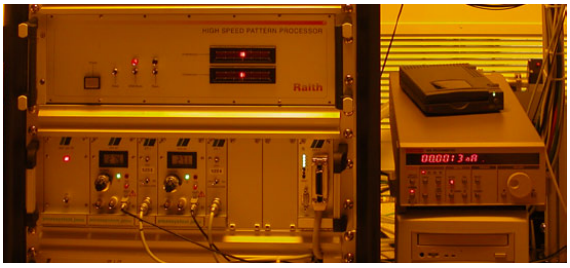

Finishing

- When you are finished writing all your devices, click “Unload Sample” in the “Navigator Exchange” window, and wait 10 minutes.
- Remove your sample, close the door.

Post-Raith Processing

Develop

- Develop the sample in 3:1 Isopropyl Alcohol:Methyl Isobutyl Ketone solution for 1 minute. Rinse in Isopropyl Alcohol, and blow off.
- You should be able to see your pattern in the PMMA under the microscope.

Evaporate

- Evaporate.

Liftoff

- Liftoff in Acetone. Let the sample sit for at least an hour, preferably overnight.
- Be bold, give it a good shot of ultrasound. I’ve never seen a gate lift off due to ultrasound (although several reviewers of this document tend to disagree).

View or use

- If you made an exposure matrix, view it in the SEM.
- If you made a device, finish your last photo steps and, measure, publish a paper, and graduate.

Appendix B
Detailed Fabrication Procedures

This Appendix, written primarily for Eli's benefit but likely to be of use to any new users of the McKay cleanrooms, covers all aspects of fabrication except evaporation, which is trivial, and e-beam lithography, which is covered in Appendix A. I have tried to include some information about *why* we do things, not just *how* we do them.

B.1 Getting Started

Obtain supplies from the chemistry stock room or around the lab: toolbox, safety glasses with anti-UV coating, pyrex petri dish with lid, a few glass microscope slides, Carbofib tweezers[1]

Obtain material.

B.2 Cleave

Cleave the material. To achieve cleave-position and chip-size precision near 100 µm, use the cleaver in the upstairs cleanroom. Turn on the nitrogen gas. Turn on the pump (under the table). Turn on the cleave-unit (power switch left-side rear). Start the "LSD" software. Adjust the scribe-tool pressure and the break force. When initialization is finished, place your wafer-to-be-cleaved on the blue tacky tape. The cleave direction is front to back, along the right-hand side of the metal bar under the tacky tape. Align the wafer cleave-axis with this bar as well as possible by hand, then be sure that the wafer is sticking to the tape under its entire area (or else the scribe may push it aside instead of making a scratch). Use the rotation arrow buttons to align the wafer rotation with the on-screen cross-hair reticle. Make sure the angle is correct by checking that an entire side of the wafer is aligned with the reticle (move the wafer with the translation arrow buttons). Move the wafer so a left or right edge is aligned with the vertical reticle. Enter the desired size of the chip into the x-translation variable-entry-box by clicking on the units to the right of the entrybox. Send the dimension to the x-axis. Move exactly this distance by clicking the blocky left or right triangular arrow button. Make sure that the mode is "Scribe and Break", and that the stop-hook above the threaded rod (used to stop the cleave-carriage in peck mode) has been lifted. Click "S1" to scratch the wafer; the scribe will scratch along your wafer from front to back along the vertical reticle. You may choose to break the wafer by hand. If not, place a clean Kimwipe on your sample (to protect the surface from accumulated evil crap on the roller wheel) and press the "B1" button to break the wafer along the scrbe-line.

It is also possible to measure x- or y- dimensions. For x-measurements, move the vertical reticle to one side of your object-to-be-measured, click the "X1 Ruler" button. Move to the other side, click the button again. The x-dimension will be displayed in the x-translation variable-entry-box.

[1] Good tweezers for handling chips are the anti-Magnetic, anti-acid stainless steel ones, with "carbofib" tips, available from techni-tool.com. They are ESD safe, soft and non-scratching.

When finished, exit the LSD program (click the file cabinet button), turn off the scriber, the gas, and the pump. Sign the log book. Clean off the break-wheel wiht IPA and a Kimwipe.

B.3 Mesa Photo

In the upstairs cleanroom, make sure that the AB mask aligner light-source powersupply is turned on. This powersupply is on a shelf under the table. If it is on, it will be possible to see a blue glow around the light-source housing. If it is not on, flip on the circuit-breakers, wait about 10 minutes, then press and hold the fire button until the starter fires (with a loud click). The light should now be visible, but if not try firing again. Incidentally, the lamp should cool for 30 minutes after the last person turned it off before you fire, so make sure the last user didn't just turn it off. Typically, you do not need to turn the lamp off, unless you are the last user of the night (how would you ever know this?). To turn it off, switch of the breakers.

Clean the chip. Find four fluoroware beakers and label them TCE, ACE, IPA and DI H20 (you can keep these beakers and use them over and over). Pour a little TCE (trichloroethylene) into a fluoroware beaker. Put the chip in the TCE and put the beaker in the ultrasound bath (on/off buttons are on the panel above the fume-hood shield) for 5 minutes. TCE removes grease. If the level in the bath is too low, add a little deionized (DI) water. If the beaker floats, add more TCE, or try to remove some water from the bath. After 5 minutes, transfer the chip to another beaker of Acetone for 5 minutes. Acetone removes photoresist and other organic impurities. Next, transfer to IPA for 5 minutes. IPA removes the acetone. Next, transfer to DI water for 5 minutes. Water removes all the solvents, and can itself be completely removed from the surface of the chip through evaporation. Organic solvents form a monolayer on the chip surface that will not evaporate, even at 180 degrees C. DI water is available from the plastic gun-like dispenser in the fume hood. Always check that the resistance on the DI water filter is 18.2MOhms or higher.

Upon removing the chip from the water, blow it off with compressed nitrogen immediately. While blowing, hold the chip on a cleanroom wipe, so any liquid that is tempted by surface tension to cling to the sides will be wicked away. IF any liquid of any kind is ever allowed to dry on the chip, it WILL be carrying some solid impurites which will precipitate onto the surface and potentially ruin the chip.

Drive away the water by heating the chip on a hotplate at 180 degrees C for five minutes. When using a hotplate, be sure to put the chip on an area that is clear of hard-baked photoresist and other crap that inconsiderate cleanroom users have left for you. Also, be sure that in the unlikely event that you contaminate the hot plate, to clean it off with an appropriate solvent (generally acetone, or PGMEA if you are using LOR 3A). Only jerks ruin the cleanroom for other users, and you are not a jerk.

Empty the cleaning solvents into waster containers, found in the yellow cabinets. The TCE goes into a separate container in the toxics cabinet. The aceton and IPA go into the general solvent waste container. If no waste containers are available, find empty solvent bottle left for this purpose on the shelves near the sliding doors. Use a glass bottle for TCE waste. Always fill out the waste label properly: write the full name of the waste (Isopropyl alcohol, not IPA), check the right boxes (flamable for Acetone and IPA, Toxic/Poison and Flamable for TEC), write Marcus on the advisor line, Cleanroom for room. 6-5546 for the phone number. Don't fill in the date (that is to be filled in on the day the bottle is full). The DI water can go down the drain.

While you are cleaning the chip, set up the spinner. Only the Headway spinners are able to achieve repeatable results. It happens that upstairs, the right-hand spinner is a Headway, but it is also the spinner that is designated for epoxy, SU-8, and other thick, disgusting resists. Some types

of SU-8 resist can form a residue on the spinner (if not cleaned by the previous user) that will spin a voluminous spiderweb-like into the air when you use the spinner which lands on your chip, ruining it. However, since SU-8 is just as frequently used on the left-hand spinner (even though it is forbidden), you are better off using the Headway. To prevent contamination, line the spinner tray with foil. Make a tidy hold for the spindle so the foil does not rub any moving parts.

Next, select a chuck to hold your chip. For chips less than 5mm squre, the best chuck is the one with a single 1mm pillar in the middle with just one vacuum hole and no additional vacuum channels. The vacuum hole is there to hold the chip while it spins, so make sure it is clear of photoresist. Otherwise, the interlock will detect good vacuum, allow the spinner to start, and fling your chip at high speed into the spinner tray. If you need to clean the hole, use either a needle tool (which you carry just for such a purpose) and/or acetone (followed with an IPA rinse to avoide damaging the O-ring too much). Some photoresists are better removed with PGMEA. Blow the chuck dry, and firmly press onto the spindle.

Program the spinner. Press Recipe-0 (recipe 0 is the only recipe we are allowed to edit, the others are set to a fixed program). Press Step-1. Press Speed, then type 5000-enter to set the spin rate in RPM. Press Speed again, choose 5000-enter to set the ramp rate in RPM/sec. Press StepTerminate and type 45-enter to set the spin time. Press Step-2, StepTerminate, 0-enter: the recipe ends at the first 0-time step. Press Step-0 to end the programming sequence and return to run-mode.

Always spin a junk-chip. Balance the chip on the chuck. This is often easier if you turn on the vacuum by pressing the VacuumOnAuto button to toggle the vacuum ON (Don't leave vacuum on for highly extended periods, it isn't that great for the pump). Center the chip carefully, rotating the chuck by hand to be sure. Toggle vacuum back to Auto. Press the green foot-switch to start the spinner. Check the speed on the display, and make sure the chip dosn't fly away. After the spin cycle ends, inspect the chip to make sure the spin-cycle didn't contaminate the surface.

After your chip is done drying for 5 minutes, put it on the spinner and spin if for 45 seconds. This will enusre it is cool, and that it dosn't fly away. If it does fly away, you'll need to clean it again. But first check the back for bumps that prevent a good vacuum and try to get it to work. If the spinner refuses to work, it is probably clogged with photoresist or may need to have the interlock adjusted...seek professional assistance (or jam a clothes hanger down the hole to clear it). Never dump solvents down the vacuum hole.

Find Shipley 1813 in the yellow cabinet. Pour a little into a fluoroware beaker. Prepare a little aluminum foil mat with one end folded enough times to form a little ridge. The idea is to be able to lay the dropper on the ridge so that the tip hovers above the foil mat (without touching it) but no so high that all the liquid rushes to the bulb. Get a dropper and fill it with enough liquid to spin. Avoid air bubbles by allowing the bulb to fully fill before pulling the tip out of the liquid.

With the chip on the chuck and your foot poised above the green switch, drip a few drops of photoresist into the spinner pan to clear away phantom dust, and to make sure no air bubbles are near the tip. With the tip near the chip surface (to avoide excess air bubbles and turbulance) drip JUST enough liquid to cover the chip surface (on drop, usually) and quickly start the spinner. Some people recommend applying the resist during a 5 second, 500 RPM pre-spin, but it is not necesary for our small chips and is likely to increase problems with bubbles.

When all your chips are finished spinning, bake them on the hotplate at 115 C for 2 minutes. If you are working with more than one chip, you can keep them clean, safe, and identifiable lining them up on a glass slide inside a covered glass petri dish. To time more than one chip, place the first chip on the hotplate and start the watch. Then place the other chips in a line. When the alarm sounds, remove them in the same order–it will take the same amound of time to remove them as

it took to place them, so they will all get the same bake time.

Dispose of any excess photoresist waste in a correctly labelled waste container. Throw the empty beaker into the covered trashcan.

If the photomask is not clean (you can assume it is not, unless you cleaned it), hold it over 1-2 wipes and squirt it with a strong jet of acetone. Blow it dry, then rinse/blow with IPA. It is very important to blow the mask completely dry. This should remove almost any dirt, but if it dosn't, ask the CNS staff about photomask cleaning products.

Move to the AB mask aligner. Raise the mask frame and make sure that the small squre chuck with a single vacuum hole is installed. If not, remove the chuck by pulling the hoses off the aligner and loosening the two screws on the sides. Install the correct chuck. Lower the mask frame and place a piece of glass (not your mask) agains the pegs. Turn on the mask vacuum. Hold in the leveler buton (on the aligner on the left-front of the aligner) and raise the cuck by turning the z-knob. If the knob rotates without raising the chuck, tighten the idiotically long screw on the side of the knob. If the knob won't turn, this rediculously long screw is probably hitting the edge–move the stage back with the x-micrometer dial until there is enough clearance. Incidentally, the top of the z-knob is supposed to slip when the pressure of the chip/chuck against the mask is appropriate, and this slip-tension can be adjusted by the screw in the top on the knob (hidden under a plastic cap). Unfortunately, people often adjust this tension (often, I think people mistakenly radically overtighten the tension screw when they really wanted to tighten the rediculously long screw) so this feature cannot be relied upon. Continue raising the chuck and holding the level button until the top of the chuck is pressed into the glass and has been leveled by it. Release the level button and lower the chuck.

Replace the glass with your mask. Check that all the micrometers are apromimately centered so you have maximum adjustment capability in both directions. The chromimum-side (brown looking side) of the mask should be face-down. Put the chip in the center of the chuck in the desired orientation, squarely aligned with the mask as much as possible. Lower the mask (it shouldn't touch the chip yet). Look through the mask and move the chip into place with the x and y micrometer screws, (in front and on the right) and rotate the chip with the angle micrometer (on the left). Switch on the sample-vacuum.

Move the alignment microscope (use the "align" switch) above the mask. Use the lowest magnification to start. Use the lowest light level to minimize unwanted exposure. The two buttons on the microscope movement handle can be pressed to move the scope in the x or y direction. Focus on the mask and raise the chip enough that it is ALMOST in focus. You don't want the chip to touch the mask until you have finished aligning. When ready, slowly raise the chip into the mask. In fact, the first part of the chip to touch the mask will be the "corner beads," the thicker bumps of photoresist that form in the corners of the chip. If the chips moves or rotates due to edgebeads, then lower the chip slightly and realign. Holding in the level-button (to allow the chip to self-adjust for uneven corner bead heights) raise the mask until the shadows of the mesas disappear (ie, until the mask is touching the photoresist). Switch to the next-higher magnification, focus on the mask. As you raise the chip, the mask will be pushed up and out of focus. You want to get the contact between the chip and mask as close as possible without popping the mask vacuum (or breaking the chip or mask), or else light will leak around the patterns and cause an overexposure.

Send the alignment microscope back to the right. Make sure the "On' and "Auto" buttons are pressed on the exposre control (to the left), and set the time to 4 seconds. Since the auto button is pressed, when you flip the switch (on the right) to move the exposure unit into position, it will atuomatically turn on the lightsource when it is in place. Other than checking to ensure that the

light switches itself on, don't stare at the light during the exposure: the system is supposed to be safe, but look at it–there is no way all the UV is contained correctly. After the light switches off (you can hear the switch), flip the switch to move the lightsource out of the way.

Lower the chuck to make sure the chip is not stuck to the mask, raise the mask, remove the chip. Fill 2 labeled fluoroware beakers about 1/2 full with CD-26 developer. Fill the DI Water beaker with DI water. Swirl the chip in the first CD-26 for 20 seconds, quickly switch to the second beaker for 25 more seconds, then rinse in DI for 15 seconds. Blow the chip off. Inspect the results under a microscope.

There will be invisible redidual photoresist on the surface of the chip. This must be removed with UV-Ozone. Place the chip in the Uv-Ozone machine. Close the lid. Open both valves on the oxygen cylinder under the table. The main valve is tricky–make sure you have opened it at least a few turns. Set the time to 30 seconds. Don't use heat. Turn on the main power, the UV, the Ozone. Make sure the vent is closed (button not pressed) and hit start. Make sure there the flow indicator bead is floating near the top of the scale. Afterwards, vent the chamber for a minute or two, unless you like inhaling ozone and getting asthma. The chip is now ready to etch.

B.4 Etch Procedure

B.4.1 Summary

- DI Water:Sulfuric Acid:Hydrogen Peroxide 240:1:8 (approx. rate 3-5 nm/sec)
- Measure photoresist thickness
- Etch
- Measure photoresist + trench
- Remove photoresist with acetone + ultrasound
- Measure actual trench depth for future reference

B.4.2 Details

Gather materials

Get the hydrogen peroxide bottle out of the small fridge in the Westervelt sample prep room. If the door is locked, it is possible to break into the room by removing the ventilation grating with a screwdriver. Also take a calculator, a few glass pipets and bulbs from the sample prep room. It may be wise to take an empty glass bottle for waste; the cleanroom does not reliably provide clean empty bottles. Proceed to the downstairs cleanroom. In the gowning area you will find a red Marcus toolbox with glass beakers, take it in with you.

Mix the solution

Use the large graduated cylinder to measure 240 ml of DI water from the filter on the back wall (the DI water in the fume hood downstairs is not to be trusted).

Make sure an appropriate waste bottle is available and ready. Empty solvent bottles are not appropriate, as solvents will explode when mixed with acid. Have a fluoroware beaker full of DI water avialable. Use a pipet to suck 1 ml of sulfuric acid directly out of the bottle and measure it

into the small graduated cylinder. Empty any excess acid out of the pipet into the waste container, and rinse the pipet a few times with the clean DI water from your nearby beaker. Dispose of the pipet in the sharps waste, not the trash (otherwise an innocent person is likely to be stabbed while handling the trash). Add the acid to the mixture, and mix well. The acid is added before the H_2O_2 so that the heat liberated by the reaction does not degrate the H_2O_2. Finally, use a pipet to measure H_2O_2 into the mixture, and stir well. Clean all the measurement tools with everything with DI water, ensuring that all chemicals end up in waste containers, and finishing the job by rinsing well with DI water in the sink. Allow the etch solution to "sit and equilibrate" while you measure the thickness of the photoresist.

B.4.3 Profilometer Operation

Log into the profilometer computer (user:PBC pass:wismad). Start the profilometer software. Place a chip on the sample holder. Click the "view sample" button (the screen will be black, since the camera is still raised). Click the button to lower the tower. As the tower descends, use the x- and y- translation knobs to position the chip: when the tip lands, it must hit your chip, not the sample holder in order to correctly calibrate the tip height. The tip should not damage photoresist or GaAs, but if you are paranoid, use a junkchip. Meanwhile, NEVER move the sample when the tip is down, as it could damage the profilometer.

After the tower lowers and the tip hits your sample, the tip will automatically raise slightly. Use the two rings on the camera to adjust the zoom and focus. Generally, maximum zoom is appropriate for our devices. Use the lightbulb icons to adjust the light level. After setting the zoom, click the "tip down" button. Right-click the point where the tip hits its shadow, and choose to adjust the crosshair calibration. This readjusted crosshair is your best guide for positioning the scan.

Since the tip is not touching the sample, use the knobs to move the feature you want to measure to a position about 2-3 crosshair divisions to the right of your calibrated crosshair. The scan will move from left to right, starting at the crosshair (on the screen). Physically, this is from front to back on your sample. Rotate the stage to get the correct angle. Generally, it is best to start and end the scan on a surface that is known to be level (like the surface of the chip) and arrange for a bump (a narrowish region of photoresist) to be in the middle of the scan. This allows you to confidently level the scan on the two side regions.

Before starting the scan, click the "recipe set up" button. Choose a scan length (100-200 microns), a scan time (30-60s), and a tip force (10 mg). Click the "view Sample" button, and when ready, click the "start scan" button.

The profilometer violently drags the tip to the left (front), then starts again slowly to the right (back). When the tip returns to the starting position, it begins taking data, as shown on the screen. The violent action of the tip at the start of a scan can sometimes move the chip. If this happens, try sandwiching your chip between microscope slides in front and in back to add weight. It is also possible to reduce the tip force, although too little force may result in excessively noisy data.

After the scan, the screen switches to view the data. Drag the cursors to two spots (ideally as far away from each other as possible to maximize the lever arm) that should be level, and click the level button. The trace will be adjusted. Drag the cursors to the two levels you wish to measure, and pull them out to get regions to average over. The height difference between the cursor and the average height difference between the regions is indicated in the box on the left. Switch back to the sample view and repeat the scan as often as necessary to convince yourself it is accurate.

Incidentally, there will be variations in photoresist height across the chip, but the etch rate is typically uniform across the chip. Therefore, the most accurate mesa-height can be achieved by carefully measuring the same place (or places) on the chip.

When you have finished measuring, use the knobs to move the chip out from under the tip. When the chip is well clear of the tip, use a tweezers to remove it from the stage. Never try to pull a chip out from under the tip with the tweezers, due to the risk of hitting the tip [2].

Etch the chip

A typical etch rate is 3 nm/s. The etch-depth target should be set to remove all the dopants plus about 10%(if the sample is single-side doped: you do not have to etch all the way to the 2DEG, if the sample is double-side dope, you need to etch all the way to the under-side doping layer or you'll have leaky gates). The reason not to etch too far is that eventually you will have to evaporate continuous gates over the mesa edge, and you don't want to have to make them too thick because liftoff gets hard.

Calculate an etch time that should etch about half way to the target. That gives enough time to calculate the etch rate but does not risk going way to far (the etch rate shouldn't be 6 nm/s). Use the profilometer to measure the depth, calculate the etch rate, and iterate towards the target. It should be possible to hit the target within 5%.

Occasionally some materials will have some oxide or something on the surface that takes a long time to etch. Be patient, cowboy. Once the oxide is gone the etch rate goes back to the expected rate; you don't want to etch all the way to China just to get through the oxide with fewer profliometer iterations.

Remove the photoresist

When the profilometer tells you that you have hit the target, remove the photoresist with a little acetone. Measure the actual trench depth without the photoresist; you'll need that number to set the target evaporation thickness for the gates that connect the pads to the e-beam layer. That target is the trench depth plus 10%.

B.5 The rest

We have covered the use of all the tools now (except the Raith, see Appendix A). To finish the chip:

- Spin on a single-layer PMMA coating downstairs
- Pattern the small-gates with the Raith using the 20 µm aperture except for really tiny features. Use a step size of 10 nm. Be sure to burn a spot to focus, or nothing will be repeatable. I no longer use focus correction, I think it is defective. Instead, burn a spot near all your critical patterns.
- Develop for 1 minute in the 3:1 solution, rinse in IPA for 15 seconds.
- Clean the residual goop with Douwe's UV-Ozone machine in the sample prep room for 2 minutes.

[2] On the other hand, some may advocate raising the tower before removing the chip each time. However, I say this time-wasting paranoia has no place in a safe and efficient fabrication procedure

- Evaporate 5 nm Cr, 15 nm Au in the thermal evaporator
- Liftoff in acetone, overnight if you like your chip. Be brave, use 5 seconds of ultrasound to finish off the liftoff.
- Spin on triple-layer PMMA coating downstairs
- Pattern the large gate pads with the Raith using the 120 µm aperture. Use a step size of 100 nm. Don't bother to burn a spot to focus: it won't matter with this aperture.
- Develop in 3:1 solution for 90 sec. Do the 2 minute UV-Ozone.
- Evaporate 15 nm Cr and x nm of Au, where x is the mesa height + 10%.
- Liftoff overnight in acetone. This is the liftoff step that is most likely to fail (as could have been predicted by Murphy's law).
- DONE!

Appendix C
Complete Nanofabrication Recipe for 5/2 Devices

In this Appendix I list the complete nanofabrication recipe I developed to process the ultra-high mobility wafers for the 5/2 experiment. In fact, this recipe is only a small tweak to the standard Marcus lab recipe that has been developed and improved by many group members over many years.

We had two general difficulties in processing these wafers. The first difficulty was making ohmic contacts. I think the problem was that the doping in the ultra-high mobility wafers is designed to such tight tolerances that there is not much room for error in the ohmic-contact doping. The ohmic contact recipe in this Appendix routinely yields contacts with 50 Ω or less resistance. I think one important improvement over previous Marcus lab ohmic recipes is that the Ge and Au are evaporated separately. Trying to evaporate a eutectic alloy is just *asking* for trouble. Another improvement is the thickness of the metal. This makes the ohmics a pain to evaporate, but not as much of a pain as cooling ohmics that do not work.

The second difficulty was that the mobility of the samples was degrading by about 1 or 2 million m^2/Vs during the fabrication. That was a small percent change in mobility, but it was enough to degrade the 5/2 features. We traced the problem to the solvents used for liftoff in the LOR photoresist process. My first attempt at a solution was to switch to another photolithography process (AZ-5200E) that used acetone as the liftoff solvent, but I found the process to be unstable (although may be it is not more unstable than the Marcus lab standard LOR 3A recipe...somebody should look in to the AZ process more carefully someday). The solution I went with in the end was to use multilayer PMMA, patterned with e-beam lithography.

C.1 $5/2$-ready fab recipe

C.1.1 Mesas

Photo

1. 4-solvent clean (TCE, Acetone, IPA, DI-water 5′ each in ultrasound)
2. Bake dry 180°C, 5′
3. Spin on S1813 photoresist. No 5s slow spin. 5000rpm 45s. 1s spin up and spin down.
4. Bake 115°C, 2min.
5. Expose 4s.
6. Develop CD-26, 45s. Rinse DI 15s.
7. UV-Ozone (in upstairs cleanroom) 30s. Do not use plasma.

Etch

8. Etch in 240:8:1 H_2O:H_2SO_4:H_2O_2. Rinse in DI-water for 15s for each etch. Etch rate is approx. 3nm/sec. Target depth is 330nm, the depth of the second doping layer + 10%.
9. Remove photoresist with acetone.

C.1.2 Ohmics

Spin

1. 4-solvent clean
2. Bake dry 5′ 180°C
3. Spin on 3-layer PMMA. No 5s spin-up. 4000rpm, 45sec, 1sec spin-up and spin-down. First layer: 495 PMMA C6, 5′ bake at 180°C. Second layer:495 PMMA C6, 7′ bake at 180°C. Third layer:950 PMMA A4, 10′ bake at 180°C. (The multilayer is for undercut and to get the PMMA thick enough for liftoff.)

Pattern

4. Pattern on Raith using 120µm aperture.
5. Develop in 3:1 IPA:MIBK for 1min30sec. Rinse IPA 15sec.
6. 2 min UV-Ozone in the Douwe box.

Evaporate

7. Ammonium hydroxide dip, 3 seconds full strength. Rinse DI-water 15 sec.
8. Get into E-beam evaporator as quickly as possible. Don't trip.

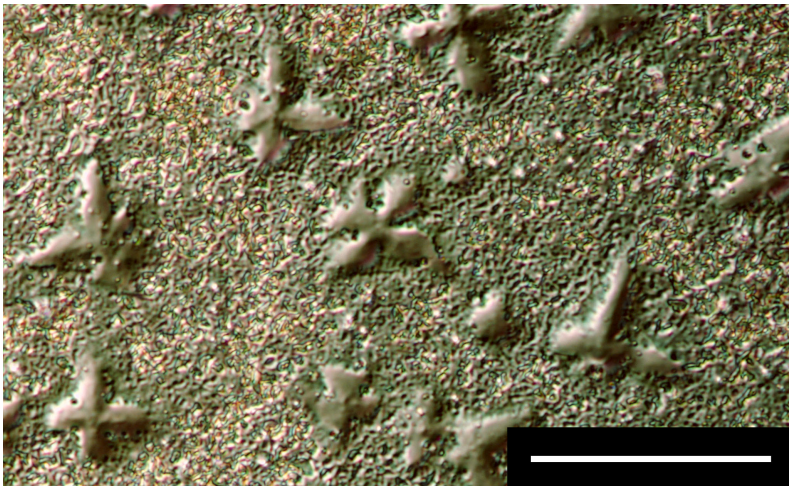

Figure C.1: An optical micrograph of an annealed ohmic that was measured to have less than 50 Ω resistance at 4 K. The white scale bar is 50 µm. Annealed ohmics that exhibit these cross-like structures are virtually guaranteed to have very low resistance.

9. Evaporate the metal stack. The wait times are important to keep things from getting too hot. For 100nm deep 2DEG, the final three layers can be omitted. For 200nm deep 2DEG, the final three layers have been shown to decrease the ohmic resistance. The thicknesses given are the actual target thickness. Multiply by 1.25 for the target in the Marcus lab e-beam evaporator. A reasonable evaporation rate is about .25-.3nm/sec
   Pt: 5nm
   Au: 200nm
   WAIT at least 30 min
   Ge: 100nm
   Pt: 73nm
   WAIT at least 30 min
   Au: 100nm
   Ge: 50nm
   Pt: 55nm

10. Liftoff in acetone. Usually takes 30 seconds.

Anneal

11. Use the Jipelec RTA in the cleanroom. Pyrometer control, target 530°C, 100s. (Reduce time for shallower 2DEG).

C.1.3 Small gates

Spin

1. 4-solvent clean.
2. 5 min bake 180°C
3. Spin on PMMA. No 5s spin-up. 4000rpm, 45sec, 1sec. spin-up and spin-down. 950 PMMA A4.
4. 10′ bake at 180°C.

Pattern

5. Write the small gates using 20µmaperture on the Raith.
6. Develop 1 min in 3:1, 15 s IPA rinse.
7. 2 min UV-Ozone in the Douwe box.

Evaporate

8. Use thermal evaporator. 5nm Cr, 15nm Au.
9. Liftoff in Acetone, overnight. 5 sec ultrasound.

C.1.4 Connector gates

Spin

1. 4-solvent clean
2. Bake dry 5' 180°C
3. Spin on 3-layer PMMA. No 5s spin-up. 4000rpm, 45sec, 1sec spin-up and spin-down. First layer: 495 PMMA C6, 5' bake at 180°C. Second layer:495 PMMA C6, 7' bake at 180°C. Third layer:950 PMMA A4, 10' bake at 180°C. (The multilayer is for undercut and to get the PMMA thick enough for liftoff.)

Pattern

4. Pattern on Raith using 120µm aperture.
5. Develop in 3:1 IPA:MIBK for 1min30sec. Rinse IPA 15sec.

Evaporate

6. Use thermal evaporator.
7. The target thickness is the depth of the mesa etch plus 10%.
8. Liftoff in Acetone.
9. DONE!

Appendix D
Wafer Data Sheet

This appendix contains a copy of the wafer data sheet provided by Loren Pfeiffer for the material we used in the experiments reported in Chapter 7. This is the one material we have found so far with good features at $\nu = 5/2$ and decent gateability.

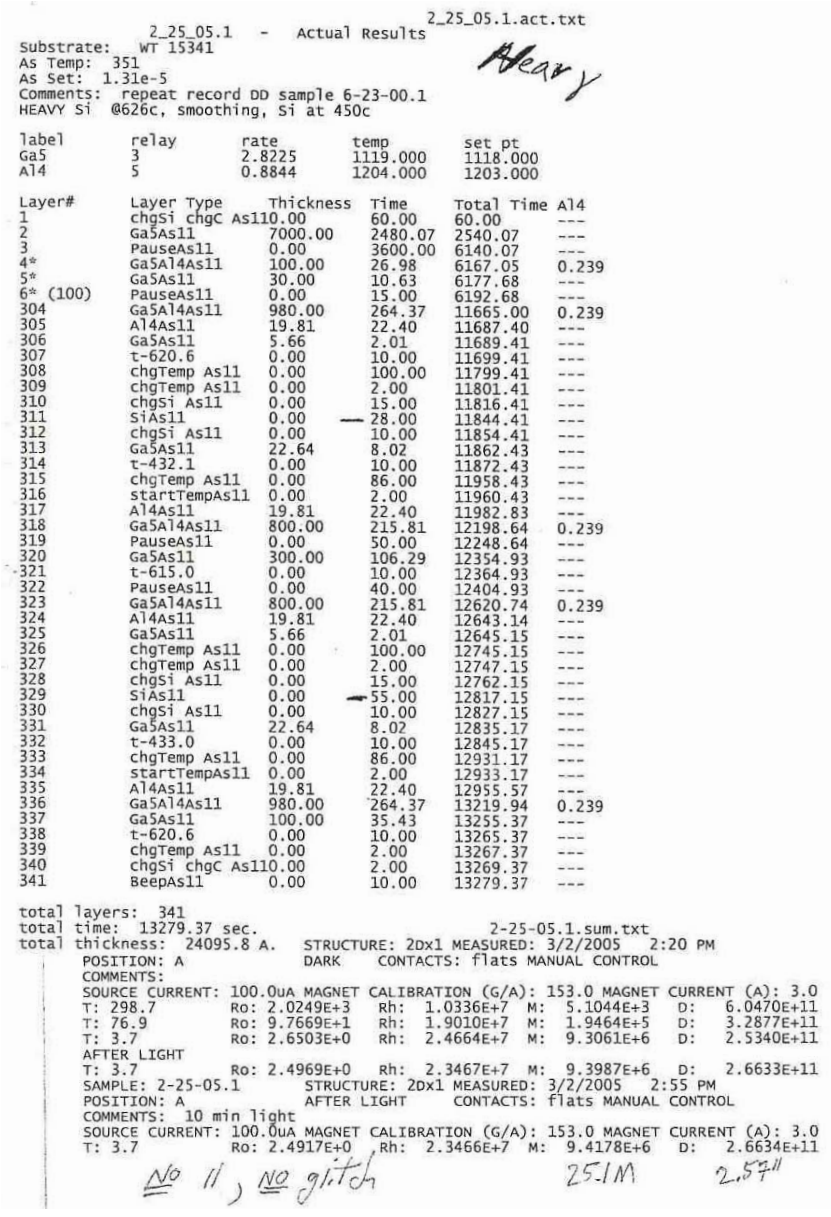

2_25_05.1.act.txt

2_25_05.1 - Actual Results

Substrate: WT 15341
As Temp: 351
As Set: 1.31e-5
Comments: repeat record DD sample 6-23-00.1
HEAVY Si @626c, smoothing, Si at 450c

Heavy

label	relay	rate	temp	set pt
Ga5	3	2.8225	1119.000	1118.000
Al4	5	0.8844	1204.000	1203.000

Layer#	Layer Type	Thickness	Time	Total Time	Al4
1	chgSi chgC As11	0.00	60.00	60.00	---
2	GaSAs11	7000.00	2480.07	2540.07	---
3	PauseAs11	0.00	3600.00	6140.07	---
4*	GaSAl4As11	100.00	26.98	6167.05	0.239
5*	GaSAs11	30.00	10.63	6177.68	---
6* (100)	PauseAs11	0.00	15.00	6192.68	---
304	GaSAl4As11	980.00	264.37	11665.00	0.239
305	Al4As11	19.81	22.40	11687.40	---
306	GaSAs11	5.66	2.01	11689.41	---
307	t-620.6	0.00	10.00	11699.41	---
308	chgTemp As11	0.00	100.00	11799.41	---
309	chgTemp As11	0.00	2.00	11801.41	---
310	chgSi As11	0.00	15.00	11816.41	---
311	SiAs11	0.00	28.00	11844.41	---
312	chgSi As11	0.00	10.00	11854.41	---
313	GaSAs11	22.64	8.02	11862.43	---
314	t-432.1	0.00	10.00	11872.43	---
315	chgTemp As11	0.00	86.00	11958.43	---
316	startTempAs11	0.00	2.00	11960.43	---
317	Al4As11	19.81	22.40	11982.83	---
318	GaSAl4As11	800.00	215.81	12198.64	0.239
319	PauseAs11	0.00	50.00	12248.64	---
320	GaSAs11	300.00	106.29	12354.93	---
321	t-615.0	0.00	10.00	12364.93	---
322	PauseAs11	0.00	40.00	12404.93	---
323	GaSAl4As11	800.00	215.81	12620.74	0.239
324	Al4As11	19.81	22.40	12643.14	---
325	GaSAs11	5.66	2.01	12645.15	---
326	chgTemp As11	0.00	100.00	12745.15	---
327	chgTemp As11	0.00	2.00	12747.15	---
328	chgSi As11	0.00	15.00	12762.15	---
329	SiAs11	0.00	55.00	12817.15	---
330	chgSi As11	0.00	10.00	12827.15	---
331	GaSAs11	22.64	8.02	12835.17	---
332	t-433.0	0.00	10.00	12845.17	---
333	chgTemp As11	0.00	86.00	12931.17	---
334	startTempAs11	0.00	2.00	12933.17	---
335	Al4As11	19.81	22.40	12955.57	---
336	GaSAl4As11	980.00	264.37	13219.94	0.239
337	GaSAs11	100.00	35.43	13255.37	---
338	t-620.6	0.00	10.00	13265.37	---
339	chgTemp As11	0.00	2.00	13267.37	---
340	chgSi chgC As11	0.00	2.00	13269.37	---
341	BeepAs11	0.00	10.00	13279.37	---

total layers: 341
total time: 13279.37 sec.
total thickness: 24095.8 A.

2-25-05.1.sum.txt

STRUCTURE: 2Dx1 MEASURED: 3/2/2005 2:20 PM
POSITION: A DARK CONTACTS: flats MANUAL CONTROL
COMMENTS:
SOURCE CURRENT: 100.0uA MAGNET CALIBRATION (G/A): 153.0 MAGNET CURRENT (A): 3.0
T: 298.7 Ro: 2.0249E+3 Rh: 1.0336E+7 M: 5.1044E+3 D: 6.0470E+11
T: 76.9 Ro: 9.7669E+1 Rh: 1.9010E+7 M: 1.9464E+5 D: 3.2877E+11
T: 3.7 Ro: 2.6503E+0 Rh: 2.4664E+7 M: 9.3061E+6 D: 2.5340E+11
AFTER LIGHT
T: 3.7 Ro: 2.4969E+0 Rh: 2.3467E+7 M: 9.3987E+6 D: 2.6633E+11
SAMPLE: 2-25-05.1 STRUCTURE: 2Dx1 MEASURED: 3/2/2005 2:55 PM
POSITION: A AFTER LIGHT CONTACTS: flats MANUAL CONTROL
COMMENTS: 10 min light
SOURCE CURRENT: 100.0uA MAGNET CALIBRATION (G/A): 153.0 MAGNET CURRENT (A): 3.0
T: 3.7 Ro: 2.4917E+0 Rh: 2.3466E+7 M: 9.4178E+6 D: 2.6634E+11

No 11, No glitch 25.1M 2.57M

Appendix E
Antilocalization Fitting Routines

This appendix contains the full listing of the routines we used to fit the data in the 2D spin-orbit coupling paper (Chapter 4). This listing is a C program I wrote that generates a detailed 2D matrix of values for the Cooperon function in Equation 4.2. The Cooperon function is the sum of the sum of two integrals, none of which converge very fast. By calculating all possible values once, we were actually able to do data fitting.

```
/*  XFUNC1.c -- This is the procedure used for calculating the "Yuli
    C" function, the cooperon for
                weak localization/antilocalization including Spin
                    Orbit.

*/

#include "XOPStandardHeaders.h"          // Include ANSI headers, Mac
    headers, IgorXOP.h, XOP.h and XOPSupport.h
#include "XFUNC1.h"
#include <stdio.h>
#include <stdlib.h>
#include <math.h>

/* All structures are 2-byte-aligned. */
#if GENERATINGPOWERPC
    #pragma options align=mac68k
#endif
#ifdef _WINDOWS_
    #pragma pack(2)
#endif


//FILE *fp;      //File can be used for diagnostic purposes to write
   output.

/* error function in double precision */
double derf(double x)
{
    // Downloaded from http://momonga.t.u-tokyo.ac.jp/~ooura/gamerf.
       html
    // Searched for Algorithm on http://www.mathtools.net/C++/
       Mathematics/
    int k;
    double w, t, y;
    static double a[65] = {
        5.958930743e-11, -1.13739022964e-9,
        1.466005199839e-8, -1.635035446196e-7,
        1.6461004480962e-6, -1.492559551950604e-5,
        1.2055331122299265e-4, -8.548326981129666e-4,
```

```
    0.00522397762482322257, -0.026866170645077342,
    0.11283791670954881569, -0.37612638903183748117,
    1.12837916709551257377,
    2.372510631e-11, -4.5493253732e-10,
    5.90362766598e-9, -6.642090827576e-8,
    6.7595634268133e-7, -6.21188515924e-6,
    5.10388300970969e-5, -3.7015410692956173e-4,
    0.00233307631218880978, -0.012549884771821922 1,
    0.05657061146827041994, -0.2137966477645600658,
    0.84270079294971486929,
    9.49905026e-12, -1.8310229805e-10,
    2.39463074e-9, -2.721444369609e-8,
    2.8045522331686e-7, -2.61830022482897e-6,
    2.195455056768781e-5, -1.6358986921372656e-4,
    0.00107052153564110318, -0.0060828471811359015 1,
    0.02986978465246258244, -0.13055593046562267625,
    0.67493323603965504676,
    3.82722073e-12, -7.421598602e-11,
    9.793057408e-10, -1.126008898854e-8,
    1.1775134830784e-7, -1.1199275838265e-6,
    9.62023443095201e-6, -7.404402135070773e-5,
    5.0689993654144881e-4, -0.00307553051439272889,
    0.01668977892553165586, -0.08548534594781312114,
    0.56909076642393639985,
    1.55296588e-12, -3.032205868e-11,
    4.0424830707e-10, -4.71135111493e-9,
    5.011915876293e-8, -4.8722516178974e-7,
    4.30683284629395e-6, -3.445026145385764e-5,
    2.4879276133931664e-4, -0.00162940941748079288,
    0.00988786373932350462, -0.05962426839442303805,
    0.49766113250947636708
};
static double b[65] = {
    -2.9734388465e-10, 2.69776334046e-9,
    -6.40788827665e-9, -1.6678201321e-8,
    -2.1854388148686e-7, 2.66246030457984e-6,
    1.612722157047886e-5, -2.5616361025506629e-4,
    1.5380842432375365e-4, 0.00815533022524927908,
    -0.01402283663896319337, -0.19746892495383021487,
    0.71511720328842845913,
    -1.951073787e-11, -3.2302692214e-10,
    5.22461866919e-9, 3.42940918551e-9,
    -3.5772874310272e-7, 1.9999935792654e-7,
    2.687044575042908e-5, -1.1843240273775776e-4,
    -8.0991728956032271e-4, 0.00661062970502241174,
    0.00909530922354827295, -0.2016007277849101314,
    0.51169696718727644908,
    3.147682272e-11, -4.8465972408e-10,
    6.3675740242e-10, 3.377623323271e-8,
    -1.5451139637086e-7, -2.03340624738438e-6,
    1.947204525295057e-5, 2.854147231653228e-5,
    -0.00101565063152200272, 0.00271187003520095655,
    0.02328095035422810727, -0.16725021123116877197,
    0.32490054966649436974,
```

```
            2.31936337e-11, -6.303206648e-11,
            -2.64888267434e-9, 2.050708040581e-8,
            1.1371857327578e-7, -2.11211337219663e-6,
            3.68797328322935e-6, 9.823686253424796e-5,
            -6.5860243990455368e-4, -7.5285814895230877e-4,
            0.02585434424202960464, -0.11637092784486193258,
            0.18267336775296612024,
            -3.67789363e-12, 2.0876046746e-10,
            -1.93319027226e-9, -4.35953392472e-9,
            1.8006992266137e-7, -7.8441223763969e-7,
            -6.75407647949153e-6, 8.428418334440096e-5,
            -1.7604388937031815e-4, -0.0023972961143507161,
            0.0206412902387602297, -0.06905562880005864105,
            0.09084526782065478489
        };

        w = x < 0 ? -x : x;
        if (w < 2.2) {
            t = w * w;
            k = (int) t;
            t -= k;
            k *= 13;
            y = ((((((((((a[k] * t + a[k + 1]) * t +
                a[k + 2]) * t + a[k + 3]) * t + a[k + 4]) * t +
                a[k + 5]) * t + a[k + 6]) * t + a[k + 7]) * t +
                a[k + 8]) * t + a[k + 9]) * t + a[k + 10]) * t +
                a[k + 11]) * t + a[k + 12]) * w;
        } else if (w < 6.9) {
            k = (int) w;
            t = w - k;
            k = 13 * (k - 2);
            y = ((((((((((b[k] * t + b[k + 1]) * t +
                b[k + 2]) * t + b[k + 3]) * t + b[k + 4]) * t +
                b[k + 5]) * t + b[k + 6]) * t + b[k + 7]) * t +
                b[k + 8]) * t + b[k + 9]) * t + b[k + 10]) * t +
                b[k + 11]) * t + b[k + 12];
            y *= y;
            y *= y;
            y *= y;
            y = 1 - y * y;
        } else {
            y = 1;
        }
        return x < 0 ? -y : y;
    }


    static double Laguerre(int n, double x)
    {   //This is the Laguerre Polynomial as in Arfken p. 779
        double *L;
        int j = 1;
        double jj = 1.0;
        double Lag;
        if (n == 0) return(1.0);
```

```
    if (n == 1) return(-x+1.0);
    L = (double *)malloc( (size_t) (n+5)*sizeof(double));
    *L = 1.0;
    L += 1;
    *(L) = -x+1.0;
    do
    {
        *(L+1) = *L*2 - *(L-1) - ( *L*(1+x) - *(L-1) )/(jj+1.0);
        jj += 1.0;
        L += 1;
    }
    while(jj < n);
    Lag = *L;
    free (L-n);
    return(Lag);
}

static double aLaguerre(int n, double m, double x)
{   //This is the Associated Laguerre Polynomial as in Arfken p. 780
    double *L;
    int j = 1;
    double jj = 1.0;
    double Lag;
    if (n == 0) return(1.0);
    if (n == 1) return(-x+1.0);
    L = (double *)malloc( (size_t) (n+5)*sizeof(double));
    *L = 1.0;
    L += 1;
    *(L) = -x+m+1.0;
    do
    {
        *(L+1) = *L*(2*jj+m+1-x)/(jj+1) - *(L-1)*(jj+m)/(jj+1);
        jj += 1.0;
        L += 1;
    }
    while(jj < n);
    Lag = *L;
    free (L-n);
    return(Lag);
}

static double Pn(double s, int n, double f, double binSize)
{  //This procedure integrates the curve as described in Pn
    //binSize is the x-size of the trapezoids for integration
    double b;
    double c = Laguerre(n,0.0);
    double i=1.0;
    double Sum=0;
    double t;
    double t2;
    double nSmall = 0;
    double SMALL = 1e-25; //1e-50;
    double ce;
    do
```

```
    {
        b=c;
        t = binSize*i;
        t2 = t*t;
        ce = exp(-s*f*t-t2/2);
        c= ce*Laguerre(n,t2);
        if ((fabs(c)) < SMALL || ce < 1e-150 ) nSmall++;    //We are
            looking for enough small numbers in a row to quit.
        else nSmall=0;
        Sum += binSize/2*(c+b);  //Add the area of the new trapezoid
            to the overall integral
        i++;
    }
    while ((nSmall < 6) ); //Quit if we find 5 small numbers in a
        row.
    return (s*Sum);
}

static double Poo(double x, double f, double binSize)
{   //This procedure return Po, either exactly (if erf < 1.0) or by
    numerical integration
    double A=sqrt(2/x)*f;
    double ErfResult = derf(A/sqrt(2));
    double Pint;
    double exact = ( -sqrt(2/x)*exp(0.5*A*A)*sqrt
        (3.14159265358979238/2)*(-1+ErfResult) );
    if (ErfResult >= .9999999999990 )
    {
        Pint = Pn(sqrt(2/x),0,f,binSize);
        return (Pint);
    }   else
    {
        return (exact);
    };
}

static double Pnm(double s, int n, double m, double f, double
    binSize)
{  //This procedure integrates the curve as described in Pnm
    //binSize is the x-size of the trapezoids for integration
    double b;
    double c = Laguerre(n,0.0);
    double i=1.0;
    double Sum=0;
    double t;
    double t2;
    double nSmall = 0;
    double SMALL = 1e-50;
    double ce;
    do
    {
        b=c;
        t = binSize*i;
        t2 = t*t;
```

```
        ce = exp(-s*f*t-t2/2);
        c = ce*aLaguerre(n,m,t2);
        if (fabs(c) < SMALL || ce < 1e-150) nSmall++;   //We are
            looking for enough small numbers in a row to quit.
        else nSmall=0;
        Sum += binSize/2*(c+b);  //Add the area of the new trapezoid
             to the overall integral
        i++;
//      printf("\n%f, nSmall=%f, t=%f, Sum=%f",i,nSmall,t,Sum);
    } while ((nSmall < 6) ); //Quit if we find 5 small numbers in a
        row.
    return ( s/sqrt(n+1.0) *Sum );
}

static double Dfunc(double x, double fi, double binSize,double
    QUALITY)
{
    double P;
    int n=0;
    double Sum=0;
    double Term;
    do
    {
        P = Pn( sqrt(2/fabs(x)),n,fi,binSize);
        Term = P*Pnm(sqrt(2/fabs(x)),n,1,fi,binSize)*Pnm(sqrt(2/fabs
            (x)),n,-1,fi,binSize)/2/(1-P);
        Sum += Term;
        n++;
//      if (n % 100 == 0) printf ("\nTerm=%e, n=%d, P=%e, Sum=%f",
    Term,n,P,Sum);
    } while (fabs(Term/Sum) > QUALITY);  //Keep adding terms until
        individual terms are QUALITY smaller than the sum.
    return (-x*Sum);
}

void Go(IORecHandle ioRecHandle)
{
    HOST_IMPORT void main(IORecHandle);
    main(ioRecHandle);
}

//The function YuliC returns the cooperon for a given x and f
static int
YuliC(
    struct {
        DOUBLE p4;
        DOUBLE p3;
        DOUBLE p2;
        DOUBLE p1;
        DOUBLE result;
    }* p)
{
    double x= p->p1;
    double fi= p->p2;
```

```
    double binSize = p->p3;
    double QUALITY = p->p4;
//START OF PROCEDURE FUNCTIONALITY
   -----------------------------------------------------------
    double P,Pa;
    long n=0;
    double Sum=0;
    double jj=1.0;
    double Term;
    double ss = sqrt(2/x);
    int flag=0;
    long maxn = 1000000;    //This is the maximum number of terms to
        include in the sum
//  fp = fopen("0906file.txt", "a+");
    {
        double *L;
        double *LL;
        double Po = Poo(x,fi,binSize);
        LL = (double *)malloc( (size_t) (maxn+5)*sizeof(double));
        L=LL;
        do
        {
            //CALCULATE P
            if (n == 0) {
                P=Po;
            };
            if (n == 1) {
                P=(fi*ss*ss - fi*fi*ss*ss*Po);
                if ((P > Po) || (fabs((Po-P)/Po) > .05)) {
                    flag = 1;
                    P = 1.0/sqrt(fi*fi+(2*n+1)*(2.0/ss/ss));
                };
            };
            if (n == 2)
            {
                double P1 = fi*ss*ss - fi*fi*ss*ss*Po;
                P= ( (1+fi*fi*ss*ss)*(Po-P1)/2.0 );
                if ( (P > P1) || (fabs((P1-P)/P1) > .05) ) {
                    flag = 2;
                    P = 1.0/sqrt(fi*fi+(2*n+1)*(2.0/ss/ss));
                };
            };
            if (n == 3)
            {
                *L = Po;    //n=-2
                L += 1;
                *(L) = fi*ss*ss - fi*fi*ss*ss*Po;   //n=-1
                *(L+1) = (1+fi*fi*ss*ss)*(Po-(*L))/2.0; //n=0
                *(L+2) = ((jj+1+fi*fi*ss*ss)*( (*L) - (*(L+1)) ) +
                   jj * (*(L-1)) )/(jj+2);
                jj += 1.0;
                L += 1;
                P = *(L+1);
```

```
                    if ( (*(L+1) > *(L)) || ( fabs((*(L+1) - *(L))/ *(L)
                        ) > .05) ) {  //The series of Pn MUST be
                        decreasing, or we get huge problems.  Switch to
                        symptotic as soon as this happens
                         flag = 3;
                         P = 1.0/sqrt(fi*fi+(2*n+1)*(2.0/ss/ss));
                    };
                };
                if ( (n > 3) && (flag==0))
                {
                    *(L+2) = ((jj+1+fi*fi*ss*ss)*( (*L) - (*(L+1)) ) +
                        jj * (*(L-1)) )/(jj+2);
                    jj += 1.0;
                    L += 1;
                    P = *(L+1);
                    Pa = 1.0/sqrt(fi*fi+(2*n+1)*(2.0/ss/ss));
                    if ( (*(L+1) > *(L)) || (fabs((*(L+1) - *(L))/ *(L))
                         > .05) ) {  //The series of Pn MUST be
                        decreasing, or we get huge problems.  Switch to
                        symptotic as soon as this happens
                         flag = n;
                         P = 1.0/sqrt(fi*fi+(2*n+1)*(2.0/ss/ss));
                    };
                };
                if (flag>0) P = 1.0/sqrt(fi*fi+(2*n+1)*(2.0/ss/ss));
                //DONE CALCULATING P
                Term = P*P*P/(1.0-P);
                Sum += Term;
                n++;
            } while ( (fabs(Term/Sum) > QUALITY) && (n < maxn));  //Keep
                adding terms until individual terms are QUALITY smaller
               than the sum.
            free (LL);
        }

//  fprintf(fp,"\tC(x=%f,f=%f)=\t%f",x,fi,x*Sum );
//  fprintf(fp,"\tPnINT(n=0)=\t%.16f\t%d\t%d\n",Pn(ss,0,fi,binSize),
    flag,n);
//  fclose(fp);
    p->result = x*Sum;
    return(0);                  /* XFunc error code */
}

static int
YuliD(
    struct {
        DOUBLE p4;
        DOUBLE p3;
        DOUBLE p2;
        DOUBLE p1;
        DOUBLE result;
    }* p)
{
    double x = p->p1;
```

```
    double fi = p->p2;
    double binSize= p->p3;
    double QUALITY= p->p4;
    double P;
    int n=0;
    double Sum=0;
    double Term;
    do
    {
        P = Pn( sqrt(2/fabs(x)),n,fi,binSize);
        Term = P*Pnm(sqrt(2/fabs(x)),n,1,fi,binSize)*Pnm(sqrt(2/fabs
            (x)),n,-1,fi,binSize)/2/(1-P);
        Sum += Term;
        n++;
    } while ((fabs(Term/Sum) > QUALITY) && n < 2000);  //Keep adding
        terms until individual terms are QUALITY smaller than the
       sum.
    p->result = -x*Sum;
    return (0);
}

//The rest of the file is just the interface to Igor.
struct DPComplexNum {
    DOUBLE real;
    DOUBLE imag;
};

static int
XFUNC1ComplexConjugate(
    struct {
        struct DPComplexNum p1;          /* complex parameter */
        struct DPComplexNum result;      /* complex result */
    }* p)
{
    p->result.real = p->p1.real;
    p->result.imag = -p->p1.imag;
    return 0;
}

static long
RegisterFunction()
{
    int funcIndex;
    /*  NOTE:
        Some XOPs should return a result of NIL in response to the
           FUNCADDRS message.
        See XOP manual "Restrictions on Direct XFUNCs" section.
    */
    funcIndex = GetXOPItem(0);       /* which function invoked ? */
    switch (funcIndex) {
        case 0:                      /* XFUNC1Add(p1, p2) */
            return((long)YuliC);
            break;
        case 1:                      /* XFUNC1Div(p1, p2) */
```

```
            return((long)YuliD);
            break;
        case 2:                         /* XFUNC1ComplexConjugate(p1) */
            return((long)XFUNC1ComplexConjugate);
            break;
    }
    return(NIL);
}

/*  DoFunction()
    This will actually never be called because all of the functions
        use the direct method.
    It would be called if a function used the message method. See
        the XOP manual for
    a discussion of direct versus message XFUNCs.
*/
static int DoFunction()
{
    int funcIndex;
    void *p;                    /* pointer to structure containing
        function parameters and result */
    int err;

    funcIndex = GetXOPItem(0);      /* which function invoked ? */
    p = (void *)GetXOPItem(1);      /* get pointer to params/result
        */
    switch (funcIndex) {
        case 0:                     /* XFUNC1Add(p1, p2) */
            err = YuliC(p);
            break;
        case 1:                     /* XFUNC1Div(p1, p2) */
            err = YuliD(p);
            break;
        case 2:                     /* XFUNC1ComplexConjugate(p1) */
            err = XFUNC1ComplexConjugate(p);
            break;
    }
    return(err);
}

/*  XOPEntry()
    This is the entry point from the host application to the XOP for
        all messages after the
    INIT message.
*/

static void
XOPEntry(void)
{
    long result = 0;
    switch (GetXOPMessage()) {
        case FUNCTION:                                  /* our external
            function being invoked ? */
            result = DoFunction();
```

```
            break;
        case FUNCADDRS:
            result = RegisterFunction();
            break;
    }
    SetXOPResult(result);
}

/*  main(ioRecHandle)
    This is the initial entry point at which the host application
        calls XOP.
    The message sent by the host must be INIT.
    main() does any necessary initialization and then sets the
        XOPEntry field of the
    ioRecHandle to the address to be called for future messages.
*/

HOST_IMPORT void
main(ioRecHandle)
    IORecHandle ioRecHandle;
{
#ifdef applec                   /* for MPW C for 68K only */
    void _DATAINIT(void);
    _DATAINIT();                /* for MPW C only */
    UnloadSeg(_DATAINIT);
#endif

#ifdef XOP_GLOBALS_ARE_A4_BASED
    #ifdef __MWERKS__
        SetCurrentA4();                                 /* Set up
            correct A4. This allows globals to work. */
        SendXOPA4ToIgor(ioRecHandle, GetA4());          /* And
            communicate it to Igor. */
    #endif
#endif

    LoadXOPSegs();
    XOPInit(ioRecHandle);                           /* do standard
        XOP initialization */
    SetXOPEntry(XOPEntry);                          /* set entry
        point for future calls */

    if (igorVersion < 200)
        SetXOPResult(REQUIRES_IGOR_200);
    else
        SetXOPResult(0L);
}

#if GENERATINGPOWERPC
    #pragma options align=reset
#endif
#ifdef _WINDOWS_
    #pragma pack()
#endif
```

```
/* All structures are 2-byte-aligned */
```

Bibliography

[1] Sethna J., in L. Nagel and D. Stein, eds., *Order Parameters, Broken Symmetry, and Topology. 1991 Lectures in Complex Systems, Santa Fe Institute Studies in the Sciences of Complexity, Proceedings*, Addison-Wesley, New York (1992).

[2] Das Sarma S., Freedman M. and Nayak C., *Phys. Rev. Lett.* **94** 166802 (2005).

[3] Stern A. and Halperin B.I., *Phys. Rev. Lett.* **96** 016802 (2006).

[4] Bonderson P., Kitaev A. and Shtengel K., *Phys. Rev. Lett.* **96** 016803 (2006).

[5] Hou C.Y. and Chamon C., *Phys. Rev. Lett.* **97** 146802 (2006).

[6] Feldman D.E. and Kitaev A., *Phys. Rev. Lett.* **97** 186803 (2006).

[7] Kitaev A., *quant-ph/9707021* (2006).

[8] Duan L.M., Demler E. and Lukin M.D., *Phys. Rev. Lett.* **91** 090402 (2003).

[9] Das Sarma S., private communication (2005).

[10] Preskill J., http://www.theory.caltech.edu/ preskill/ph229/ (2004).

[11] BELL J.S., *Rev. Mod. Phys.* **38** 447 (1966).

[12] Garcia-Ripoll J.J., Zoller P. and Cirac J.I., *Phys. Rev. A (Atomic, Molecular, and Optical Physics)* **71** 062309 (2005).

[13] Dell'Anno F., De Siena S. and Illuminati F., *Physics Reports-Review Section Of Physics Letters* **428** 53 (2006).

[14] Mabuchi H. and Doherty A., *Science* **298** 1372 (2002).

[15] Schulman L. and Vazirani U.

[16] Loss D. and DiVincenzo D.P., *Phys. Rev. A* **57** 120 (1998).

[17] Taylor J.M. *et al.*, *Nature Physics* .

[18] Schmidt-Kaler F. *et al.*, *Nature* **422** 408 (2003).

[19] Leibfried D. *et al.*, *nature* **422** 412 (2003).

[20] Das R. and Kumar A., *Applied Physics Letters* **89** 024107 (2006).

[21] Ballentine L., World Scientific, New Jersey (1998).

[22] Wilczek F., *Phys. Rev. Lett.* **49** 957 (1982).

[23] Preskill J., http://www.theory.caltech.edu/ preskill/ph219/topological.pdf (2004).

[24] Störmer H.L., *Rev. Mod. Phys.* **71** 875 (1999).

[25] Das Sarma S., in S. Das Sarma and A. Pinczuk, eds., *Perspectives in Quantum Hall Effects*, Wiley, New York (1997).

[26] Abrahams E. *et al.*, *Phys. Rev. Lett.* **42** 673 (1979).

[27] Halperin B.I., *Phys. Rev. B* **25** 2185 (1982).

[28] Laughlin R.B., *Phys. Rev. B* **23** 5632 (1981).

[29] Wen X.G., *Phys. Rev. Lett.* **64** 2206 (1990).

[30] Datta S., ed., Cambridge University Press, Cambridge (2003).

[31] Shapere A. and Wilczek F., World Scientific, New Jersey (1989).

[32] Laughlin R.B., *Phys. Rev. Lett.* **50** 1395 (1983).

[33] Jain J., in S. Das Sarma and A. Pinczuk, eds., *Perspectives in Quantum Hall Effects*, Wiley, New York (1997).

[34] Arovas D., Schrieffer J.R. and Wilczek F., *Phys. Rev. Lett.* **53** 722 (1984).

[35] Goldman V.J. and Su B., *Science* **267** 1010 (1995).

[36] de C. Chamon C. *et al.*, *Phys. Rev. B* **55** 2331 (1997).

[37] I do not think Wilczek expected the anyon, which he considered essentially a toy mathematical object, to assume a physical form so soon after he published it. In the introduction of his anyon paper [22], using a strategy now rarely seen in PRL introductions, he stated that "practical applications of these phenomena seem remote." That was the only point in the paper that turned out to be incorrect.

[38] Arovas D.

[39] Jain J.K., *Phys. Rev. Lett.* **63** 199 (1989).

[40] Halperin B.I., Lee P.A. and Read N., *Phys. Rev. B* **47** 7312 (1993).

[41] Read N., *Bull. Am. Phys. Soc.* **32** 923 (1987).

[42] Read N., *Phys. Rev. Lett.* **62** 86 (1989).

[43] Zhang S.C., Hansson T.H. and Kivelson S., *Phys. Rev. Lett.* **62** 82 (1989).

[44] Zhang S. (1992).

[45] Willett R. *et al.*, *Phys. Rev. Lett.* **59** 1776 (1987).

[46] Moore G. and Read N., *Nucl. Phys. B* **360** 362 (1991).

[47] Bardeen J., Cooper L.N. and Schrieffer J.R., *Phys. Rev.* **106** 162 (1957).

[48] Greiter M., Wen X.G. and Wilczek F., *Phys. Rev. Lett.* **66** 3205 (1991).

[49] Read N. and Green D., *Phys. Rev. B* **61** 10267 (2000).

[50] Scarola V.W., Park K. and Jain J.K., *Nature* **406** 863 (2000).

[51] Morf R.H., *Phys. Rev. Lett.* **80** 1505 (1998).

[52] Tőke C. and Jain J.K., *Phys. Rev. Lett.* **96** 246805 (2006).

[53] Stone M. and Chung S.B., *Phys. Rev. B* **73** 014505 (2006).

[54] Tewari S. *et al.*, quant-ph/0606101 (2006).

[55] Nayak C. and Wilczek F., *Nulcear Physics B* **479** 529 (1996).

[56] Stern A., von Oppen F. and Mariani E., *Phys. Rev. B* **70** 205338 (2004).

[57] Halperin B.I., *Helv. Phys. Acta* **56** 75 (1983).

[58] Gammel P.L. *et al.*, *Phys. Rev. B* **38** 10128 (1988).

[59] Xia J.S. *et al.*, *Phys. Rev. Lett.* **93** 176809 (2004).

[60] Eisenstein J.P. *et al.*, *Phys. Rev. Lett.* **61** 997 (1988).

[61] Eisenstein J.P. *et al.*, *Surf. Sci.* **229** 31 (1990).

[62] Pan W. *et al.*, *Phys. Rev. Lett.* **83** 3530 (1999).

[63] Eisenstein J., private communication (2006).

[64] Kouwenhoven L.P. *et al.*, *Phys. Rev. Lett.* **64** 685 (1990).

[65] Camino F.E., Zhou W. and Goldman V.J., *Phys. Rev. B* **72** 075342 (2005).

[66] Fendley P., Fisher M.P.A. and Nayak C., *Phys. Rev. Lett.* **97** 036801 (2006).

[67] Moon K. *et al.*, *Phys. Rev. Lett.* **71** 4381 (1993).

[68] Fendley P., Ludwig A.W.W. and Saleur H., *Phys. Rev. B* **52** 8934 (1995).

[69] Roddaro S. *et al.*, *Phys. Rev. Lett.* **93** 046801 (2004).

[70] Roddaro S. *et al.*, *Phys. Rev. Lett.* **95** 156804 (2005).

[71] Wen X.G., *Phys. Rev. B* **44** 5708 (1991).

[72] Wen X.G., *Phys. Rev. B* **43** 11025 (1991).

[73] Marcus C., private communication (2005).

[74] Stern A., private communication (2005).

[75] Efros A.L. and Shklovskii B.I., *J. Phys. C* **8** L49 (1975).

[76] Matthews J. and M. C., *J. Res. Natl. Inst. Stand. Technol.* **110** 497 (2005).

[77] Coleridge P.T., Stoner R. and Fletcher R., *Phys. Rev. B* **39** 1120 (1989).

[78] Coleridge P.T., *Phys. Rev. B* **44** 3793 (1991).

[79] Das Sarma S. and Pinczuk A., eds., Wiley, New York (1997).

[80] Goerbig M.O., Lederer P. and Smith C.M., *Phys. Rev. B* **68** 241302 (2003).

[81] Eisenstein J.P. *et al.*, *Phys. Rev. Lett.* **88** 076801 (2002).

[82] Jackson J.D., *Classical Electrodynamics*, Wiley (1975).

[83] Dresselhaus G., *Phys. Rev.* **100** 580 (1955).

[84] Bychkov Y.L. and Rashba E.I., *J. Phys C* **17** 6093 (1983).

[85] Knap W. *et al.*, *Phys. Rev. B* **53** 3912 (1996).

[86] Pfeffer P., *Phys. Rev. B* **59** 15902 (1999).

[87] Akkermans E., Wolf P. and Maynard R., *Phys. Rev. Lett.* (1986).

[88] Ishimaru K., volume 2, Academic Press, New York (1978).

[89] Datta S. and Das B., *Appl. Phys. Lett.* **56** 665 (1990).

[90] Altshuler B.L. and Aronov A.G., *Electron-Electron Interactions in Disordered Systems, edited by A. L. Efros and M. Pollak*, p. 11, North Holland, Amsterdam (1985).

[91] Lee P.A. and Ramakrishnan T.V., *Rev. Mod. Phys.* **57** 287 (1975).

[92] Bergmann G., *Solid State Comm.* **42** 815 (1982).

[93] Kouwenhoven L. and Marcus C.M., *Physics World* **11** 35 (1998).

[94] Beenakker C.W.J., *Rev. Mod. Phys.* **69** 731 (1997).

[95] Alhassid Y., *Rev. Mod. Phys.* **72** 895 (2000).

[96] Folk J.A. *et al.*, *Phys. Rev. Lett.* **86** 2102 (2001).

[97] Beenakker C.W.J. and van Houten H., *Solid State Physics* **44** 1.

[98] Dresselhaus P.D. *et al.*, *Phys. Rev. Lett.* **68** 106 (1992).

[99] Hikami S., Larkin A.I. and Nagaoka Y., *Prog. Theor. Phys.* **63** 707 (1980).

[100] Wolf S.A. *et al.*, *Science* **294** 1488 (2001).

[101] Awschalom D., Loss D. and Samarth N., *Semiconductor Spintronics and Quantum Computation*, Springer-Verlag (2002).

[102] Koga T. *et al.*, *Phys. Rev. Lett.* **88** 126601 (2002).

[103] Kiselev A.A. and Kim K.W., *Appl. Phys. Lett.* **78** 775 (2001).

[104] Jusserand B. *et al.*, *Phys. Rev. B* **51** 4707 (1995).

[105] Miller J.B. *et al.*, *Phys. Rev. Lett.* **90** 76807 (2003).

[106] Zutic I., Fabian J. and Sarma S.D., *Reviews of Modern Physics* **76** 323 (2004).

[107] Rudolph J. *et al.*, *Applied Physics Letters* **82** 4516 (2003).

[108] Duckheim M. and Loss D., *Nature Physics* **2** 195 (2006).

[109] Schliemann J., Loss D. and Westervelt R.M., *Phys. Rev. B* **73** 085323 (2006).

[110] Serebrennikov Y.A., *Phys. Rev. B* **73** 195317 (2006).

[111] Citro R., Romeo F. and Marinaro M., *Phys. Rev. B* **74** 115329 (2006).

[112] Trushin M.P. and Chudnovskiy A.L., *Physica E* **34** 397 (2006).

[113] Zumbühl D.M. *et al.*, *Phys. Rev. Lett.* **89** 276803 (2002).

[114] Zumbühl D.M. *et al.*, *to be published* (2004).

[115] Halperin B.I. *et al.*, *Phys. Rev. Lett.* **86** 2106 (2001).

[116] Aleiner I.L. and Fal'ko V.I., *Phys. Rev. Lett.* **87** 256801 (2001).

[117] Fal'ko V.I. and Jungwirth T., *Phys. Rev. B* **65** 81306 (2002).

[118] Meyer J.S., Altland A. and Al'tshuler B.L., *Phys. Rev. Lett.* **89** 206601 (2002).

[119] Meyer J.S., Fal'ko V.I. and Al'tshuler B.L., *in NATO Science Series II, edited by I.V. Lerner, B.L. Altshuler, V.I. Fal'ko and T. Giamarchi (Kluwer Academic Publishers, Dordrecht)* **Vol. 72** 117 (2002).

[120] Konemann J. *et al.*, *Phys. Rev. Lett.* **94** 226404 (2005).

[121] Zduniak A., Dyakonov M.I. and Knap W., *Phys. Rev. B* **56** 1996 (1997).

[122] Al'tshuler B.L. *et al.*, *Sov. Phys. JETP* **54** 411 (1981).

[123] Aronov A.G. and Lyanda-Geller Y.B., *Phys. Rev. Lett.* **70** 343 (1993).

[124] Koga T. *et al.*, *Phys. Rev. Lett.* **89** 046801 (2002).

[125] Bergmann G., *Phys. Rep.* **107** 1 (1984).

[126] Mathur H. and Stone A.D., *Phys. Rev. Lett.* **68** 2964 (1992).

[127] Lyanda-Geller Y.B. and Mirlin A.D., *Phys. Rev. Lett.* **72** 1894 (1994).

[128] Iordanskii S.V., Lyanda-Geller Y.B. and Pikus G.E., *JETP Lett.* **60** 206 (1994).

[129] Lyanda-Geller Y.B., *Phys. Rev. Lett.* **80** 4273 (1998).

[130] Morpurgo A.F. *et al.*, *Phys. Rev. Lett.* **80** 1050 (1998).

[131] Gor'kov L.P., Larkin A.I. and Khmel'nitskii D.E., *JETP Lett.* **30** 228 (1979).

[132] Lyanda-Geller Y. (2002), unpublished.

[133] Gasparyan V.M. and Zyuzin A.Y., *Sov. Phys. Solid State* **27** 999 (1985).

[134] Cassam-Chenai A. and Shapiro B., *J. Phys. I France* **4** 1527 (1994).

[135] Kawabata A., *J. Phys. Soc. Jpn.* **53** 3540 (1984).

[136] Hansen J.E., Taboryski R. and Lindelof P.E., *Phys. Rev. B* **47** 16040 (1993).

[137] Ramvall P., Kowalski B. and Omling P., *Phys. Rev. B* **55** 7160 (1997).

[138] Nitta J., Akazaki T. and Takayanagi H., *Phys. Rev. Lett.* **78** 1335 (1997).

[139] Schäpers T. *et al.*, *J. Appl. Phys.* **83** 4324 (1998).

[140] Heida J.P. *et al.*, *Phys. Rev. B* **57** 11911 (1998).

[141] Schultz M. *et al.*, *Semicond. Sci. Technol.* **11** 1168 (1996).

[142] Papadakis S.J. *et al.*, *Physica E* **9** 31 (2001).

[143] Winkler R. *et al.*, *Phys. Rev. B* **65** 155303 (2002).

[144] Lu J.P. *et al.*, *Phys. Rev. Lett.* **81** 1282 (1998).

[145] Ivchenko E.L. and Pikus G.E., *Superlattices and Other Heterostructures: Symmetry and Optical Phenomena*, volume 110 of *Springer Series in Solid-State Sciences*, Springer-Verlag (1995).

[146] Bulgakov E.N. *et al.*, *Phys. Rev. Lett.* **83** 376 (1999).

[147] Keppeler S. and Winkler R., *Phys. Rev. Lett.* **88** 46401 (2002).

[148] Khaetskii A.V. and Nazarov Y.V., *Phys. Rev. B* **61** 12639 (2000).

[149] Khaetskii A.V. and Nazarov Y.V., *Phys. Rev. B* **64** 2001 (2001).

[150] Cremers J.N.H.J. *et al.*, *Phys. Rev. B* **68** 125329 (2003).

[151] Millo O. *et al.*, *Phys. Rev. Lett.* **65** 1494 (1990).

[152] D'yakonov M.I. and Perel' V.I., *Sov. Phys. JETP* **33** 1053 (1971).

[153] Papadakis S.J. *et al.*, *Science* **283** 2056 (1999).

[154] Grundler D., *Phys. Rev. Lett.* **84** 6074 (2000).

[155] Kurdak C. *et al.*, *Phys. Rev. B* **46** 6846 (1992).

[156] Nitta J., Meijer F.E. and Takayanagi H., *App. Phys. Lett.* **75** 695 (1999).

[157] Shea H.R., Martel R. and Avouris P., *Phys. Rev. Lett.* **84** 4441 (2000).

[158] Engel H.A. and Loss D., *Phys. Rev. B* **62** 10238 (2000).

[159] Braggio A., Sassetti M. and Kramer B., *Phys. Rev. Lett.* **87** 146802 (2001).

[160] Mireles F. and Kirczenow G., *Phys. Rev. B* **64** 24426 (2001).

[161] Hackens B. *et al.*, *Physica E* **12** 833 (2002).

[162] Buttiker M., *Phys. Rev. B* **33** 3020 (1986).

[163] Baranger H.U. and Mello P.A., *Phys. Rev. B* **51** 4703 (1995).

[164] Brouwer P.W. and Beenakker C.W.J., *Phys. Rev. B* **55** 4695 (1997).

[165] Chan I.H. *et al.*, *Phys. Rev. Lett.* **74** 3876 (1995).

[166] Huibers A.G. *et al.*, *Phys. Rev. Lett.* **81** 200 (1998).

[167] Huibers A.G. *et al.*, *Phys. Rev. Lett.* **83** 5090 (1999).

[168] Brouwer P.W., Cremers J.N.H.J. and Halperin B.I., *Phys. Rev. B* **65** R81302 (2002).

[169] Fujisawa T. *et al.*, *Nature* **419** 278 (2002).

[170] Elzerman J.M. *et al.*, *Nature* **430** 431 (2004).

[171] Golovach V., Khaetskii A. and Loss D., *Phys. Rev. Lett.* **93** 16601 (2004).

[172] Zumbühl D.M. *et al.*, *Phys. Rev. B* **69** 121305R (2004).

[173] Al'tshuler B.L., *JETP Lett.* **41** 648 (1985).

[174] Lee P.A. and Stone A.D., *Phys. Rev. Lett.* **55** 1622 (1985).

[175] Meir Y., Gefen Y. and Entin-Wohlman O., *Phys. Rev. Lett.* **63** 798 (1989).

[176] Al'tshuler B.L. and Shklovskii B.I., *Sov. Phys. JETP* **64** 127 (1986).

[177] Stone A.D., *Phys. Rev. B* **39** 10736 (1989).

[178] Feng S., *Phys. Rev. B* **39** 8722 (1989).

[179] Imry Y., *Europhys. Lett.* **1** 249 (1986).

[180] Debray P. *et al.*, *Phys. Rev. Lett.* **63** 2264 (1989).

[181] Moon J.S., Birge N.O. and Golding B., *Phys. Rev. B* **56** 15124 (1997).

[182] Fukai Y.K. *et al.*, *Solid State Comm.* **94** 757 (1995).

[183] Birge N.O., Golding B. and Haemmerle W.H., *Phys. Rev. Lett.* **62** 195 (1989).

[184] Mailly D. *et al.*, *Europhys. Lett.* **8** 471 (1989).

[185] Gustin C. *et al.*, *Physica E* **17** 154 (2003).

[186] Gustin C. *et al.*, *Phys. Rev. B* **68** 241305R (2003).

[187] Hackens B. *et al.*, *Physica E* **17** 156 (2003).

[188] Huibers A.G. *et al.*, *Phys. Rev. Lett.* **81** 1917 (1998).

[189] Alves E.R.P. and Lewenkopf C.H., *Phys. Rev. Lett.* **88** 256805 (2002).

[190] Pan W. *et al.*, *Phys. Rev. Lett.* **83** 3530 (1999).

[191] Pan W. *et al.*, *Phys. Rev. Lett.* **83** 820 (1999).

[192] Lilly M.P. *et al.*, *Phys. Rev. Lett.* **83** 824 (1999).

[193] Pan W. *et al.*, *Physica E* **6** 14 (2000).

[194] Haldane F.D.M. and Rezayi E.H., *Phys. Rev. Lett.* **60** 956 (1988).

[195] Rezayi E.H. and Haldane F.D.M., *Phys. Rev. Lett.* **84** 4685 (2000).

[196] Tserkovnyak Y. and Simon S.H., *Phys. Rev. Lett.* **90** 016802 (2003).

[197] Chung S.B. and Stone M., *Phys. Rev. B* **73** 245311 (2006).

[198] Kitaev A., *Ann. Phys. (N.Y.)* **303** (2003).

[199] Bonesteel N.E. *et al.*, *Phys. Rev. Lett.* **95** 140503 (2005).

[200] Harju A., Saarikoski H. and Räsänen E., *Phys. Rev. Lett.* **96** 126805 (2006).

[201] Miller J.B. *et al.* (unpublished).

[202] D'Agosta R., Vignale G. and Raimondi R., *Phys. Rev. Lett.* **94** 086801 (2005).

[203] Roddaro S. *et al.*, *Phys. Rev. Lett.* **90** 046805 (2003).

[204] Lal S., *condmat/o611218* (2006).

[205] All resistances are differential with zero dc-current-bias unless otherwise noted.

[206] Büttiker M., *Phys. Rev. Lett.* **57** 1761 (1986).

[207] Beenakker C.W.J. and van Houten H., *Solid State Physics* **44** 1 (1991), see discussions in Secs. IV.B and IV.C. Our $R_{\rm D}$ corresponds to R_D^+ in this reference.

[208] In the absence of tunneling across the Hall bar, the derivations for $R_{\rm xy}$ and other resistances yield an equality, e.g., $R_{\rm xy}$=$h/e^2(1/N_{\rm bulk})$.

[209] Beenakker C.W.J., *Phys. Rev. Lett.* **64** 216 (1990).

[210] MacDonald A.H., *Phys. Rev. Lett.* **64** 220 (1990).

[211] Chang A.M. and Cunningham J.E., *Solid State Comm.* **72** 651 (1989).

[212] Chang A.M. and Cunningham J.E., *Surf Sci.* **229** 216 (1990).

[213] Wang J.K. and Goldman V.J., *Phys. Rev. Lett.* **67** 749 (1991).

[214] Würtz A. *et al.*, *Physica E* **22** 177 (2004).

[215] van Wees B.J. *et al.*, *Phys. Rev. B* **38** 3625 (1988).

[216] Alphenaar B.W. *et al.*, *Phys. Rev. Lett.* **64** 677 (1990).

[217] Alphenaar B.W. *et al.*, *Phys. Rev. B* **45** 3890 (1992).

[218] Chung Y.C., Heiblum M. and Umansky V., *Phys. Rev. Lett.* **91** 216804 (2003).

[219] Camino F.E., Zhou W. and Goldman V.J., *Phys. Rev. Lett.* **95** 246802 (2005).

[220] Willett R.L. *et al.*, *Phys. Rev. B* **37** 8476 (1988).

[221] Engel L.W. *et al.*, *Phys. Rev. B* **45** 3418 (1992).

[222] Gate voltages were restricted to the range -1.9 V (depletion) to -3 V and allowed to stabilize for several hours at each setpoint. Beyond -3 V the conductance was typically hysteretic as a function of gate voltage.

[223] Wong L.W., Jiang H.W. and Schaff W.J., *Phys. Rev. B* **54** R17323 (1996).

[224] Kane C.L. and Fisher M.P.A., *Phys. Rev. Lett.* **72** 724 (1994).

[225] Lu Y., private communication (2006).